Local structures and 5d→4f luminescence of Ce-doped fluoride crystals for optoelectronic applications

Author:

UY Mayrene Allam

Supervisor:

Prof. ABE Hitoshi

DOCTOR OF PHILOSOPHY

Department of Materials Structure Science

School of High Energy Accelerator Science

The Graduate University for Advanced Studies, SOKENDAI

September 2023

⟨Abridged version of Doctoral Thesis⟩

Acknowledgments

My sincerest gratitude goes to Professor Hitoshi Abe for providing me with the opportunity to acquire my degree at the Graduate University for Advanced Studies under his supervision. I am indebted to him for patiently mentoring me and teaching me everything I needed to know about X-ray absorption techniques. I am also grateful to him for providing me with numerous opportunities to be involved in the exchange of scientific information through conferences and workshops.

I am equally indebted to Professor Nobuhiko Sarukura for his mentorship and training in various advanced optical spectroscopic techniques. I appreciate his unwavering support for my participation in various conferences, as well as introducing me to his academic circles and sharing his expert knowledge on laser and scintillator materials. I am also very thankful to Professor Toshihiko Shimizu and Professor Yamanoi Kohei for their support and assistance during my stay at Osaka University Institute of Laser Engineering as a special research student.

I would also like to express my gratitude to my former supervisor, Professor Roland Sarmago, and his student, Christian Loer Llemit, for sharing their insights and resources on the DFT part of my research.

Furthermore, I would like to thank my dear friend Melvin for his support and guidance in both academic and non-academic matters. I am also thankful to my experiment buddy, Shinohara, for assisting me in all my optical experiments, and to Angelo for his participation during beamtimes and for engaging in research and non-research related discussions.

I would also like to extend my thanks to Professor Masao Kimura for his useful suggestions on how to improve my thesis.

Financial support for my studies was provided by SOKENDAI through the SOKENDAI Dispatch Program, Osaka University Institute of Laser Engineering through the Japan Society for the Promotion of Science (JSPS) program, and the Ministry of Education, Culture, Sports, Science and Technology (MEXT), Japan, for my scholarship. All my XAS experiments were performed under KEK PF-PAC nos.: 2020V008, 2021PF-T001, 2022G030, and 2022PF-T005. I am also grateful to the SOKENDAI office secretaries, Sawada-san, Hasegawa-san, Kimura-san, and Rtischev-san, as well as the Laser Advanced Material secretaries, Suzuki-san, Morita-san, and Yoshida-

san, for their unwavering assistance and guidance with various document works throughout my three-year course as a Ph.D. student.

My student life in Japan wouldn't have been enjoyable without the support of my roommates in PF, Kohei, Fumitoshi, and Le, as well as my friends in Tsukuba: Jessica, Jerali, Jun, Van, Reniel, April, Kenn, Marlon, and Bryan, and in Osaka: Verdad, Jonathan, Valynn, Jl, and Charisse.

I would like to express my gratitude to my mother, Maria, and my sisters, Aiza, Michellane, and Danice, for their prayers, love, and support.

Above all, I thank Him for all the blessings He has bestowed upon me. I am grateful for His wisdom and for keeping me sane during my challenging times.

To God be the glory.

Abstract

Cerium-doped fluoride crystals are by far the leading host material for tunable solid-state UV lasers, as well as scintillators for the detection of fast events such as neutrons, alpha-rays, and X-rays. This is due to their wide transparency in the ultraviolet (UV) region and fast emission decay times. The specificity and tunability of the luminescence of Ce-doped fluoride crystals in the UV region are ascribed to the interconfigurational 4f→5d (5d→4f) transitions of the Ce ion. These transitions are strongly influenced by the size and shape of the first anion coordination polyhedron of the Ce ion in its host environment. However, despite extensive research, a complete understanding of the relationship between the local structure of the Ce ion and the crystal field splitting has not been reached yet. This is primarily because the necessity for charge compensation often complicates the interpretation of the redshift observed in compounds where the lanthanide ion, such as the Ce^{3+} ion, occupies a divalent or monovalent cation site. In this regard, we employed XAS spectroscopy in order to investigate the changes in oxidation state of the Ce ions and the local structures surrounding it, and the extent of restructuring on the host's lattice specifically when the ions are doped in a cubic and trigonal host crystals at relatively low doping concentrations.

The samples used in this study were 0.01mol% Ce-doped CaF_2 crystal, which belongs to the cubic fluorite family of fluoride compounds, and 1.0mol% Ce-doped $LiCaAlF_6$ and $LiSrAlF_6$ crystals, which belong to the trigonal colquiriite group of crystals. The Ce-doped CaF_2 crystal exhibited multiple VUV absorption bands centered around 185, 195, 204, 244, and 304 nm, as well as double emission bands centered around 320 and 340 nm. On the other hand, both the absorption and emission spectra of Ce-doped $LiCaAlF_6$ and $LiSrAlF_6$ crystals showed a polarization dependence with respect to the incident and emitted beam. When the incident beam was polarized parallel to their c-axis, both crystals exhibited a blue shift in the 266-nm absorption band. Anisotropy was also observed in the double-peak emission bands of the crystals, centered at around 290 and 310 nm, when the emitted beam was polarized parallel to the c-axis of the crystals. This anisotropy is more pronounced in Ce-doped $LiSrAlF_6$ crystal compared to Ce-doped $LiCaAlF_6$ crystal. Ce-doped $LiSrAlF_6$ showed a significant blue

shift in the 290-nm emission band, accompanied by an increase in emission intensity. In contrast, Ce-doped $LiCaAlF_6$ showed a minor blue shift, and the increase in emission intensity was relatively weak.

Our XAS K-edge XANES and EXAFS analyses confirmed that the 4f→5d and 5d→4f transitions of Ce-doped CaF_2 crystal originated from a dominant Ce^{3+} center with an undistorted cubic (O_h) symmetry. However, despite the presence of its 244-nm band in the absorption spectra, we were unable to resolve the C_{3v} symmetry from the XAS spectra. In the case of Ce-doped $LiCaAlF_6$ and $LiSrAlF_6$ crystals, our combined XAS K-edge analyses (XANES and EXAFS) and XAS L_3-edge analysis (XANES) confirmed that the transitions were from a trigonal Ce^{3+} center with stretched Ce-F bond lengths and extended F-Ce-F^{ii} angles. Furthermore, we determined that the anisotropy in the optical and lasing properties can be attributed to the covalent interaction between the Ce^{3+} ion and its neighboring F^- and Al^{3+} ions. This covalent interaction is stronger in Ce^{3+}-doped $LiSrAlF_6$ compared to Ce^{3+}-doped $LiCaAlF_6$, resulting in more pronounced optical anisotropy and greater ESA. Specifically, the charge transfer between the Ce^{3+} ion and its ligand ions arises from the hybridization of the electronic states of the Ce^{3+} ion with those of the F^- and Al^{3+} ion. These effects are evident not only in the optical spectra but also in their respective XAS L_3-edge spectra.

Our XAS analyses provided valuable insights into the extent of restructuring within the vicinity of the Ce^{3+} ion in moderately-doped fluorite (CaF_2) and colquiriite-type ($LiCaAlF_6$ and $LiSrAlF_6$) fluoride crystals. It directly identified the dominant Ce center responsible for most of the observed absorption bands in Ce^{3+}-doped CaF_2 crystal. Additionally, it elucidated the source of anisotropy in the optical properties of Ce^{3+}-doped $LiCaAlF_6$ and $LiSrAlF_6$ crystals and the ambiguity in the mechanism of ESA, which hinders the achievement of efficient UV lasing in most fluoride and oxide crystals. The use of structural techniques, such as the XAS spectroscopy demonstrated in this study, can provide new and direct insights into the structural properties of wide band gap fluoride crystals. These insights not only contribute to a better understanding of the fundamental physical phenomena and underlying mechanisms but also hold promise for the development of new high-performance lasers, scintillators, and other optoelectronic devices.

Contents

Acknowledgments **i**

Abstract **iii**

Table of Contents **v**

List of Figures **vi**

List of Tables **vii**

1 Introduction **1**
1.1 Luminescence of Ce-doped compounds 1
1.2 Fluorides as solid-state UV laser media 10
1.3 Fluorides as scintillators 18
1.4 The calcium fluoride crystal 27
1.5 The colquiriite-type fluorides 34

2 Purpose and motivation **36**

3 Crystal growth techniques **39**
3.1 The Czochralski method 39
3.2 The Bridgman method 40

4 Characterization techniques **43**
4.1 X-ray absorption spectroscopy 43
4.2 Optical spectroscopies and other techniques 54
4.3 *Ab initio* methods 57
4.3.1 DFT calculation 57
4.3.2 FDMNES simulation 63

5 Experimental setup **65**
5.1 Sample preparation 65
5.2 Optical spectroscopies 66
5.2.1 Transmission/Absorption spectroscopy 66
5.2.2 PL spectroscopy 67

5.2.3 TRPL spectroscopy 68
5.2.4 Quantum yield spectroscopy 68
5.3 X-ray absorption spectroscopy 69
5.3.1 XAS at the Ce K-edge 69

6 Results **71**
6.1 Optical properties of Ce-doped calcium fluoride 71
6.2 Optical properties of Ce-doped colquiriites 77
6.3 Ce ion in calcium fluoride crystal 78
6.4 Ce ion in colquiriite-type fluoride crystals 81

7 Local structures and optical properties of Ce-doped fluoride crystals **82**
7.1 Ce ion in calcium fluoride crystal 82
7.2 Ce ion in colquiriite-type fluoride crystals 84
7.3 Designing a scintillator and UV laser crystal 85

8 Conclusion **92**
8.1 Conclusion 92

List of Figures

1.1 Absorption and emission spectra of various Ce^{3+}-doped fluoride and oxide crystals. [**?**] 2
1.2 Compiled spectroscopic redshift D(A) for the trivalent lanthanides in inorganic compounds as shown in Ref. [**?**]. The data points that are connected with a solid line are from LaF_3, $LaCl_3$, $LaBr_3$, La_2O_3, La_2O_2S, and La_2S_3. 4
1.3 Compiled spectroscopic redshift D(A) of the trivalent lanthanides in fluoride compounds as shown in Ref. [**?**]. The typical errors are ± 250 cm^{-1}. 4
1.4 Compiled spectroscopic redshift D(A) of the trivalent lanthanides in fluoride compounds as shown in Ref. [**?**] with the lanthanide ion substituting on (a) a monovalent or divalent cation site and (b) yttrium-containing fluoride compounds. The typical errors are ± 250 cm^{-1}. 5
1.5 Schematic energy diagram of Ce^{3+} ion in the free ion state, spherical field, octahedral field, cubic field and dodecahedral field. [**?**] 7
1.6 VRBE diagram with Ln^{2+}, Ln^{3+}, TM^{2+}, and TM^{3+} in $Y_3Al_2Ga_3O_{12}$ host [**? ? ? ?**]. 10
1.7 (a) Weak electron-phonon coupling of RE ions; and (b) relatively strong electron-phonon coupling of TM ions described by the configurational coordinate model. [**?**]. 11
1.8 Luminescence of Ce^{3+}-doped oxides and fluorides estimated from optical spectroscopic data. 12
1.9 The polarized absorption and (b) emission spectra for Ce^{3+}-doped $LiSrAlF_6$ and $LiCaAlF_6$ crystals reported in Ref. [**?**]. The π and σ symbols represent polarizations parallel and perpendicular to the optical axis of the host crystal, respectively. 16
1.10 In (a) Side and top view images of WGM resonator Ce^{3+}-doped $LiCaAlF_6$ crystal and (b) the UV WGM laser spectrum at several pump energies along with spectral profile of the pump light reported in Ref. [**?**]. 17

1.11 Small-signal gain spectra for (a) Ce^{3+}-doped $LiSrAlF_6$ and (b) Ce^{3+}-doped $LiCaAlF_6$ crystals. Further details can be found in Ref. [**?**]. The π and σ symbols represent probe polarizations parallel and perpendicular to the optical axis, respectively. 17
1.12 Laser output energies monitored at ∼292 nm as a function of absorbed 266 nm pump energy in (a) Ce^{3+}-doped $LiSrAlF_6$ or (b) Ce^{3+}-doped $LiCaAlF_6$ crystal. For further details, please refer to Ref. [**?**]. The π and σ symbols denotes longitudinal pump polarization parallel or perpendicular to the optical axis, respectively. The oscillator output on the other hand, was polarized along the optical axis. The least squares fits to the laser slope efficiencies are denoted by the solid lines. . 18
1.13 Relationship between the emission wavelength (nm) and the decay time ns in PL and scintillation. [**?**]. 20
1.14 Light yield of scintillators and cathode ray tube phosphors versus their energy band gap. The solid curve represents an approximate theoretical limit, while the dashed circles indicate some of the most commonly used scintillators. Hatched boxes give the band-gap energy ranges typical for some types of compounds [**?**]. 22
1.15 R&D History of common scintillators. Arrows indicate modifications of materials [**?**]. 23
1.16 Scintillation spectra of N^{3+}-, Er^{3+}- and Tm^{3+}-doped LuF_3 [**?**], Ce-doped GAGG [**?**], Pr-doped LuAG [**?**], Eu-doped SrI_2 [**?**], and Sm-doped FCZ glass-ceramics [**?**]. 24
1.17 The neutron signal detected at about 12 ns using APLF80 + 3Pr scintillator glass at the GEKKO XII facility of the Institute of Laser Engineering, Osaka University [**?**]. 25
1.18 Dependence of the decay time constant of the Ce-doped CaF_2 crystals on the Ce dopant concentration [**?**]. 26
1.19 X-ray induced radioluminescence spectra of Ce-doped CaF_2 scintillators in the wavelength range from 180 to 700 nm. The supplied bias voltage and tube current were 80 kV and 1 mA, respectively. The X-ray exposure time was 10 s for each integration. [**?**]. 26
1.20 Scintillation light yield plotted against Ce concentrations. The inset shows 241Am a-ray spectrum of Ce 0.1% doped CaF2. The shaping time was 2 ms and 5.5 MeV peak channel was determined by a single gaussian fitting. [**?**]. 27
1.21 Crystal structure of CaF_2 crystal 28

1.22 Ultraviolet absorption spectra of Ce^{3+} in CaF_2 crystal under varying Ce^{3+} concentrations from 0.005% to 5% at room and liquid-nitrogen temperature as reported in Ref. [**?**]. 30
1.23 (a) Absolute radioluminescence spectra of the CaF_2:Ce sample using 25-kV X-ray tube source and (b) Normalized radioluminescence spectra for the limit Ce concentrations. The emission band at 280 nm, which is gradually suppressed with increasing Ce concentration and completely dumped at 3% concentration, is from self-trapped exciton as reported in Ref. [**?**]. 31
1.24 Optimized local structures from DFT-PBE calculations of Ce^{3+} in CaF_2 with a local charge compensation by interstitial F^- ions and O_F substituents published in Ref. [**?**]. The point group symmetries and the values of selected distances are indicated. 32
1.25 Crystal structure of $Li(Ca, Sr)AlF_6$ crystal 34

3.1 Schematic diagram of the CZ process. 40
3.2 Schematic diagram of the Bridgman process and the transparent and colorless as-grown crystal. 41

4.1 Low-resolution X-ray absorption spectrum for Pb. The *K*, *L*, and *M* edge transitions corresponds to excitation of an electron from n=1, 2, and 3 shells, respectively. he *L* edges (inset) and the *M* edges are actually further split at higher resolution [**?**]. 44
4.2 Schematic illustration of an X-ray absorption spectrum, showing the structured absorption that is seen both within ≈50 eV of the edge (the XANES) and for several hundred to >1,000 eV above the edge (the EXAFS) [**?**]. 45
4.3 Transitions that give rise to the various emission lines. Excitation of a *K* shell results in K_α and K_β emission lines originating from n=2 and n=3, respectively. At higher resolution, these can be resolved into $K_\alpha 1$ and $K_\alpha 2$, with the splitting due to spin-orbit coupling. *L*-edge excitation exhibits a similar pattern but with greater complexity [**?**]. . . 47
4.4 Typical experimental setup for XAS measurements. 48
4.5 K-edge XANES of manganese oxides illustrating the almost linear correlation between the oxidation state and the edge position, where an increase of the oxidation state shifts the absorption edge to a higher energy. [**?**]. 49
4.6 Modulation of EXAFS photo-excitation cross-section by the interference between the outgoing and the back-scattered photoelectron waves. 52

4.7 Illustration of single scattering (dashed line) and multiple scattering (solid lines) pathways where the absorbing atom A is surrounded by two scattering atoms, S_1 and S_2 [**?**]. . . 53
4.8 EXAFS spectrum as calculated in Eq. 4.8 showing a characteristic "beat" in amplitude at k= $7\mathring{A}^{-1}$ due to the presence of both FeS and FeFe scattering. The structural information of a di-μ-sulfido bridged Fe dimer is encoded in the amplitude, the shape, the phase, and the frequency of the oscillations. Data have been multiplied by k^3 to enhance the oscillations at high k. Noise, which is pronounced at high k for dilute samples, often limits the data to k$\leq 12\mathring{A}^{-1}$ [**?**]. 54
4.9 Solving Kohn-Sham equation leads to a circular argument. . 60
4.10 Convergence of electron density and other observable quantities using Self Consistent Field calculation. 60

5.1 Photo of the 0.01mol% Ce-doped CaF_2 crystal. 65
5.2 Schematic diagram of the experimental setup used for photoluminescence (PL) measurement of the 0.01mol% Ce-doped CaF_2 crystal. 67
5.3 Schematic diagram for the time-resolved photoluminescence (TRPL) measurements of 0.01mol% Ce-doped CaF_2 crystal. 68
5.4 Schematic diagram of the XAS setup for the 0.01mol% Ce-doped CaF_2 crystal. 70

6.1 VUV absorption spectrum of 0.01mol% Ce-doped CaF_2 single crystal at room temperature. 72
6.2 UV PL spectrum of 0.01mol% Ce-doped CaF_2 single crystal under 290-nm Ti:sapphire laser excitation at room temperature. 73
6.3 UV PL emission decay of 0.01mol% Ce-doped CaF_2 single crystal under 290-nm Ti:sapphire laser excitation at room temperature. 74
6.4 Decay profile of the (a) 320 and (b) 340-nm emissions of 0.01mol% Ce-doped CaF_2 single crystal under 290-nm Ti:sapphire laser excitation at room temperature. The fitted single exponential functions are represented as dotted lines. 75
6.5 PL excitation spectra of 0.01mol% Ce-doped CaF_2 single crystal monitored around 320 and 340 nm at room temperature. 76
6.6 Quantum yield of 0.01mol% Ce-doped CaF_2 single crystal, monitored within the 308 to 386-nm emission range at room temperature under different excitation wavelengths. 77
6.7 Ce K-edge XANES spectrum of 0.01mol% Ce-doped CaF_2 single crystal (black line) at room temperature. The CeF_3 (red line) and CeO_2 (blue line) reference spectra for the Ce^{3+} and Ce^{4+} oxidation states, respectively, are also shown. . . . 78

6.8 Ce K-edge EXAFS spectra in k-space of 0.01mol% Ce^{3+}-doped CaF_2 single crystal at room temperature. The measured data for the Ce^{3+}-doped CaF_2 crystal is represented by solid black dots, while the first shell fitting curve of its Fourier transform, using the CeF_3 FEFF input file, is denoted by a red solid line. 80
6.9 Ce K-edge EXAFS spectra in R-space of 0.01mol% Ce^{3+}-doped CaF_2 single crystal at room temperature. The measured Ce^{3+}-doped CaF_2 data is also represented as solid black dots, while the 1st shell fitting curve of its Fourier transform using CeF_3 FEFF input file is denoted by a red solid line. . . 80

7.1 Local structure of Ce^{3+} ion in 0.01mol% Ce-doped CaF_2 and the corresponding crystal field splitting of its 4f and 5d levels. 83
7.2 General scheme of a solid-state laser. 86
7.3 Simplified energy level diagram of a three-level (left) and a four-level (right) laser. 87
7.4 Thermoluminescence glow curves of $Y_3Al_2Ga_3O_{12}$:Ce^{3+} with different electron traps [**?**]. 89

List of Tables

1.1 Overview of RE ions and their corresponding laser wavelengths [**?**]. 11

1.2 Spectroscopic characteristics of some Ce^{3+}-doped crystals [**?**]. Typical dopant concentration range from 0.01 to 2%at Ce. [a]Ce:LiCAF and Ce:LiSAF often grown with up to 2% Na^{+} co-doping for charge compensation.[n.] 13

1.3 Key performance characteristics of different Cerium lasers [**?**]. A=absolute efficiency, S=slope efficiency. [a]Peak power from chirped-pulse amplifier system. [b]Pumped at 266 nm with additional 532 nm pump to bleach color centres. [c]25% gain measured at 355 nm. 15

1.4 Lifetime of major luminescence ions [**?**]. The ∼5 ns value is that of Pr^{3+}-doped $20\,Al(PO_3)_3 - 80\,LiF$ (APLF) glass. . . . 21

1.5 Calculated $4\,f^1$ and $5\,d^1$ energy levels and 4f→5d relative transition intensities for the tetragonal C_{4v} F_i' (100) center in CaF_2:Ce with and without the effect of spin-orbit coupling (SOC)[a] from Ref. [**?**]. 33

Chapter 1

Introduction

1.1 Luminescence of Ce^{3+}-doped compounds

The luminescence of Ce^{3+} ion and other lanthanide ions in various compounds has been extensively studied over the past several decades. The particular attention to the Ce^{3+} ion stems from its efficient broadband luminescence due to parity-allowed electric dipole transitions between the $4f^0 5d^1$ excited state and the $4f^1$ ground state. More importantly, it can be substantially tuned from the visible to the UV region when the ions are incorporated in different crystalline host compounds such as oxides and fluorides as shown in Fig. 1.1 [**?**]. UV luminescence is also exhibited by non-crystalline compounds such as the fluoro-oxide lithium glass. Generally, the transfer limit is also a few nanoseconds thus, Ce^{3+}-doped compounds are very attractive for short-pulse UV laser as well as for scintillator applications. Extensive studies have been employed to understand the specificity and tunability of the luminescence in the UV to visible region. Though these studies have been mainly performed using optical spectroscopies, the optical and scintillation properties have been demonstrated to vary with (a) host material, (b) Ce concentration, (c) target doping site, and (d) co-doping with another cation.

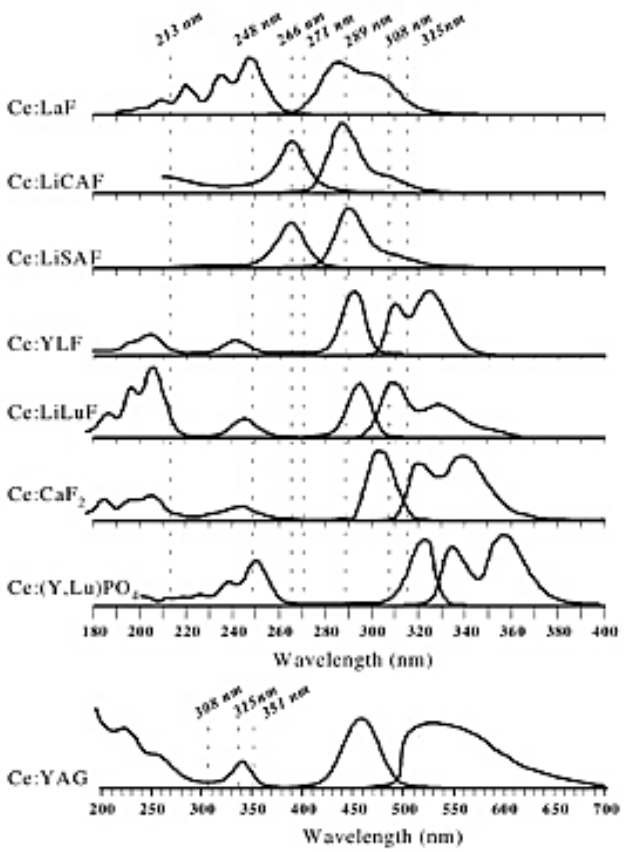

Figure 1.1: Absorption and emission spectra of various Ce^{3+}-doped fluoride and oxide crystals. [**?**]

Ce^{3+} ion has only one 4f-4f absorption due to the transition from $^2F_{5/2}$ to $^2F_{7/2}$ levels. These levels are separated by the spin-orbit coupling energy of approximately 2250 cm^{-1}. The electrons in the $5s^2$ and $5p^6$ orbitals sufficiently shield the 4f levels, resulting in their energies being primarily determined by the interactions within the lanthanide ion. In contrast, the excited 5d orbitals are strongly influenced by the surrounding ligand anions. Consequently, the centroid or average position of the 5d levels is lowered by an amount, D(A), relative to the position of the free Ce^{3+} ion, which is at 6.35 eV or 51230 cm^{-1} [**? ?**]. This is referred to as redshift and is written as

$$D\,(A) = [E_c\,(\text{free}) - E_c\,(A)] + [\varepsilon_s(A) - \varepsilon_s(\text{free})] \\ = \varepsilon_c(A) + \varepsilon_s(A) - 1890\text{cm}^{-1} \quad (1.1)$$

where E_c(free)=51230 cm^{-1} is the centroid position of Ce^{3+} as free ion, while E_c(A) represents the centroid position of Ce^{3+} in compound A. The term $\varepsilon_c(A)$ refers to the centroid shift, ε_s(free) represents the energy difference between the centroid position and the lowest 5d level ($^2D_{3/2}$) of the free Ce^{3+} ion, and $\varepsilon_s(A)$ represents the same for the Ce^{3+} ion in host A, which reflects the contribution from crystal field and spin-orbit coupling. This contribution to the redshift is known as the crystal field shift.

The values of spectroscopic redshift, D(A), compiled by Dorenbos from 300 different compounds, are shown in Fig. 1.2 [**?**]. For illustration purposes, the type of anions in the host crystal is represented by seven-digit identification numbers and displayed as variable A. The first two digits are significant to the type of anion. The redshift is shown to vary from the lowest value of 6600 cm^{-1} (234 nm) for $KMgF_3$ to the largest value of 33,300 cm^{-1} (625 nm) for $MgSc_2S_4$. These are the first 4f→5d absorption band of the Ce^{3+} ion in these inorganic compounds. The values of spectroscopic redshift, D(A), specific to fluorides are also shown in Fig. 1.3 [**?**], which is a 10,000 times enlarged view of Fig. 1.2. In this plot, the fifth digit of the identification number is significant to the type of trivalent rare-earth cation that often provides the site for Ce^{3+} ion. Lastly, the compiled spectroscopic redshift, D(A), specific to fluorides that have a monovalent or divalent cationic site for Ce^{3+} substitution, is shown in Fig. 1.4 [**?**]. In these plots, the compounds are grouped depending on the size of rare-earth cations in the structure. Those that do not contain trivalent rare-earth cations were given a zero value for the fifth digit (Fig. 1.4a), whereas yttrium-containing compounds were given a value of four (4) for the fourth digit (Fig. 1.4a). Both plots are in an expanded view as well.

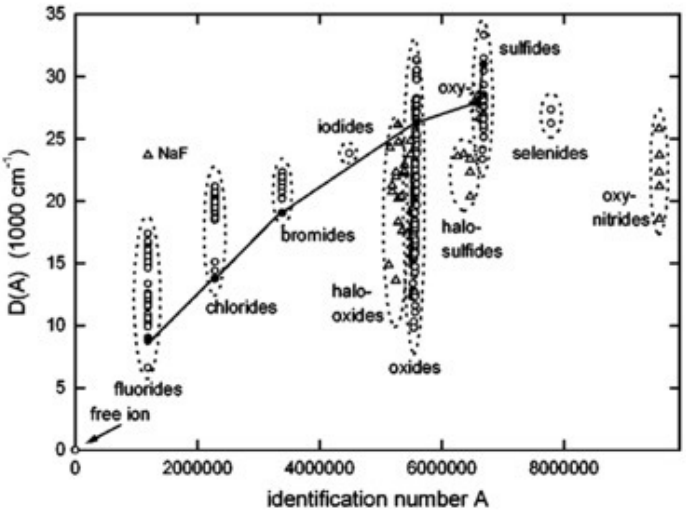

Figure 1.2: Compiled spectroscopic redshift D(A) for the trivalent lanthanides in inorganic compounds as shown in Ref. [**?**]. The data points that are connected with a solid line are from LaF_3, $LaCl_3$, $LaBr_3$, La_2O_3, La_2O_2S, and La_2S_3.

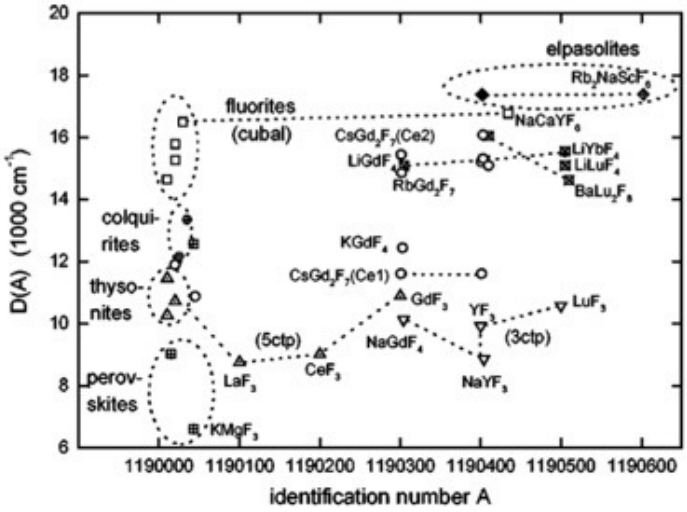

Figure 1.3: Compiled spectroscopic redshift D(A) of the trivalent lanthanides in fluoride compounds as shown in Ref. [**?**]. The typical errors are ± 250 cm^{-1}.

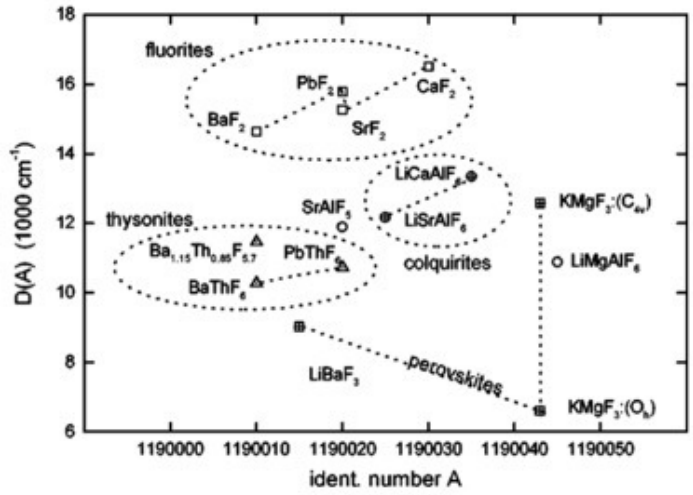

(a)

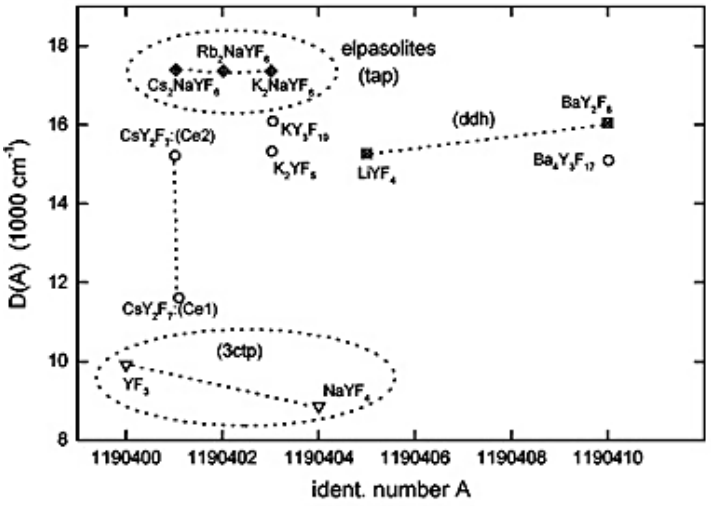

(b)

Figure 1.4: Compiled spectroscopic redshift D(A) of the trivalent lanthanides in fluoride compounds as shown in Ref. [**?**] with the lanthanide ion substituting on (a) a monovalent or divalent cation site and (b) yttrium-containing fluoride compounds. The typical errors are ± 250 cm^{-1}.

Redshift is observed to be dictated by two major phenomena, namely the nephelauxetic effect and crystal field splitting. The term nephelauxetic means "cloud expanding" and it depends on the strength of covalent bonding between the metal and its ligand. When more unpaired electrons of the metal spread over the ligand, the energy required to spin-pair the electrons is reduced. The bonding between the dopant and its ligands also induces a

repulsive force that further splits the two levels of the free Ce^{3+} ion, namely $^2D_{3/2}$ and $^2D_{5/2}$, based on the energy value of each d orbital in the geometric structure, thus its dependence on the anion orientation. The energy value difference between the lowest 5d level and the highest 5d level is called the crystal field splitting energy and is denoted by Δ_o. In addition to the redshift, the Stokes shift is also used to describe the difference between the spectral position of the maximum of the first absorption band and the maximum of the fluorescence emission. The Stokes shift is denoted by ΔS(A) and is expressed in either wavelength or wavenumber units.

A schematic diagram of the levels of the Ce^{3+} ion in different symmetries, extrapolated from various reported spectroscopic data, is shown in Fig. 1.5 along with the free ion levels from the Dieke diagram [**?** **?**]. There are five possible states ($= 2l + 1$) in the d orbital of the Ce^{3+} ion since its orbital angular momentum, l, is 2. If the spin-orbit coupling of the Ce^{3+} ion in the free ion state is ignored, the 5d orbital states degenerate. The Ce^{3+} ion's 5d orbital states in a spherical electrostatic field also degenerate but are subject to a centroid shift, ε_c. In the octahedral field, the 5d energy level can be split into $t_{2g}(d_{xy}, d_{xz}, d_{yz})$ and $e_g(d_{x^2-y^2}, d_{z^2})$. Here, Δ_o can often be expressed as the crystal field splitting parameter (10 Dq). Compared with the degenerate 5d level in the spherical field, the t_{2g} orbitals are stabilized by $-0.4 \times \Delta_0$ whereas the e_g orbitals are unstabilized by $+0.6 \times \Delta_0$. This gets inverted in the cubic field, i.e., compared with the degenerate 5d level in the spherical field, the e_g orbitals are stabilized by $0.6 \times \Delta_c$ whereas the t_{2g} orbitals are unstabilized by $0.4 \times \Delta_c$. Particularly for Ce^{3+} ion surrounded by O^{2-} ligands in a cubic polyhedron and assuming that it has the same bond length as that in an octahedral polyhedron, the splitting energy in the cubic field (Δ_c) can be reduced to $8/9 \times \Delta_0$ [**?**]. Theoretically, the e_g orbital in the cubic field is much lower than that of the octahedral field's t_{2g}. The t_{2g} state in the cubic field can also be split further by spin-orbit coupling. On the other hand, in a dodecahedral field, the e_g and t_{2g} can be split further. The splitting between the lowest $5\,d_1$ and the second lowest $5\,d_2$ is denoted by Δ_{12} and the crystal field splitting between the lowest $5\,d_1$ and the highest $5\,d_5$ is denoted as ε_{cfs} [**?**]. This is the case for Ce^{3+}-doped garnet compounds; the redshift is significantly manifested in its $4f \rightarrow 5\,d_1$ absorption band [**?**].

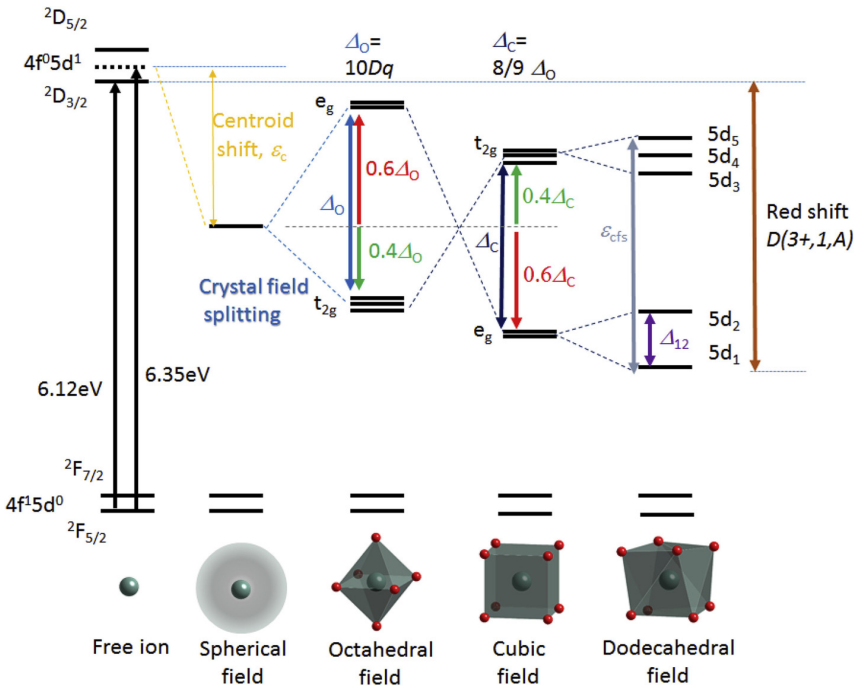

Figure 1.5: Schematic energy diagram of Ce^{3+} ion in the free ion state, spherical field, octahedral field, cubic field and dodecahedral field. [**?**]

Optical studies on the Ce^{3+} 5d levels have also shown that the crystal field splitting generally behaves quite independently from the centroid shift. The magnitude of the crystal field splitting depends on factors such as the coordination number, the size of the substituted cations, the symmetry of the Ce^{3+} ion, and the degree of polyhedron distortion around the Ce^{3+} ion. On the other hand, the centroid shift due to the nephelauxetic effect depends on two factors: covalency between the metal and the anion ligands, and the polarizability of the surrounding anion ligands.

Based on compiled spectroscopic data on lanthanide ions doped in various inorganic compounds (Figs. 1.2 - 1.4), four models were then extrapolated in order to predict 5d-level positions in yet uninvestigated materials [**? ? ? ? ? ?**]. These models are: (1) the redshift model, (2) the centroid shift model, (3) the charge transfer model (CT-model), and (4) the chemical shift model.

The *redshift model* was developed in 2000. It states that D(A) is the same for all 13 trivalent lanthanides, regardless of the number of electrons in the 4f-shell, when doped in the same site of the same host compound [**?**]. Thus, it is useful in estimating the first allowed $4\,f^n \rightarrow 4\,f^{n-1}5d$ transition

for all other lanthanides using a known redshift of just one lanthanide ion. That is why the focus on redshift has been entirely on Ce^{3+} since it has the simplest electron configuration. Redshift is given by

$$E_{fd}\left(n, Q, A\right) = E_{fd}\left(n, Q, free\right) - D\left(Q, A\right) \tag{1.2}$$

where n is the number of 4f electrons in the 4f shell, Q is the charge of the ion in host A, and E_{fd}(n, Q, free) is the 4f-$5d_1$ transition energy for the free lanthanide ions in vacuum as derived from extrapolation from data on those lanthanides as impurity in compounds [**?** **?**].

The *centroid shift model* was developed in 2001 to 2002 and has been used to predict the size of the centroid shift in Ce^{3+}-doped fluorides and Ce^{3+}-doped elpasolite fluorides, respectively [**?** **?**]. In terms of ligand polarizability, the centroid shift ε_c can be written as

$$\varepsilon_c = \frac{e^2}{4\pi\epsilon_0}\left(\langle r^2\rangle_{5d} - \langle r^2\rangle_{4f}\right)\sum_{i=1}^{k}\frac{\alpha_i}{R_i^6} \tag{1.3}$$

where r represents the radial position of the electron in the 4f or 5d orbital, and $\langle r^2\rangle$ is the expectation value of r^2, α_i is the polarizability of the ligand i positioned at a distance R_i from the metal ion, and ϵ_0 is the permittivity of vacuum. The summation is performed over all N nearest anion ligands. Centroid shift can also be written in terms of its proportionality to the square of the overlap integral, $S = \langle\phi_M\psi_L\rangle$, between the metal ($M$) and ligand ($L$) orbital [**?** **?**]

$$\varepsilon_c = \sum_{i=1}^{k}\left(a_i\langle\phi_{5d}|\psi_{L_i}\rangle^2 - b_i\langle\phi_{4f}|\psi_{L_i}\rangle^2\right) \tag{1.4}$$

where a and b are appropriate constants.

The *charge transfer model* (CT-model) developed from 2003 to 2005 deals with the location of the lanthanide ground state levels in relation to the top of the valence band. The basic idea is that the energy E_{4f}(n, 3+, A) of electron transfer from the valence band to a trivalent lanthanide provides the energy E_{4f}(n+1, 2+, A) of the 4f-ground state of the divalent lanthanide above the energy E_V(A) at the top of the valence band. By comparing the CT-energies to different Ln^{3+} ions at the same site in the

same host compound, the same characteristic energy differences always appear. The following equation applies

$$E_{4f}\left(n+1,2+,A\right)=E_V(A)+E^{CT}\left(6,3+,A\right)+\Delta E\left(n+1,7,2+\right) \quad (1.5)$$

where ΔE(n+1, 7, 2+) is the energy difference, averaged over many different compounds, between the CT to a trivalent lanthanide with n electrons in the 4f shell and the energy of CT to Eu^{3+}(n=6). Once the CT energy for one lanthanide is known, usually that of Eu^{3+}, then that of all others can be predicted. The CT-model provides the energies of the divalent lanthanide ground states with respect to E_V(A).

The latest addition to the series of models is the *chemical shift model* published in 2012. It deals with the vacuum referred 4f-electron binding energy E_{4f}(n, Q, A) (4f-VRBE) of lanthanide ions in compounds. The model relates the chemical shift, defined as E_{4f}(n+1, 2+, vacuum), E_{4f}(n+1, 2+, A) for a divalent lanthanide, with the chemical shift E_{4f}(n+1, 3+, vacuum), E_{4f}(n+1, 3+, A) for the same trivalent lanthanide in a chemical environment [**?**]. Generally, the VRBE diagram of Ln ions is drawn with the number of 4f electrons of Ln^{3+} ion on the x-axis and the VRBE of the electron in a compound on the y-axis, as shown in Fig. 1.6. The VRBE of Ln ion can be predicted using several parameters such as the host exciton creation energy (E^{ex}), charge transfer energy of Ln^{3+}, and the parameter for energy difference between Eu^{2+} and Eu^{3+} energy levels, U(6,A). These parameters can be obtained through simple spectroscopy. However, it is not easy to obtain the U(6,A) value directly. Hence, U(6,A) is often estimated using the centroid shift of the 5d energy level of Ce^{3+} (ε_c), and the VRBE of Eu^{2+} (E_{4f}(7, 2+, A)) can then be determined by the U(6,A) as follows

$$U\left(6,A\right)=5.44+2.834\exp\left(-\frac{\varepsilon_c}{2.2}\right) \quad (1.6)$$

$$E_{4f}\left(7,2+,A\right)=-24.92+\frac{18.05+U\left(6,A\right)}{0.777-0.0353U\left(6,A\right)} \quad (1.7)$$

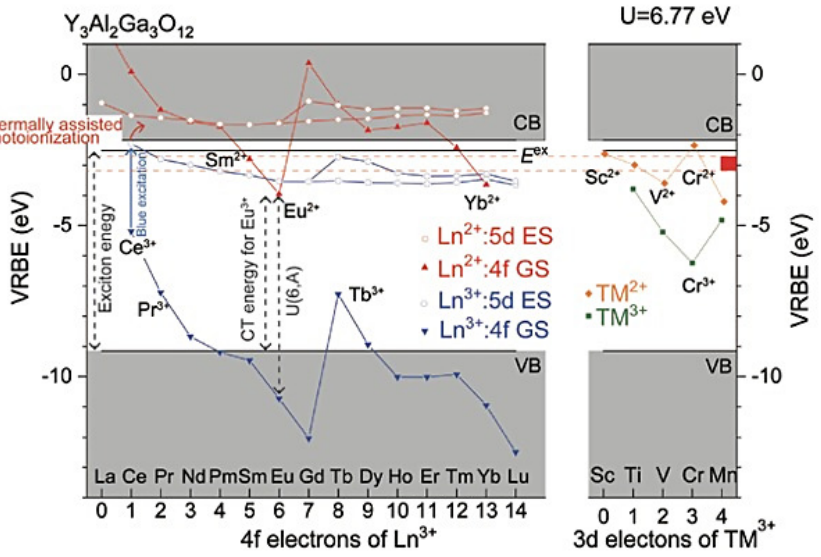

Figure 1.6: VRBE diagram with Ln^{2+}, Ln^{3+}, TM^{2+}, and TM^{3+} in $Y_3Al_2Ga_3O_{12}$ host [**? ? ? ?**].

The zig-zag curves of 4f electron energy with respect to the vacuum level for Ln^{2+} and Ln^{3+} ions, as a function of the 4f electron number, are not significantly affected by the composition of compounds due to the insensitivity of the 4f electrons to their environments. Thus, after determining the VRBE of Eu^{2+} using the U(6,A) value, all the VRBEs of Ln^{2+} and Ln^{3+} can be estimated based on the universal nature of the zig-zag curves. Strictly speaking, the zig-zag curves of Ln^{2+} and Ln^{3+} are tilted towards lower energy as the number of 4f electrons increases, due to the nephelauxetic effect [**? ?**].

1.2 Fluorides as solid-state UV laser media

The basic properties of solid state laser crystals are defined by intrinsic centers of the host material and extrinsic centers formed by a dopant ion which usually is a rare earth (RE) or transition metal (TM) ion. Laser crystals with TM dopants are characterized by broad 3d-3d absorption and emission band because its 3d-electrons are non-shielded and can couple easily with the phonons of the surrounding ligands. In contrast, those with RE dopants are characterized by narrow 4f-4f transitions because its 4f-electrons are shielded by the electrons in the 5s and 5p-orbitals and can

only be weakly influenced by the crystal field provided by the ligands. The laser wavelengths of important RE ions are listed in table 1.1 [**?**]. The energy level scheme of RE ions with weak electron–phonon coupling and the vibronic energy levels of the TM ions with strong electron–phonon coupling is illustrated in Fig. 1.7 [**?**].

Table 1.1: Overview of RE ions and their corresponding laser wavelengths [**?**].

Laser ion	Laser wavelengths	Remarks
Nd^{3+}	$0.9\mu m, 1.06\mu m, 1.3\mu m$	NIR RE lasers
Yb^{3+}	$1.0 - 1.1\mu m$	
Tm^{3+}	$2\mu m$	
Ho^{3+}	$2\mu m$	
Er^{3+}	$1.6\mu m, 3\mu m$	
Pr^{3+}	$0.52\mu m, 0.60\mu m$	Visible RE lasers
	$0.64\mu m, 0.72\mu m$	
Er^{3+}	$0.55\mu m$	
Ce^{3+}	$0.3\mu m$	UV RE lasers

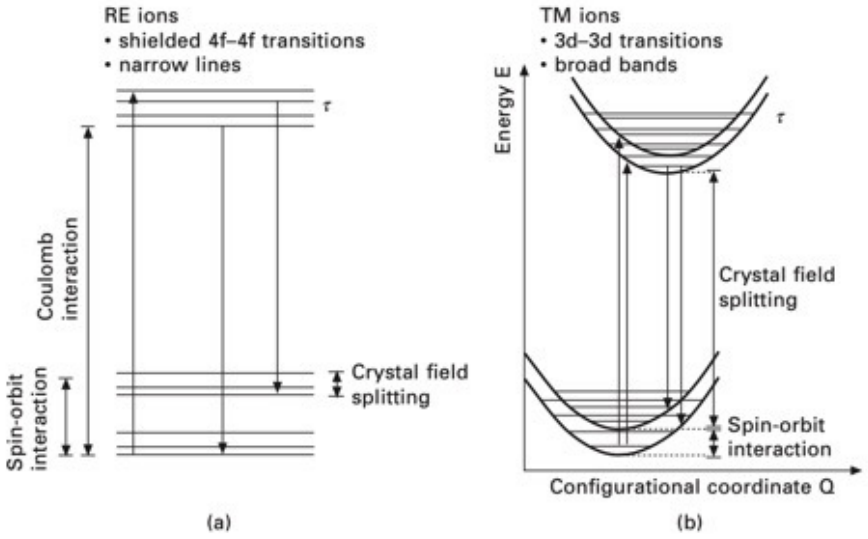

Figure 1.7: (a) Weak electron-phonon coupling of RE ions; and (b) relatively strong electron-phonon coupling of TM ions described by the configurational coordinate model. [**?**].

Host materials, on the other hand, are usually based on oxide compounds. The most recognized among the commercially available laser host materials

is yttrium aluminum garnet ($Y_3Al_5O_{12}$) or YAG. YAG crystal doped with Nd^{3+} ion is known to exhibit various groups of NIR laser transitions around 900 nm, 1060 nm, and 1300 nm. The strongest and mostly used emission is between 1050 nm and 1100 nm and typically it is pumped at the 806 nm wavelength of a diode laser. But when doped with Ce^{3+} ion, its emission shifts towards the visible region. However, existence of strong excited state absorption (ESA) hinders the crystal from laser oscillation [**?**]. This behavior has also been found true for other Ce^{3+}-doped oxides crystals thus there is no known Ce laser in oxides yet. Conversely, lasing can be realized in Ce^{3+}-doped fluorides and moreover, the emission further shifts towards the UV region. This shift is shown in Fig. 1.8. Fluorides are favoured over oxides as host materials because of their large band gaps and low phonon energies. Further, they are stable to radiation damage and have small non-linear refractive indices [**?** **?**]. Spectroscopic and key lasing performance characteristics of some Ce^{3+}-doped crystals are tabulated in Tables 1.3 and 1.2.

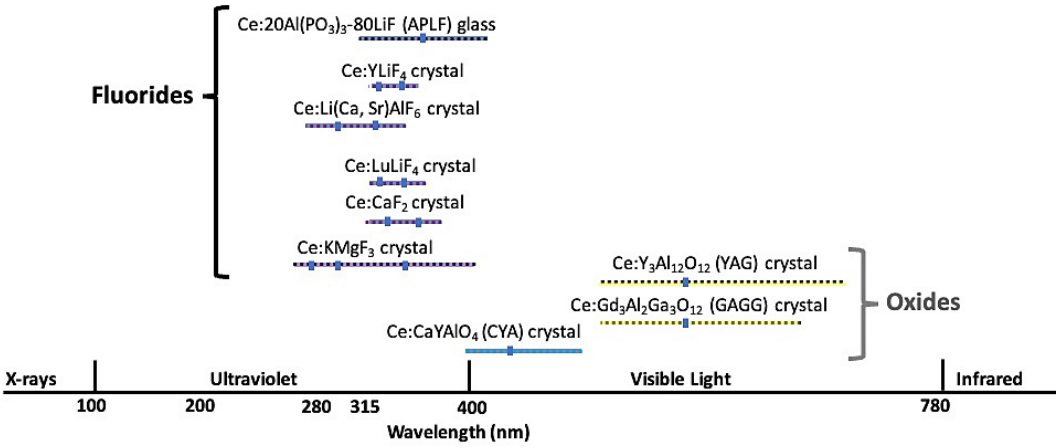

Figure 1.8: Luminescence of Ce^{3+}-doped oxides and fluorides estimated from optical spectroscopic data.

Table 1.2: Spectroscopic characteristics of some Ce^{3+}-doped crystals [**?**]. Typical dopant concentration range from 0.01 to 2%at Ce. [a]Ce:LiCAF and Ce:LiSAF often grown with up to 2% Na^+ co-doping for charge compensation.[n.]

Material	**5d level lifetime** (ns)	**Emission cross section** ($\times 10^{-18}$ cm^2)	**ESA cross section** ($\times 10^{-18}$ cm^2)	**Remarks**
Ce:YLF	40 [**?**]	7.6 unpolarized at 325 nm emission peak [**?**]	unknown	Stable and transient (50 ns, 200 μs and 50 ms) color centers, poor quantum yield
Ce:LiLuF	40 [**?**]	6.7 π, 4.5 σ at 308 nm [**?**]	<0.1 π, 2 σ at 308 nm [**?**]	ESA greatly reduces laser efficiency for σ polarization, but not π polarization
Ce:LiCAF[a]	25 [**?**]	9.6 π, 6.2 σ at 290 nm emission peak [**?**]	3.6 π, 2.2 σ at 290 nm emission peak [**?**]	Gain cross section $6x10^{-18}cm^2$ at 290 nm

Continued on next page

Table 1.2 – continued from previous page

Material	**5d level lifetime (ns)**	**Emission cross section** ($\times 10^{-18} cm^2$)	**ESA cross section** ($\times 10^{-18} cm^2$)	**Remarks**
Ce:LiSAF[a]	28 [**?**]	9.5 π, 6.1 σ at 290 nm emission peak [**?**]	2.7 π, 4.6 σ at 290 nm emission peak [**?**]	Formation of color centers limits performance; however, use of an additional anti-solarant pump can bleach color centers and restore efficiency [**?**]
Ce:LaF_3	20 [**?**]	unknown	unknown	Color centers limit performance at above 0.03 Hz [**?**]
Ce:CaF_2	40 [**?**]	unknown	unknown	Formation of color centers prevents lasing
Ce:YAG	65 [**?**]	unknown	up to 7 at 700 nm [**?**]	ESA prevents lasing

Table 1.3: Key performance characteristics of different Cerium lasers [**?**]. A=absolute efficiency, S=slope efficiency. [a]Peak power from chirped-pulse amplifier system. [b]Pumped at 266 nm with additional 532 nm pump to bleach color centres. [c]25% gain measured at 355 nm.

Material	**pump λ's** (nm)	**Tunability** (nm)	**Output power or energy**	**Maximum efficiency**
Ce:YLF	248	325 [**?**]	1.5 mJ [**?**]	5% (A) [**?**]
Ce:LiLuF	248, 289	305-333	380 mW	62% (S) [**?**]
	290	[**?**]	[**?**]	55% (S) [**?**]
			27 mJ [**?**]	
Ce:LiCAF[a]	263, 266,	280-316	900 mW	46% (S) [**?**]
	271	[**?**]	60 mJ [**?**]	42% (S) [**?**]
			98 mJ [**?**]	
			30 GW[a] [**?**]	
Ce:LiSAF[a]	263, 266	283-313	250 mW	47% (S)[b] [**?**]
	271	[**?**]	[**?**]	
			5 mJ [**?** **?**]	
Ce:LaF_3	248	286 [**?**]	5 μJ [**?**]	0.01% (A) [**?**]
Ce:KYF_2	308	362 [**?**]	-	-
Ce:LuPO	315	355[c] [**?**]	-	-

By far, the most prominent and excellent solid-state gain media for amplifying UV pulses are the Ce^{3+}-doped colquiriite-type, lithium calcium hexafluoroaluminate (Ce:$LiCaAlF_6$ or Ce:LiCAF) and lithium strontium hexafluoroaluminate (Ce:$LiSrAlF_6$ or Ce:LiSAF) crystals. As shown in Fig. 1.9, Ce:LiCAF and Ce:LiSAF have a strong absorption band around 266 nm (UV) [**?**], which allows direct optical pumping by the fourth harmonics of an Nd:YAG laser. The optical emissions of both crystals are characterized by a broad bandwidth (280 - 320 nm), a large Stokes shift, and a nanosecond lifetime owing to the electric dipole-allowed inter-configurational 5d→4f (5d→4f) transition of Ce^{3+} ion. In principle, this broad bandwidth allows for tunable continuous wave (CW) and mode-locked laser operation modes, ultrashort pulse generation, and quantum efficiency of around 90% [**?** **?**

]. A low-threshold lasing pump power intensity of 7.5×10^9 $\frac{W}{m^9}$ has been demonstrated using a whispering gallery mode (WGM) resonator made from Ce:LiCAF crystal [**?** **?** **?**]. In the WGM setup shown in Fig. 1.10, population inversion is achieved by repeated total internal reflections at the surface modes of the circular dielectric medium.

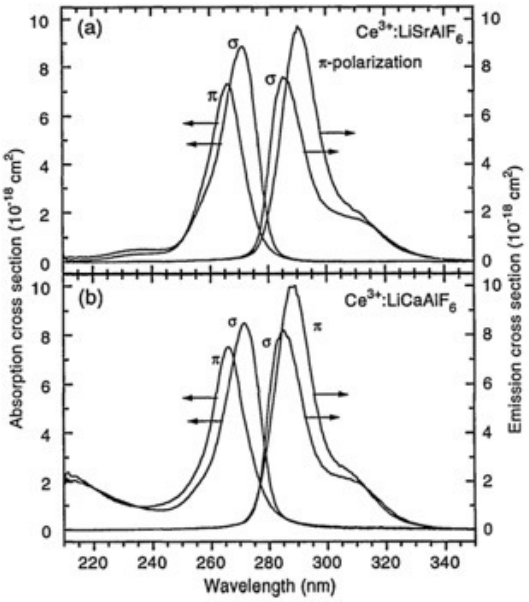

Figure 1.9: The polarized absorption and (b) emission spectra for Ce^{3+}-doped $LiSrAlF_6$ and $LiCaAlF_6$ crystals reported in Ref. [**?**]. The π and σ symbols represent polarizations parallel and perpendicular to the optical axis of the host crystal, respectively.

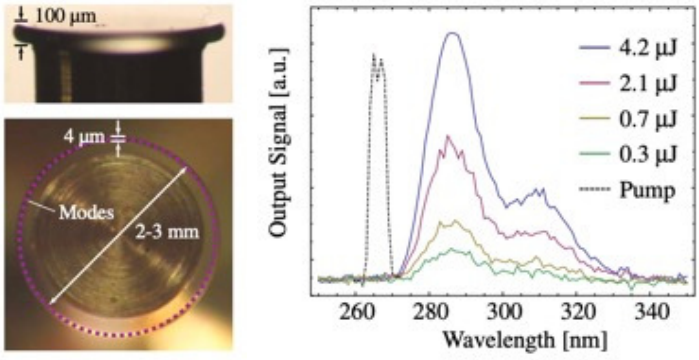

(a) (b)

Figure 1.10: In (a) Side and top view images of WGM resonator Ce^{3+}-doped $LiCaAlF_6$ crystal and (b) the UV WGM laser spectrum at several pump energies along with spectral profile of the pump light reported in Ref. [**?**].

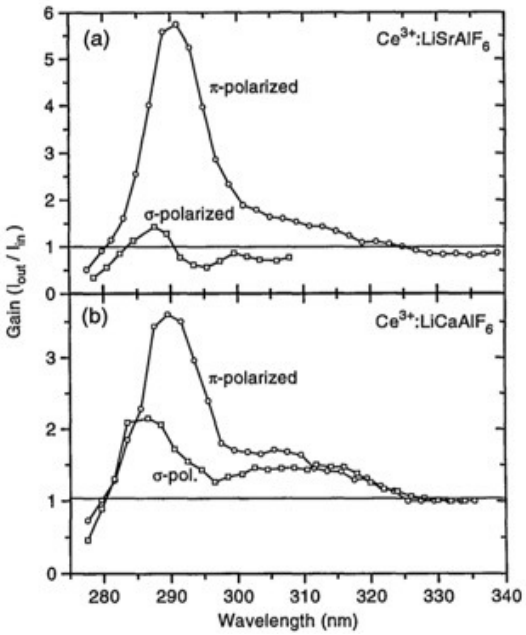

Figure 1.11: Small-signal gain spectra for (a) Ce^{3+}-doped $LiSrAlF_6$ and (b) Ce^{3+}-doped $LiCaAlF_6$ crystals. Further details can be found in Ref. [**?**]. The π and σ symbols represent probe polarizations parallel and perpendicular to the optical axis, respectively.

ESA has also been observed in Ce:LiCAF and Ce:LiSAF crystals but at a lesser degree than any other Ce^{3+}-doped crystals. Thus, high laser slope efficiencies of 21% and 29% (Fig. 1.12) have been demonstrated for Ce:LiCAF and Ce:LiSAF, respectively. Still, the gain values have been

found to drop significantly when the pump and the probe beam are polarized perpendicular to the optical or c-axis of the crystals as shown in Fig. 1.11 [**?**]. This effect is considerably stronger in LiSAF than in LiCAF. While the luminescence of Ce:LiCAF and Ce:LiSAF were ascribed to the immediate coordination octahedron of the Ce^{3+} ion, the anisotropy in the laser slope efficiency were associated to the anisotropic nature of ESA itself and to the layered structure of the crystals.

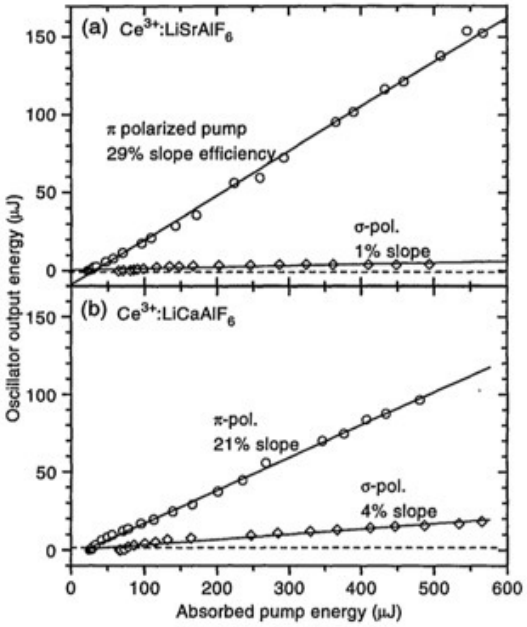

Figure 1.12: Laser output energies monitored at ∼292 nm as a function of absorbed 266 nm pump energy in (a) Ce^{3+}-doped $LiSrAlF_6$ or (b) Ce^{3+}-doped $LiCaAlF_6$ crystal. For further details, please refer to Ref. [**?**]. The π and σ symbols denotes longitudinal pump polarization parallel or perpendicular to the optical axis, respectively. The oscillator output on the other hand, was polarized along the optical axis. The least squares fits to the laser slope efficiencies are denoted by the solid lines.

1.3 Fluorides as scintillators

In ionizing radiation detectors, luminescent materials known as scintillators are used to covert high-energy ionizing radiation, such as X-rays and γ-rays to a near-visible or visible light. Scintillators have widespread applications in medical imaging (PET, X-ray CT, SPECT) [**?**], security[**?**], oil-logging [**?**], non-destructive studies of cultural objects [**?**], astro-physics[**?**], and

particle-physics [**?**]. Another luminescent-type detector called storage phosphor is also used. Storage phosphor is analogous to scintillator, with the difference being that a significant part of the energy released upon interaction with radiation is stored in long-living traps. The trap, which is the loss mechanism of a scintillator, serves as the memory bit of a storage phosphor. The lifetime must be long enough for the intended application. The absorbed energy is then released through optical (optically stimulated luminescence, OSL) or thermal (thermally stimulated luminescence, TSL) stimulation. The main application of OSL [**?**] or TSL [**?**] dosimeters is personal dosimetry to measure ionizing radiation.

Since events in high-energy ionizing radiation are both fast and rare, luminescent materials must process each radiation signal event-by-event with a fast response time. The scintillation decay rate is fundamentally governed by the speed of transfer of free electrons and holes from an ionization track to the emission center and the lifetime of the luminescence state of the activator. The scintillation decay rate of an excited state is given by

$$\Gamma = \frac{1}{\tau} \propto \frac{n}{\lambda_{em}^3} \left(\frac{n^2+2}{3} \right)^2 \sum_f |\langle f|\mu|i\rangle|^2 \tag{1.8}$$

where Γ is the scintillation decay rate of an excited state, τ is the fluorescence decay time, λ_{em}^3 is the emission wavelength, n is the refractive index, and μ is the dipole operator connecting the initial state $|i\rangle$ with the final state $\langle f|$. The matrix element connecting an initial state with a final state via the dipole operator will only be of appreciable size for transitions between states of different parity. Although other processes of energy migration from the host lattice to emission centers can be involved, the scintillation decay time is approximately proportional to λ^3. Figure 1.13 demonstrates this relationship between the decay time, τ, and the emission wavelength, λ, in PL and scintillation.

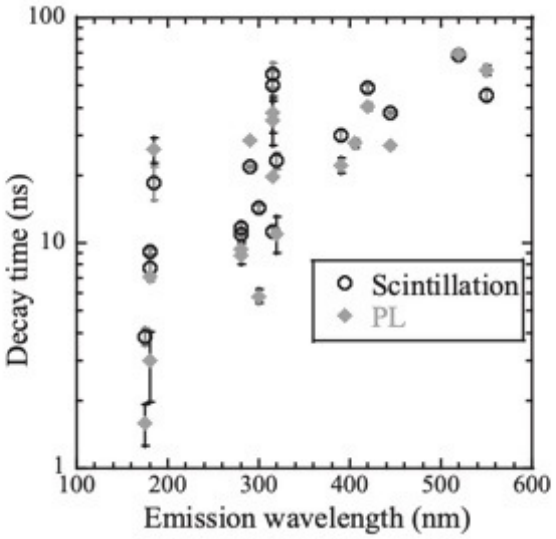

Figure 1.13: Relationship between the emission wavelength (nm) and the decay time ns in PL and scintillation. [**?**].

The transitions between the 5d and 4f levels of trivalent lanthanides such as Ce^{3+}, Pr^{3+}, and Nd^{3+}, and in the divalent lanthanides like Eu^{2+}, are parity allowed. As dictated by Eq. 1.8, these transitions are therefore fast. Transitions between levels of the p- and s- configurations in TI^{+}, Pb^{2+}, and Bi^{3+} are equally parity allowed and are also fast. In contrast, transitions starting from a less than half-filled configuration and terminating in a more than half-filled ground-state configuration are slow because they are usually spin forbidden. This is the case for TI^{+}:Nal, $Bi_4Ge_3O_{12}$, and TI^{+}:CsI where emissions have $\tau > 200$ ns. The same applies for self-trapped exciton emission ($\tau > 1000$ ns), and when Tm^{3+} ($4f^{12}$) and Er^{3+} ($4f^{12}$) are the activator ions. For Eu^{2+}, decay times are usually around 1μs.

Excluding lanthanides, which have non-radiative relaxation to high-lying 4f-levels, one is restricted to the Ce^{3+}, Pr^{3+}, and Nd^{3+} ions for fast scintillators. The lifetime of the lowest 5d-state of Ce^{3+} in inorganic compounds ranges from 17 to 60 ns, that of Pr^{3+} is about two times shorter, and that of Nd^{3+} is again two times shorter. The shortening of the emission wavelength from Ce^{3+} to Pr^{3+} to Nd^{3+}, to a great extent, is responsible for the two and four times shortening of the decay time of Pr^{3+} and Nd^{3+} luminescence as dictated by Eq. 1.8. Table 1.4 summarizes the major luminescence ions and their approximate lifetimes.

Table 1.4: Lifetime of major luminescence ions [**?**]. The ∼5 ns value is that of Pr^{3+}-doped $20\,Al(PO_3)_3-80\,LiF$ (APLF) glass.

Luminescence center	Transition	Lifetime
$Ce^{3+}, Pr^{3+}, Nd^{3+}, Eu^{2+}, etc.$	$5d-4f$	$\sim 5\text{ns}- \sim 1\mu\text{s}$
$Pr^{3+}, Tb^{2+}, Eu^{3+}, etc.$	$4f-4f$	$\sim 10\mu s- \sim 10\text{ms}$
$Cr^{3+}, Mn^{4+}, Mn^{2+}, etc.$	$3d-3d$	$\sim 10\mu s- \sim 10\text{ms}$
$Bi^{3+}, Pb^{2+}, Sn^{2+}, etc.$	$p-s$	$\sim 10\mu\text{s}$

In another aspect, the number of carriers or photons produced is proportional to the quantity or energy of the incident ionizing radiation. If we assume that all charge carriers will be transferred to activator ions and that the intrinsic luminescence quantum efficiency of the activator ion is unity, then the light output of the scintillation crystal will be fully determined by the number of electron-hole pairs created in the ionization track. Therefore, the scintillation light output can be expressed as

$$n_{e-h} = \frac{E_\gamma}{\beta E_g} \tag{1.9}$$

where n_{e-h} is the number of electron-hole pairs created during illumination, E_g is the band gap of the material, E_γ is the emission output, and β is a weight factor. It is reported to be close to 2.5 as determined experimentally and theoretically [**?**]. Fig. 1.14 shows the curve describing the fundamental limit on light output assuming $\beta = 2.5$. The hatched bars indicate the range of band gap values typical for the type of compounds [**?**]. High-band gap fluorides are shown to have the lowest light yield among the set of compounds, while the low-band gap sulfides have the highest.

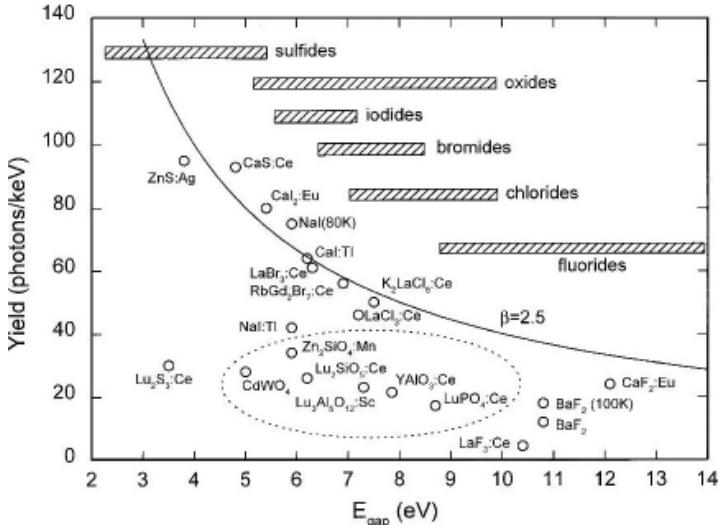

Figure 1.14: Light yield of scintillators and cathode ray tube phosphors versus their energy band gap. The solid curve represents an approximate theoretical limit, while the dashed circles indicate some of the most commonly used scintillators. Hatched boxes give the band-gap energy ranges typical for some types of compounds [**?**].

Figure 1.15 provides an overview of the research and development history of common scintillators. Initially, materials such as alkali halides (NaI and CsI) and natural phosphors (CaF_2 and $CdWO_4$) were widely used. Today, well-known scintillators include Tl-doped NaI, Tl-doped CsI, Eu-doped CaF_2, and the artificial $Bi_4Ge_3O_{12}$ (BGO) [**?**], which was developed after 1980. In recent years, there has been extensive investigation of Ce-activated crystals such as perovskites like $LuAlO_3$ (LuAP) [**? ? ?**] and $YAIO_3$ (YAP) [**?**], as well as orthosilicates like Lu_2SiO_5 (LSO) and Y_2SiO_5 (YSO) [**?**]. Consequently, Ce doping has become a standard approach for developing new scintillators. Other ions, such as praseodymium (Pr) or ytterbium (Yb), have also received attention when activated in the same host materials [**? ? ?**]. Figure 1.16 shows typical scintillation spectra for these scintillators. Notably, the emission wavelength resulting from 5d-4f transitions strongly depends on the crystal field, which is specific to each host lattice. It is important to emphasize that the presented data are only examples. In the case of Ce- and Pr-doped scintillators, the presence of traps and parasitic absorption can reduce the light yield. Interestingly, co-doping a $Lu_3Al_5O_{12}$ crystal with Ce^{3+} and Ce^{3+} has been found to enhance the light yield, possibly due to the generation of Ce^{4+} by doping with Mg^{2+} [**?**]. Further

experiments are required to fully understand this phenomenon, as similar enhancement effects have not been observed in other garnet scintillators [**?**].

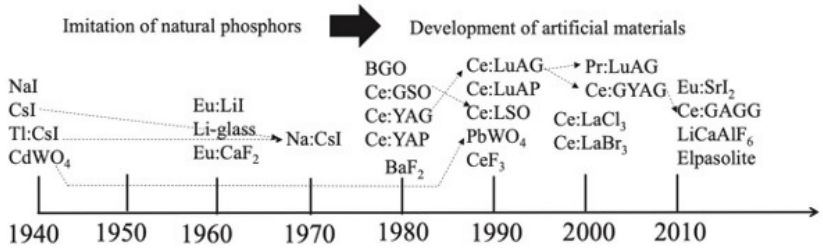

Figure 1.15: R&D History of common scintillators. Arrows indicate modifications of materials [**?**].

To address the need for efficient scintillators, the development of new materials is being explored. One promising option is the use of Nd-doped crystals, which have demonstrated both high light output and relatively good timing properties for VUV luminescence [**?**]. This makes them attractive candidates for fast VUV scintillators. Additionally, BaF_2 is a commonly used scintillator with very fast response time for detecting X-rays, gamma rays, and other high-energy particles. It finds application in the detection of 511 keV gamma photons in positron emission tomography. Due to these advantages, there is growing interest in using rare earth (RE)-doped fluorides as VUV scintillators.

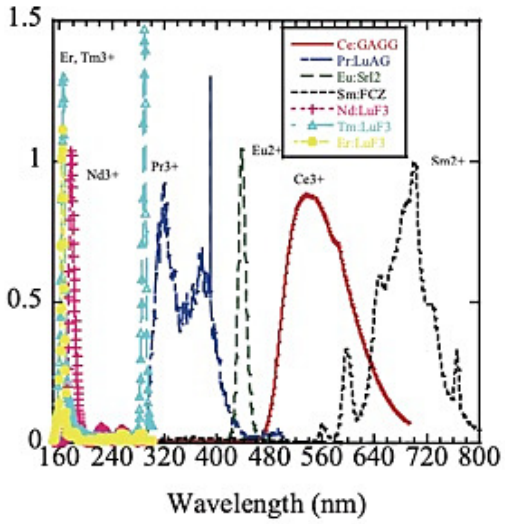

Figure 1.16: Scintillation spectra of N^{3+}-, Er^{3+}- and Tm^{3+}-doped LuF_3 [**?**], Ce-doped GAGG [**?**], Pr-doped LuAG [**?**], Eu-doped SrI_2 [**?**], and Sm-doped FCZ glass-ceramics [**?**].

The chemical formula of the compound used must also be taken into consideration. For instance, when detecting high-energy photons like X-rays and γ-rays, it is preferable to use dense materials composed of high Z_{eff} (effective atomic number). This is because the three types of interactions with matter (photoelectric absorption, Compton scattering, and pair creation) and their interaction probabilities depend on $\sim \rho\ Z_{eff}^4$, $\rho\ Z_{eff}$, and $\rho\ Z_{eff}^2$, respectively. The effective atomic number can be expressed as:

$$Z_{eff} = \left(\Sigma w_i Z_i^4\right)^{\frac{1}{4}} \tag{1.10}$$

where w_i and Z_i represent the fraction of the total mass associated with the i-th element and the atomic number of the i-th element, respectively. In dosimeter applications, the power of Z_i may sometimes be assigned a value of 2.94. Therefore, empirically, powers of 3-4 are commonly used, with the specific value depending on the application.

For neutron detection, materials consisting of light elements are employed. Additionally, inclusion of ^{6}Li or ^{10}B in the matrix is necessary as these elements have a high cross-section for thermal neutrons. In this regard, $20\,Al(PO_3)_3 - 80\,LiF$ (APLF) glass or $LiCaAlF_6$ crystals have been developed for neutron detectors. These materials offer the advantages of

non-hygroscopicity and a high scintillation light yield when doped with Eu^{2+} as an emission center. Pulse-shape discrimination is achievable through doping with Ce^{3+} ions. The same applies to Pr^{3+} ions, as demonstrated in a Pr^{3+}-doped APLF glass shown in Fig. 1.17 [**?**].

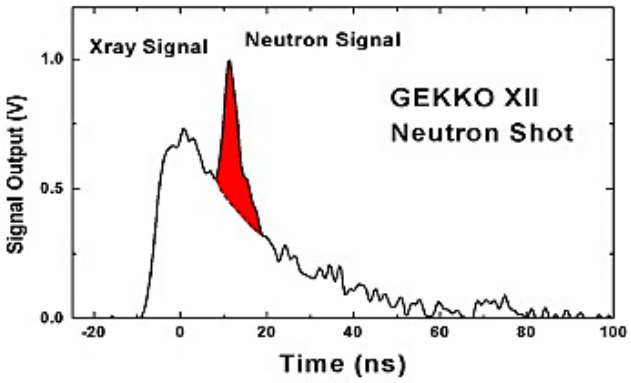

Figure 1.17: The neutron signal detected at about 12 ns using APLF80 + 3Pr scintillator glass at the GEKKO XII facility of the Institute of Laser Engineering, Osaka University [**?**].

On the other hand, charged-particle detectors are primarily utilized for detecting α rays, which have a high interaction probability with most materials. To avoid detecting background photons and neutrons in the measurement environment of charged particles, materials with intermediate Z_{eff} are preferred. Elements with Z values ranging from 10 to 30 are suitable candidates for this purpose. In addition, high energy resolution is required to distinguish between different radioisotopes [**?**]. Consequently, scintillator materials must possess high transparency. Ce^{3+}-doped CaF_2 crystals meet these criteria. These crystals exhibit luminescence in the UV region over a wide range of Ce concentrations. When optically excited within the 290 to 310-nm range, the decay constant of Ce^{3+}-doped CaF_2 crystals is less than 60 ns, and this decay becomes even faster as the Ce concentration increases (Fig. 1.18).

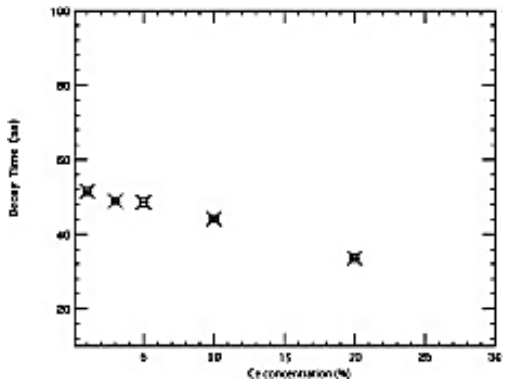

Figure 1.18: Dependence of the decay time constant of the Ce-doped CaF_2 crystals on the Ce dopant concentration [**?**].

Furthermore, under X-ray excitation, Ce^{3+}-doped CaF_2 crystals also exhibit emissions in the 300 to 360-nm range, as shown in Fig. 1.19. However, the decay time constants for these emissions are slightly slower than those observed under optical excitation, differing by a few ns. In the figure, the luminescence at 270 nm in low Ce concentration samples was due to self-trapped exciton, while the sharp line around 300 nm in the 20% Ce-doped sample was noise caused by a direct hit of X-ray or background cosmic ray to the CCD.

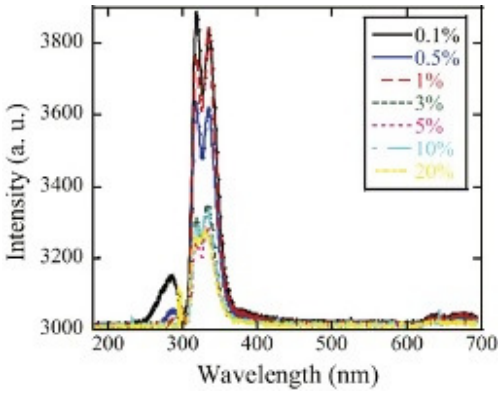

Figure 1.19: X-ray induced radioluminescence spectra of Ce-doped CaF_2 scintillators in the wavelength range from 180 to 700 nm. The supplied bias voltage and tube current were 80 kV and 1 mA, respectively. The X-ray exposure time was 10 s for each integration. [**?**].

Additionally, Ce^{3+}-doped CaF_2 crystals have been demonstrated to effectively discriminate alpha rays. The inset in the pulse height spectrum in Fig. 1.20 shows the full energy peak of an α ray for a 0.1 mol% Ce-doped

sample when irradiated with 5.5 MeV α rays from 241Am. Considering the quantum efficiency of the used PMT around 320 nm, the scintillation light yield monotonically decreases with increasing Ce concentrations. The highest light yield is exhibited by a moderately-doped CaF_2 crystal.

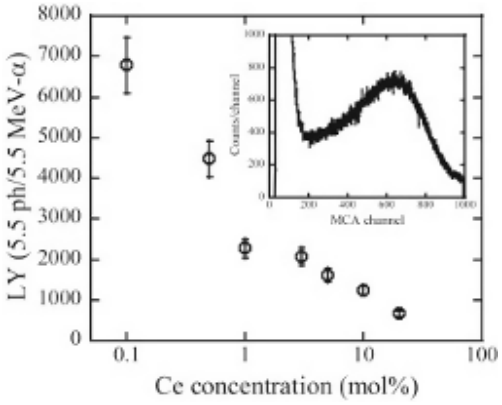

Figure 1.20: Scintillation light yield plotted against Ce concentrations. The inset shows 241Am a-ray spectrum of Ce 0.1% doped CaF2. The shaping time was 2 ms and 5.5 MeV peak channel was determined by a single gaussian fitting. [**?**].

In high counting-rate applications such as positron emission tomography (PET), the timing resolution is a crucial consideration. The timing resolution is determined by the combination of a scintillator, photodetector, and readout electronics. When it comes to scintillator materials, the timing resolution primarily relies on the number of scintillation photons emitted by the fast component. The presence of a slow component can degrade the timing resolution.

On the detector side, it is important that the spectrum of incident photons matches the spectral sensitivity of the photodetector. This ensures that the fast component can be effectively detected and converted into an electrical signal. Furthermore, the response time of the photodetector should be well-matched to the desired timing resolution.

1.4 The CaF_2 crystal

Calcium fluoride (CaF_2) is an ionic crystal with a fluorite structure that crystallizes in the cubic $Fm\bar{3}m$ space group. The crystal structure consists of F^- ions forming a simple cubic lattice, with Ca^{2+} ions present in every

second cube (see Fig. 1.21). The empty cubes serve as interstitial sites for impurities and dopants, and play a crucial role in defect formation and diffusion. Additionally, the crystal structure can be described as having F^- ions bonded to four equivalent Ca^{2+} atoms, forming a combination of corner and edge-sharing FCa_4 tetrahedra. The lattice constant of CaF_2 is 5.4626 Å, and the Ca^{2+} ions are bonded to all eight F^- ions at an equal distance of 2.39 Å [**?**].

However, despite the simple crystal structure of CaF_2 host crystal, the interpretation of its Ce ion's crystal field splitting is complicated by the presence of multitude of absorption bands where only one or two are expected. When doped with Ce^{3+} ions, CaF_2 crystals exhibit wide transparency in the UV to IR region and have shorter radiative lifetimes. This makes them suitable for scintillator applications, particularly for the detection of events such as X-rays and α rays that require fast temporal resolution. CaF_2 crystals also possess excellent physical properties, including good thermal conductivity, high radiation resistance, and a low refractive index. Due to the presence of only one metal ion (calcium) in the crystal and its comparable ionic radius to that of Ca^{2+}, the substitution of Ce^{3+} ions at the calcium site is favored structurally. Despite this, the interpretation of the crystal field splitting of its Ce^{3+} ions is complicated by the presence of multiple absorption bands, where only one or two are expected.

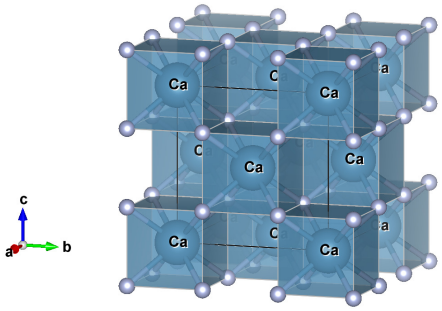

Figure 1.21: Crystal structure of CaF_2 crystal

Extensive absorption and photoluminescence (PL) studies have been conducted to investigate the influence of Ce^{3+} doping concentration on the absorption bands. Loh *et al* have reported absorption bands centered around 215 nm and 245 nm, which increase steadily with increasing nominal doping concentration from 0.005 to 5 mol% (see Fig. 1.22) [**?**]. In contrast,

the emission band shape at 290-310 nm in the radioluminescence spectra (see Fig. 1.23) showed no significant change [**?**]. The reported decay time is approximately 40 ns [**? ?**]. Numerical calculations have been employed to match the optically observed absorption bands with the crystal field splitting of Ce^{3+} ions in specific site symmetries, such as tetragonal and trigonal symmetry [**? ? ?**]. Advanced techniques, including electron paramagnetic resonance (EPR), have also been utilized to investigate the mechanism of charge compensation [**? ? ?**]. EPR is sensitive to the various local site symmetries of the Ce^{3+} ion and has successfully provided insights into the CaF_2 crystal. These studies collectively support the notion that the complex absorption bands arise due to the co-existence of Ce^{3+} centers with various site symmetries.

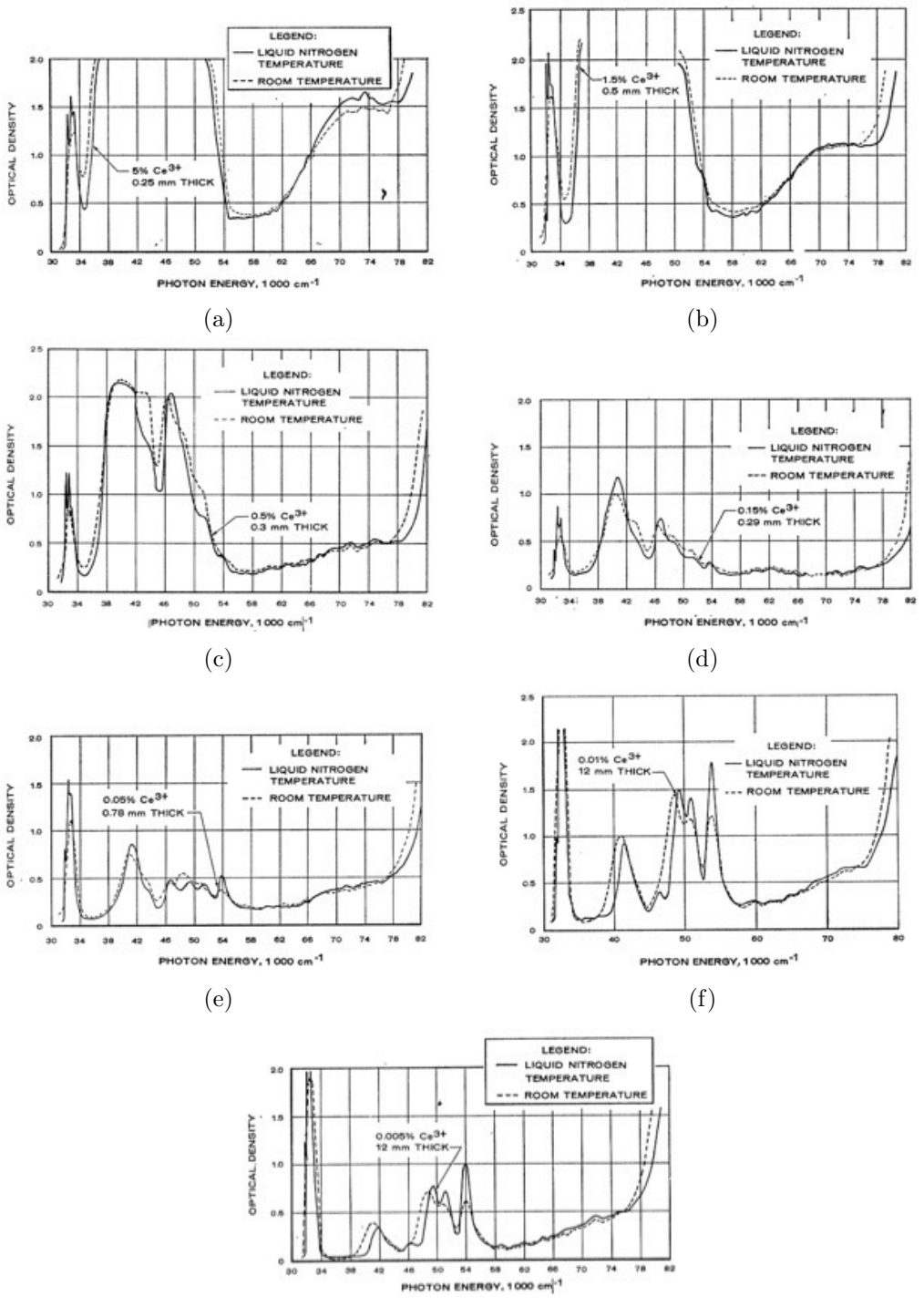

Figure 1.22: Ultraviolet absorption spectra of Ce^{3+} in CaF_2 crystal under varying Ce^{3+} concentrations from 0.005% to 5% at room and liquid-nitrogen temperature as reported in Ref. [**?**].

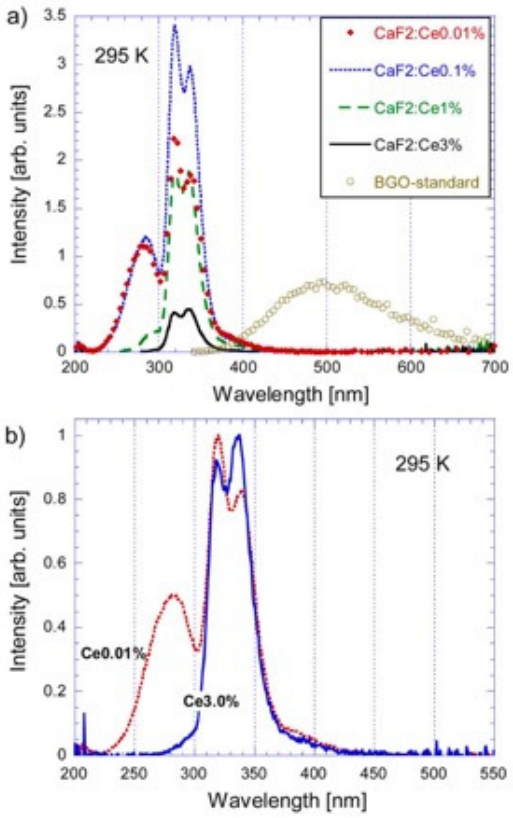

Figure 1.23: (a) Absolute radioluminescence spectra of the CaF_2:Ce sample using 25-kV X-ray tube source and (b) Normalized radioluminescence spectra for the limit Ce concentrations. The emission band at 280 nm, which is gradually suppressed with increasing Ce concentration and completely dumped at 3% concentration, is from self-trapped exciton as reported in Ref. [**?**].

Doping a divalent calcium ion (Ca^{2+}) with a trivalent cerium ion (Ce^{3+}) requires charge compensation. This can be achieved by introduction of an interstitial fluoride ion (F^-) into the nearest or remote empty lattice cube. If the charge compensation is too far away, the original cubic symmetry (O_h) can be maintained. However, if the compensation is closer, the symmetry can be reduced to either tetragonal (C_{4v}), trigonal (C_{3v}), or other symmetries, depending on the location of the charge compensator.

Figure 1.24 shows the optimized local structures of Ce^{3+} ions in CaF_2, obtained from DFT calculations [**?**]. The figure illustrates the possible locations of local charge compensation by interstitial F^- ions and O_F substituents, along with their corresponding symmetries. When an interstitial F^- ion is positioned at ($\frac{1}{2}$, 0, 0), typically originating from randomly dis-

tributed single Ce^{3+} ions, tetragonal C_{4v} symmetry is formed. On the other hand, if the interstitial F^- ion is located at $(\frac{1}{2}, \frac{1}{2}, \frac{1}{2})$, trigonal C_{3v} symmetry is formed. Trigonal C_{3v} symmetry becomes more favored as the concentration of Ce increases. At high concentrations, the Ce^{3+} ions tend to diffuse and cluster together with their charge compensators. Therefore, the absorption band at 240 nm can be attributed to the cluster-ion Ce^{3+} center C_{3v} F_i' (111), as its variation is observed with Ce^{3+} doping concentration. The absorption bands in the range of 190 to 210 nm and at 304 nm are ascribed to the dominant center, the single-ion $Ce^{3+}C_{4v}$ F_i' (100), as these bands persist with varying doping concentrations.

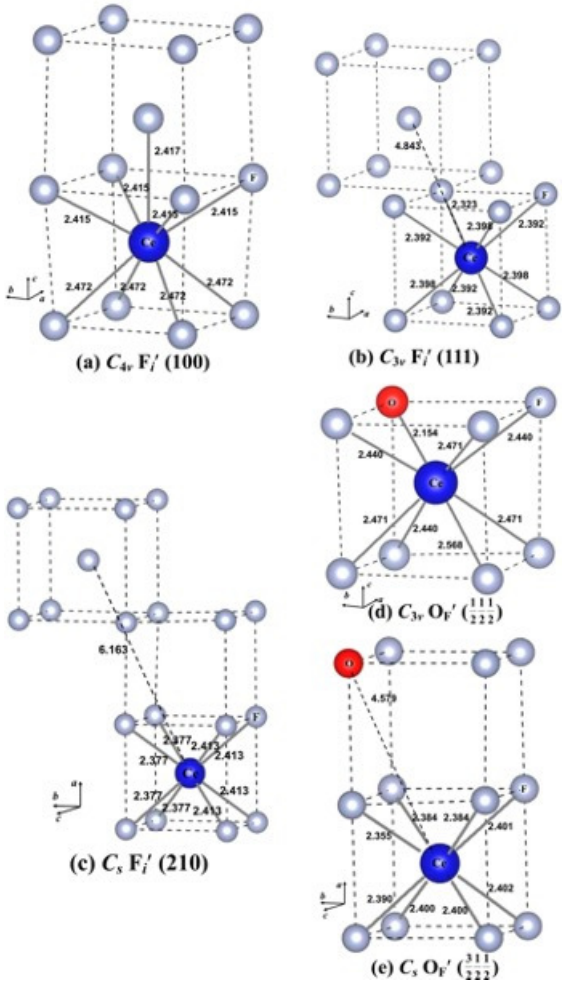

Figure 1.24: Optimized local structures from DFT-PBE calculations of Ce^{3+} in CaF_2 with a local charge compensation by interstitial F^- ions and O_F substituents published in Ref. [**?**]. The point group symmetries and the values of selected distances are indicated.

The interpretation of the complex absorption spectrum of the Ce-doped CaF_2 has not been satisfactory yet. The calculated 5d levels of the Ce^{3+} ion with different site symmetries are nearly coincident, making their symmetry assignments ambiguous when using common absorption spectroscopy setups. For example, as shown in Table 1.5, one calculated 5d band of the single-ion Ce^{3+} center C_{4v} F_i' (100) remains missing, even with high-resolution and low-temperature (liquid helium) optical measurements [**?** **?** **?**]. However, according to theory, there should be a total of five 5d energy levels split by the C_{4v} crystal field and the spin-orbit interaction, resulting in the remaining degeneracy being Kramer's degeneracy. This missing level is assumed, at best, to coincide with the 240-nm absorption band of the cluster-ion Ce^{3+} center C_{3v} F_i' (111).

Table 1.5: Calculated $4\,f^1$ and $5\,d^1$ energy levels and 4f→5d relative transition intensities for the tetragonal C_{4v} F_i' (100) center in CaF_2:Ce with and without the effect of spin-orbit coupling (SOC)[a] from Ref. [**?**].

	energy levels				relative transition intensities		
	without SOC	with SOC			$4f_1 \rightarrow 5d_1$	$4f_1 \rightarrow 5d_1$	
	calcd	calcd	exptl[b]	exptl[c]	calcd	calcd	exptl[b]
$4f_1$	0	0	0	0		1.00	1.00
$4f_2$	270	281	110[d]			0.07	0.05
$4f_3$	271	559	579			0.29	0.27
$4f_4$	375	2276	2192	2191		0.63	1.04
$4f_5$	476	2380	2307	2305		0.29	1.37
$4f_6$	670	2635	2440	2824		0.01	0.02
$4f_7$	1614	3325	3562	3562		0.03	0.04
$5d_1$	29683	30714	32350		1.00		
$5d_2$	39370	40285			0.10		
$5d_3$	48043	48992	49490		0.19		
$5d_4$	48673	49961	51160		0.42		
$5d_5$	51569	52946	53370		0.56		

1.5 The $LiCaAlF_6$ and $LiSrAlF_6$ crystals

LiCAF and LiSAF, in their pure crystal form, belong to the *colquirite* $LiMM'F_6$ family of fluoride compounds, where M represents Ca or Sr, and M' represents Al, Ga, or Cr. These crystals have a trigonal crystal structure with a space group of D_{3d}^4 (space symmetry $P\bar{3}1c$) and lattice constants of a=4.996 Å and c=9.636 Å [**?** **?**]. They are optically uniaxial with two formula units per unit cell. Each lithium (Li), calcium (Ca) or strontium (Sr), and aluminum (Al) atom is surrounded by six fluorine (F) atoms, as shown in Figure 1.25. The Li and Al atoms occupy the centers of deformed octahedra with D_3 symmetry, while the Ca or Sr atoms occupy deformed octahedral sites with C_{3i} symmetry. The crystal structure can also be viewed as a two-dimensional arrangement, with alternating $(Li,Al)F_6$ and $(Ca,Sr)F_6$ slabs stacked along the c-axis. The adjacent LiF_6 and AlF_6 octahedra share edges and are connected to the CaF_6 or SrF_6 octahedra by sharing fluorine atoms at their vertices.

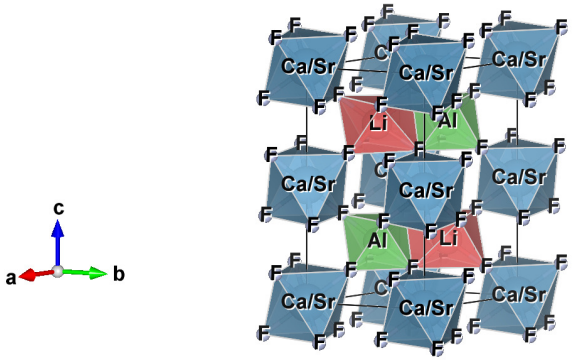

Figure 1.25: Crystal structure of $Li(Ca,Sr)AlF_6$ crystal

In a structural study using single crystal X-ray diffraction (XRD) on pure LiCAF and LiSAF crystals, it was observed that the Sr-F bond lengths were 1.5 Å longer than the Ca-F bond lengths (2.28 Å) [**?**]. The extent of distortions between the SrF_6 and CaF_6 octahedra, described in terms of the F-(Ca, Sr)-F deviation from 90°, was also found to be different. For LiSAF, the F-Sr-F^i and F-Sr-F^{ii} angles were equal to 84.93° and 95.07°, respectively, while for LiCAF, the values were 87.05° and 92.95°, respectively. The interval between the $^2T_{tg}$ levels, derived independently from the absorption spectra of Ce-doped LiCAF and LiSAF crystals, was subsequently correlated to the

expansion of the (Ca,Sr)F_6 octahedra in pure LiCAF and LiSAF crystals, or in other words, to the increase in Ca-F or Sr-F bond lengths. On the other hand, the shifting in the 5d→4f spectrum towards longer wavelengths was correlated to the increase in the F-M-F^{ii} angle.

Based on ionic size, the preferred site of substitution for the Ce^{3+} ion is either the Ca^{2+} or Sr^{2+} site. Often, the octahedra of Ca^{2+} or Sr^{2+} undergo weak distortions, resulting in tetragonal, trigonal, or orthorhombic symmetry. Since Sr^{2+} is larger in size than Ca^{2+}, the CeF_6 octahedra can be more extended in LiSAF, as observed previously [**?**]. This can lead to greater smearing in the absorption, excitation, and emission features, as well as in the Stokes shift [**?**].

The charge difference between the Ce^{3+} ion and the Ca^{2+} or Sr^{2+} ion requires charge compensation, which may involve cation vacancies. The proximity of the cation vacancy can influence the symmetry of the Ce^{3+} ion's octahedron. An electron spin-resonance (ESR) study performed on a Ce^{3+}-doped $LiCaAlF_6$ crystal revealed the presence of at least two distinct Ce^{3+} centers [**?**]. The dominant center has trigonal symmetry, assumed to occur from direct substitution of Ce^{3+} for Ca^{2+}, with a remote charge-compensating Li^+-ion vacancy. The other center is perturbed by a nearby charge-compensating Li^+-ion vacancy, resulting in orthorhombic symmetry. The presence of these centers was then correlated with the anisotropy in the luminescence of Ce:LiCAF crystals. Specifically, the π-component (E‖c) of the crystal's emission spectra exhibits two bands centered at 290 nm and 312 nm, which correspond to the transition from the lowest ^2D excited state to the $^2F_{7/2}$ and $^2F_{5/2}$ ground states of the Ce^{3+} ion, respectively. The σ-component (E‖a) has three bands, two of which are centered at 285 nm and 289 nm, while the third one is centered at 320 nm. The former bands are attributed to the transition from the ^2D state to the split levels of $^2F_{5/2}$, while the latter constitutes the ^2D to $^2F_{7/2}$ transition.

Chapter 2

Purpose and motivation

The optical properties and fluorescence profiles of cerium-activated fluoride crystals, particularly those containing the Ce^{3+} ion, have been extensively studied through optical spectroscopic techniques. However, there is still ongoing debate regarding the mechanisms of luminescence in Ce ions due to the lack of a complete understanding of the relationship between the local structure and the crystal field splitting. The interpretation of the redshift in compounds where the lanthanide ion, such as Ce^{3+}, occupies a divalent or monovalent cation site is further complicated by the need for charge compensation.

For instance, despite the relatively simple crystal structure, significant efforts have been made to interpret the complex absorption bands observed in Ce^{3+}-doped CaF_2. It has been observed that the proximity of charge compensation affects the symmetry of the Ce^{3+} ion's polyhedra. However, the calculated energy levels of the Ce ions do not fully align with the experimentally derived transitions. Additionally, when the compound is treated in an oxygen atmosphere, the zero phonon absorption line measured at low temperatures shifts by 2300 cm^{-1} from 313.2 to 338 nm [**?**]. This shift is quite large for a F^- charge compensator. But one can only surmise that the O^{2-} ion assumes the role of the charge compensator instead of the F^- ion. This discrepancy can be attributed to the larger polarizability of the O^{2-} ion in CaO compared to the F^- ion in CaF_2, as well as the greater covalency between O^{2-} and Ce^{3+} ions.

Furthermore, it has been found that Ce ions can undergo valence changes

between Ce^{3+} and Ce^{4+} when annealed in reducing and oxidizing atmospheres, respectively [**?**]. Studies have also revealed that Ce^{4+} ions can coexist with Ce^{3+} ions in doped crystals and can be stabilized by the addition of divalent ions such as Ca^{2+} and Mg^{2+} [**?**]. The presence of Ce^{4+} ions actually plays a crucial role to the optical mechanism along with the Ce^{3+} luminescent center, and co-doping Ce with divalent alkaline earth ions has been shown to improve emission lifetimes. Another interesting case is the doping of Ce^{3+} ions in NaF. This leads to a significant redshift of 23700 cm^{-1}, which is unusually large for a fluoride compound. However, the presence of two neighboring oxygen ions at the fluoride sites can only be speculated.

Overall, there is limited direct evidence regarding the changes in the oxidation state of Ce ions during annealing, the local structures surrounding Ce ions, and the extent of restructuring in the host lattice when dopants are added and their concentrations are increased. Understanding the relationship between the local structure and crystal field splitting is crucial for the development of Ce-doped fluorides as scintillators and tunable solid-state UV laser materials. Therefore, this study aims to investigate the optical and local structural properties of Ce-doped fluoride crystals for their potential applications as ultrafast and efficient scintillators and high-performing tunable solid-state UV lasers. Specifically, the objectives of this study are as follows:

1. Characterize the optical emission of Ce-doped CaF_2 crystals for scintillator applications.

2. Characterize the optical emissions of Ce-doped $LiCaAlF_6$ and $LiSrAlF_6$ crystals for UV laser applications.

3. Determine the changes in the oxidation state of Ce ions, the local structures surrounding them, and the extent of local restructuring in CaF_2 crystals grown by the Bridgman method, as well as in $LiCaAlF_6$ and $LiSrAlF_6$ crystals grown by the Czochralski method.

4. Propose design considerations for future scintillator devices and tunable solid-state UV lasers.

The choice of fluorite-type CaF_2 and colquiriite-type $LiCaAlF_6$ and $LiSrAlF_6$ crystals for this study is based on their excellent optical characteristics, including wide optical transparency from vacuum ultraviolet (VUV) to infrared (IR), low phonon energy (approximately 300-500 cm^{-1}) [**?** **?**], and low refractive index [**?**]. In addition to these fundamental requirements for optoelectronic devices, the scintillating capability of these crystals has already been demonstrated. Ce-doped CaF_2 crystals exhibit a fast enough lifetime to discriminate alpha rays, while the Li-rich colquiriite-type Ce-doped crystals ($LiCaAlF_6$ and $LiSrAlF_6$) offer a high cross-section for thermal neutrons in neutron diagnostics. These crystals are also among the few that can lase in the UV region. The study will begin with the analysis of the simplest or highest symmetry structure, the fluorite-type CaF_2 crystal, followed by the colquiriite group crystals, $LiCaAlF_6$ and $LiSrAlF_6$, which have a trigonal crystal structure. The local structures and luminescence properties of these three crystals will be discussed in relation to their respective applications. More complex crystal structures, such as $KMgF_3$, where the Ce^{3+} ion is expected to replace the monovalent K^+ ion, will be investigated in future studies.

Chapter 3

Crystal growth techniques

Up until recently, inorganic scintillators were usually in the form of single crystals. These were typically produced by growing techniques from the melt, such as the Czochralski or Bridgman-Stockbarger methods. This chapter gives a brief introduction on how these two techniques are performed.

3.1 The Czochralski method

The Czochralski (CZ) method is the most widely used method for the production of bulk single crystals for a wide range of electronic and optical materials. The method is named after the Polish scientist Jan Czochralski, who developed it in 1916. The Czochralski apparatus is shown in Fig. 3.1. One attaches a seed crystal to the bottom of a vertical arm so that the seed is barely in contact with the material at the surface of the melt. The arm is raised slowly, and a crystal grows underneath at the interface between the crystal and the melt. Usually, the crystal is rotated slowly so that inhomogeneities in the liquid are not replicated in the crystal. Based on measurements of the weight of the crystal during the pulling process, computer-controlled apparatuses can vary the pulling rate to produce any desired diameter. As the seed is extracted, the material solidifies, and eventually, a large circular boule is produced. The Czochralski method is usually used for materials with a high melting point.

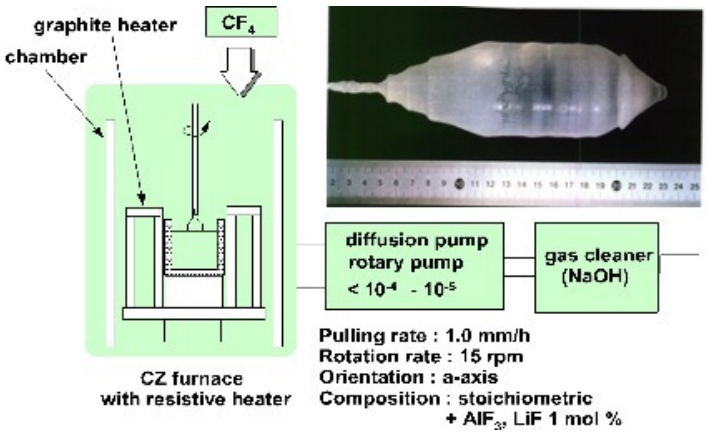

Figure 3.1: Schematic diagram of the CZ process.

Crystal growth of Ce-doped $LiCaAlF_6$ and $LiCaAlF_6$ is usually performed in a CZ system with a resistive heater made of high-purity graphite [**?**]. The starting material is prepared from commercially available CeF_3, LiF, CaF_2 or SrF_2, and AlF_3 powders of high purity ($\geq$ 99.99%) which are then placed in a Pt crucible. Vacuum treatment is performed prior to growth. The system is heated from room temperature to 700°C for a period of 12 h under vacuum (approximately 10^{-3} Pa). Both rotary and diffusion pumps are used to achieve this pressure and effectively eliminate water and oxygen from the growth chamber and the starting material. Subsequently, high purity CF_4 gas (99.99%) is slowly introduced into the furnace. Thereafter, the starting material is melted at approximately 820°C.

3.2 The Bridgman method

The Bridgman technique involves slow cooling of a molten material by moving its container from a hot zone into a cold one, as shown in Fig.3.2. The precursor material used to create the product material is sealed within a crucible or an ampoule and placed in the furnace along with a seed material. The seed crystal is of a known orientation and is placed at the base of the crucible or the ampoule used for crystal growth, facilitating crystal growth in the same orientation as the seed crystal. Heaters maintain the hot zone at a temperature above the melting point of the material. The cold zone, on the other hand, is the outside of the furnace. If a separate furnace is

employed to control the temperature gradient in the cold zone, then it is referred to as the Bridgman-Stockbarger technique.

The precursor material is then melted in the hot zone and translated into the cold zone by motion. The material solidifies as it moves through the temperature gradient in the furnace at a rate that matches the growth of the crystal, so that the interface between crystal and melt is always at the same temperature. For CaF_2 crystal, the rate used is 7.5 mm h^{-1}. A layer of impurities grows at the interface between melt and solid. As this surface moves up, the melt and the impurities become concentrated in the higher part of the crystal. This method is well suited for materials with low melting point and sensitive to air, such as Strontium Iodide. The Bridgman method can be performed in either vertical or horizontal configurations.

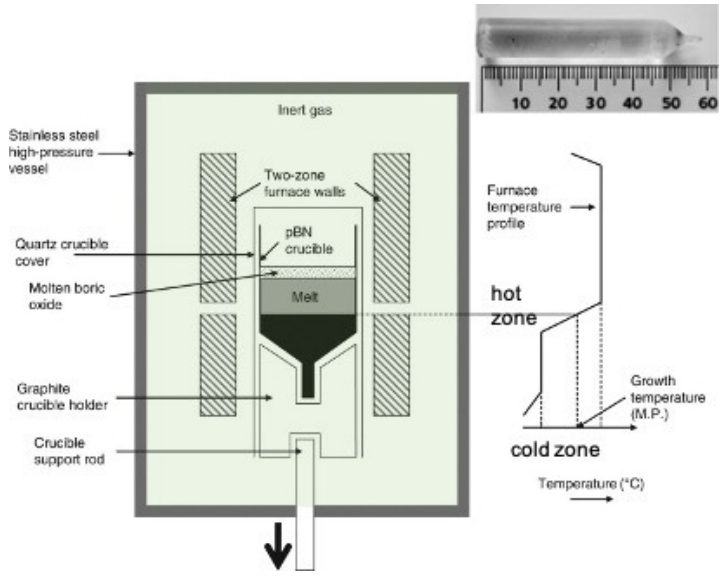

Figure 3.2: Schematic diagram of the Bridgman process and the transparent and colorless as-grown crystal.

To grow CaF_2 crystal, usually the Bridgman–Stockbarger method is operated in a system of nine concentric niobium heat shields [**?**]. The starting material is prepared from commercially available CeF_3, and CaF_2 powders of high purity ($\geq$ 99.99%). The starting material is sealed in a graphite crucible and then melted in the hotzone with maximum temperature of 1600°C. Then, the crucible containing the melt is mechanically removed at a speed of 7.5 mm h^{-1} from the heating zone to where the material cools

down. This will yield a crystal that is optically clear, colourless and easily cleavable.

Chapter 4

Characterization techniques

The characteristics of crystals can be inherent, forming a unique fingerprint, or generated through material design and engineering using various treatment methods. Understanding the chemical and structural properties of crystals is crucial for their applications in different fields. This chapter discusses common techniques, such as photon, neutron, and electron-based methods, for determining the optical and structural properties of materials at an atomic and microscopic scale.

4.1 X-ray absorption spectroscopy

X-ray absorption spectroscopy (XAS) is a widely used technique for analyzing the chemical state of matter and determining its local geometric and electronic structure. XAS experiments are typically conducted at synchrotron radiation facilities, where intense, tunable, and polarized X-ray beams are produced. This technique can be applied to samples in the gas phase, solutions, or solids, and it finds applications in various disciplines, including physics, chemistry, biology, biophysics, medicine, engineering, environmental science, materials science, and geology.

X-rays possess sufficient energy to remove a core electron from an atom, as they are ionizing radiation. Each core shell has a specific binding energy, and plotting X-ray absorption as a function of energy for any atom produces a spectrum resembling the X-ray absorption spectrum for Pb (shown in Figure 4.1 [**? ? ? ?**]). When the X-ray energy is scanned across the binding

energy of a core shell, an abrupt increase in absorption cross-section, known as an absorption edge, is observed. Each edge corresponds to a different core-electron binding energy and is named according to the principle quantum number of the excited electron (e.g., K for n=1, L for n=2, M for n=3, etc.). The core-electron binding energy increases with the atomic number, ranging from 284 eV for the C K edge to 115,606 eV for the U K edge. The L edges have significantly lower energies than their corresponding K edges (e.g., 270 eV for the Cl L_1 edge, 20,948 eV and 17,166 eV for the U L_2 and L_3 edges).

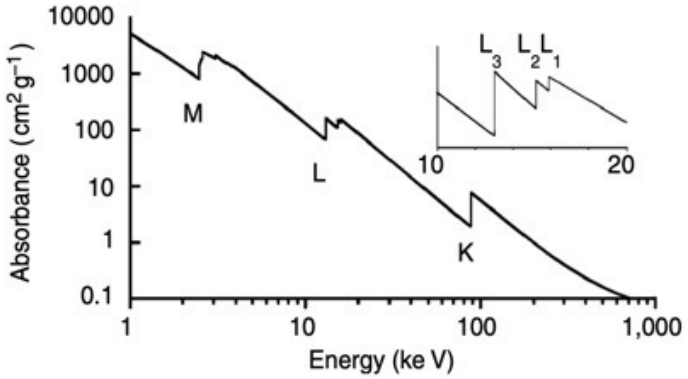

Figure 4.1: Low-resolution X-ray absorption spectrum for Pb. The K, L, and M edge transitions corresponds to excitation of an electron from n=1, 2, and 3 shells, respectively. he L edges (inset) and the M edges are actually further split at higher resolution [**?**].

A closer look at the inset of Fig. 4.1 reveals the L edge is actually composed of three distinct L edges, named L_1, L_2, and L_3 edges in order of decreasing energy. The excitation of a 2s electron corresponds to the L_1 edge. Conversely, the 2p excitation is split into two edges, L_2 and L_3, due to the spin-orbit coupling energy of the $2p^5$ configuration. The higher energy $^2P_{1/2}$ excited state gives rise to the L_2 edge, while the lower energy $^2P_{3/2}$ excited state corresponds to the L_3 edge. Because of degeneracy, the L_3 edge has twice the edge jump of the L_2 and L_1 edges. Spin-orbit coupling for core shells can be quite significant, in contrast to valence electron shells where spin-orbit coupling energies are relatively small. For Pb, the L_2-L_3 splitting is 2,165 eV (1 eV = 8,066 cm^{-1}). Similar, albeit smaller, splittings occur for lower-energy edges such as the 5 M edges, 7 N edges, and so on. Thereby, X-ray absorption spectroscopy (XAS) specifically refers to

the measurement of X-ray absorption cross-section in the vicinity of one or more absorbing edges.

While an absorption edge alone can only provide elemental identification [**?** **?**], a more detailed examination of the edges in Fig. 4.1 can yield a wealth of information. As shown in Fig. 4.2, the absorption edge not only exhibits a discontinuous increase in absorption but also displays significant structures both in the immediate vicinity of the edge jump and well above the edge. The structure in the vicinity of the edge is commonly referred to as X-ray absorption near-edge structure (XANES). The oscillations above the edge, which can extend for 1,000 eV or more, are referred to as extended X-ray absorption fine structure (EXAFS). While the term XAFS (X-ray absorption fine structure) is often used to encompass the entire structured absorption region, the terms XANES and EXAFS are still widely employed, as they are typically analyzed differently. The XANES region is sensitive to oxidation state and geometry, but is not usually analyzed quantitatively. On the other hand, the EXAFS region is sensitive to the radial distribution of electron density around the absorbing atom and is used for the quantitative determination of bond length and coordination number.

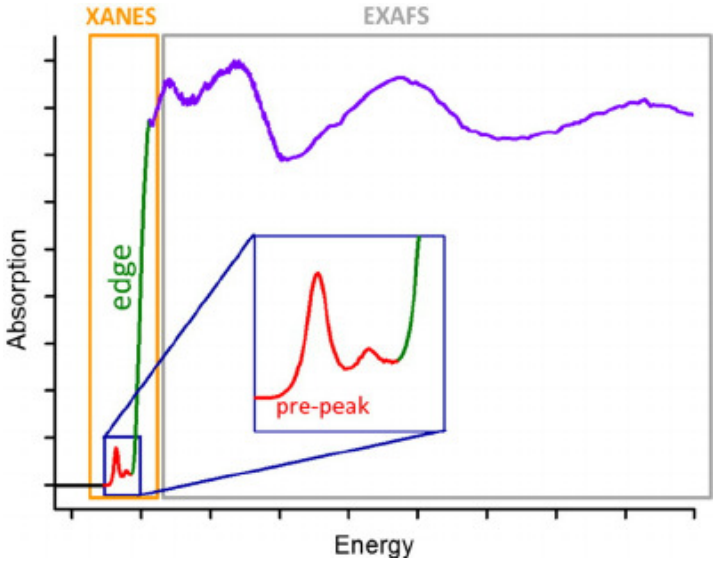

Figure 4.2: Schematic illustration of an X-ray absorption spectrum, showing the structured absorption that is seen both within ≈50 eV of the edge (the XANES) and for several hundred to >1,000 eV above the edge (the EXAFS) [**?**].

Absorption of an ionizing X-ray results in the ejection of a photoelectron,

leaving behind a highly excited core-hole state. This state can relax through various mechanisms, with the main ones being the emission of an Auger electron and X-ray fluorescence. Auger emission dominates when the process involves lower energy excitation, while X-ray fluorescence is the primary relaxation process involved at higher-energy excitation. For instance,, at the K edges of elements with atomic numbers greater than 40, the X-ray fluorescence yield approaches 1. The spectrum for light elements is relatively simple, but for heavy elements, a large number of X-ray emission lines are observed. Some possible emission lines are shown in Fig. 4.3 [**?** **?** **?**]. Like all emission spectroscopy, selection rules apply to X-ray fluorescence, resulting in only certain transitions (diagram lines) being allowed, while a variety of forbidden transitions (non-diagram lines) are also observed. The probability of transition per unit time from an initial state $|i\rangle$ to a final state $|f\rangle$, according to Fermi's Golden Rule, is given by

$$P_{if} = \frac{2\pi}{\hbar} |\langle f|\epsilon I\dot{r}|i\rangle|^2 \rho_f(E) \tag{4.1}$$

where, ϵ is the polarization vector of the electromagnetic wave, and $\epsilon \cdot \mathbf{r}$ is the interaction operator in the dipole approximation. $\rho_f(E)$ represents the energy density of final states. This equation is derived from time-dependent perturbation theory for an atom that is loosely coupled to a classical radiation field [**?**]. The X-ray field is treated as a classical plane wave. As a result, each element has unique "characteristic" X-ray emission energies that can be well resolved from neighboring emission lines [**?** **?** **?**].

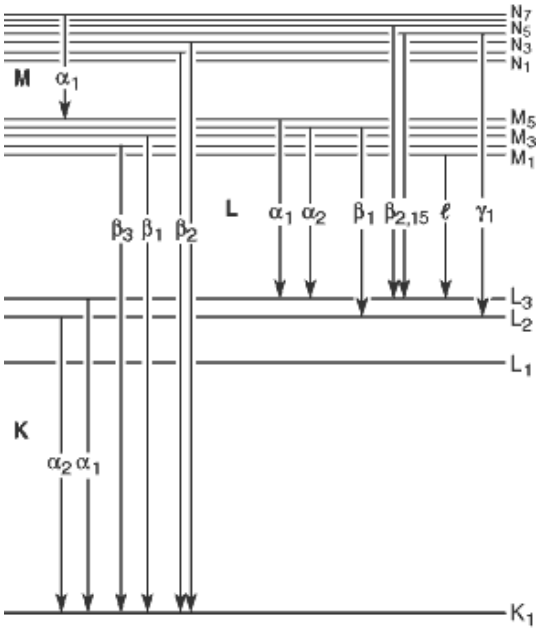

Figure 4.3: Transitions that give rise to the various emission lines. Excitation of a K shell results in K_α and K_β emission lines originating from n=2 and n=3, respectively. At higher resolution, these can be resolved into $K_\alpha 1$ and $K_\alpha 2$, with the splitting due to spin-orbit coupling. L-edge excitation exhibits a similar pattern but with greater complexity [**?**].

Measurement of X-ray absorption spectra

If an X-ray photon travels through a material there's a probability that it will be scattered inelastically by one of its electron or be absorbed by ejecting an electron out of the core of the atom [**?**]. These probabilities themselves will depend on both the energy (E) of the photon and the atomic number (Z) of atoms in the material. In consequence, if a monochromatic X-ray beam passes through a material, its intensity I decreases exponentially with the distance t traveled inside the sample.

$$I(t) = I_0 \exp -\mu(E)\, t \tag{4.2}$$

The above equation is known as the Beer-Lambert's law. I_0 is the intensity of the initial beam and μ is the attenuation coefficient which depends on the X-ray energy (E), atomic number (Z), density (ρ), and atomic mass (A).

$$\mu \approx \frac{\rho Z^4}{AE^3} \tag{4.3}$$

In the simplest case, a XAS experiment involves the measurement of the incident and the transmitted X-ray flux using an ionization chamber in front and behind the sample as shown in Fig. 4.4 [**?**]. Beer-Lambert's equation (Eq. 4.2) can be conveniently re-arranged to yield the absorption coefficient of the sample in the absorption mode

$$\mu\left(E\right)t = \alpha = \ln\frac{I_0}{I_1} \tag{4.4}$$

However, this approach is limited to moderately concentrated samples (greater than 10 mM or ≈500 ppm). To overcome this limitation, XAS spectra can be measured in fluorescence mode [**?**]. This is particularly applicable to dilute samples such as catalysts, biological samples, or environmental samples. As shown in Fig. 4.4, the fluorescence detector is typically positioned at a 45° angle from the surface of the sample. As long as the sample is dilute (with absorbance due to the element of interest being much smaller than the background absorbance) or thin (with total absorbance [**?**]), the intensity of the fluorescence X-rays is directly proportional to the X-ray absorption cross-section [**?**].

$$\alpha = \frac{I_F}{I_0} \tag{4.5}$$

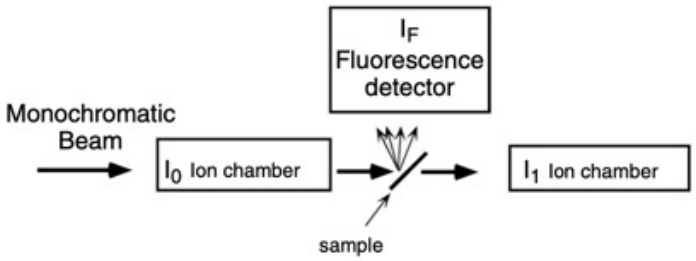

Figure 4.4: Typical experimental setup for XAS measurements.

The sample also emits a variety of X-rays, including the fluorescence X-rays of interest and a background of scattered X-rays. To ensure good sensitivity, the fluorescence detector requires some form of energy resolution

to distinguish between the signal and background X-rays. Energy dispersive Si(Li)-detectors, scintillation counters, or gas-filled proportional counters can be used to discriminate the sample fluorescence from the background signal. Photodiodes, channeltrons, and channel plates are also commonly employed for detection.

X-ray absorption near edge spectroscopy

XANES exhibits characteristic features that depend on the coordination of the absorber atom. Increasing the oxidation state of the absorber shifts the position of the absorption edge in the XANES to higher energies. This is illustrated in Fig. 4.5 for various Manganese compounds [**?**]. The linear relationship between the edge and the valence state of the atom can be qualitatively understood through screening effects. The radial distribution of valence-electron charges contributes to the screening of the nuclear charge, even in the vicinity of the nucleus. The transfer of valence electrons to the ligands reduces this screening effect. As a consequence, the core electrons become less screened, leading to stronger attraction to the nucleus and requiring more energy to bring them to an excited state. The sample's absorption edge is compared with systematic series of model complexes, for which the variations in geometric and electronic structural parameters are known. This allows for the correlation of the observed spectral changes with oxidation state trends.

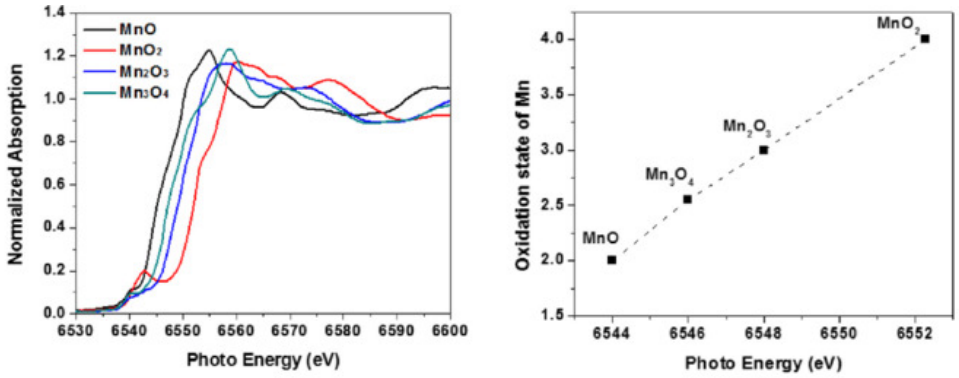

Figure 4.5: K-edge XANES of manganese oxides illustrating the almost linear correlation between the oxidation state and the edge position, where an increase of the oxidation state shifts the absorption edge to a higher energy. [**?**].

Occasionally, peaks in the pre-edge region can also be observed near the

onset of the absorption edge ,which are sensitive to the symmetry of the system. These peaks may arise from quadrupole transitions (s→d at the K or L_1 edge or p→f at the $L_{2,3}$ edges) to empty bound states. The selection rule for these to be allowed is $\Delta l = \pm 2$. However, quadrupole transitions are generally very weak, representing less than 5% of the edge intensity. But, for transition metal compounds, the pre-edge peaks are sometimes quite strong. For example, tetrahedral systems 3d and 4p orbitals mix by symmetry, allowing for the pre-edge to gain intensity due to dipole allowed contributions. These peaks are attributed to p-d hybridization (e.g., 3d and 4p orbitals in tetrahedral systems) resulting from the interaction with ligands. In this case, the transitions become dipole allowed due to orbital mixing [**?** **?**].

Most studies on metals are conducted at the K-edge due to the ease of analysis. However, it is worth mentioning that studies can also be carried out at the L-edges, which result from dipole allowed 2p to 3d transitions (for 3d metals) (see Fig. 4.3). In comparison to the K-edge, L-edge spectra provide 3-5 times better energy resolution, resulting in sharper spectrum features [**?** **?**]. However, the interpretation of L-edge XAS is much more complex than that of the K-edge. For complexes with one or more 3d holes in the 2p core excited configuration, the analysis requires the consideration of multiplet effects, including 2p-3d exchange, as well as both 3d-3d and 2p-3d Coulomb repulsion, 2p final state spin-orbit coupling, and 3d spin-orbit coupling [**?**].

As the L-edge absorption originates from a 2p core electron localized on the metal, and the p→d transition is electric dipole allowed, only transitions to the metal d components of valence holes have transition final state intensity. Hence the integrated intensity of the L-edge absorption can be directly related to covalency (ligand character in the metal valence orbitals) via the normalized ground state wavefunction, expressed as a linear combination of the metal and ligand orbitals:

The L-edge involves an electric dipole allowed transition. Unlike the K pre-edge, it is insensitive to 3d-4p mixing. Thus, the total-integrated L-edge intensity is proportional to the metal 3d character in all unoccupied valence orbitals, regardless of the crystal field. This makes L-edge XAS a precise probe of covalency in transition metal sites. Since the L-edge

absorption originates from a 2p core electron localized on the metal, and the p→d transition is electric dipole allowed, only transitions to the metal d components of valence holes have transition final state intensity. Hence the integrated intensity of the L-edge absorption can be directly related to covalency (ligand character in the metal valence orbitals) via the normalized ground state wavefunction, expressed as a linear combination of the metal and ligand orbitals:

$$|\chi\rangle = \sqrt{1-\alpha^2}\,|M_{3d}\rangle - \alpha\,|L\rangle \tag{4.6}$$

where M_{3d} is the unoccupied metal 3d orbital, L is the interacting ligand valence orbital and α^2 reflects the covalency of the metal-ligand interaction. One thus needs to include the ligand field splitting of the 3d orbitals and the 3d orbital covalency, which will vary for the degenerate symmetry blocks of valence d orbitals, i.e. the differential orbital covalency (DOC) [**?**]. This methodology was exploited to determine the covalency of the electron transfer blue Cu^{II} active site of plastocyanin [**? ?**].

Extended X-ray absorption fine structure

The EXAFS region is typically taken starting from 20-30 eV above the edge jump. At these energies, the X-ray-excited photoelectron has significant energy and thus has a de Broglie wavelength that is comparable to the interatomic distances. The EXAFS photo-excitation cross-section is modulated by the interference between the outgoing and the back-scattered photoelectron waves, as illustrated schematically in Fig. 4.6. At energy E_1, the outgoing and the back-scattered X-rays are in phase, resulting in constructive interference and a local maximum in the X-ray photoabsorption cross-section. At a higher X-ray energy (energy E_2), the photoelectron has greater kinetic energy and shorter wavelength, resulting in destructive interference and a local minimum in the photoabsorption cross-section. The physical origin of EXAFS is thus electron scattering, and EXAFS can be thought of as a spectroscopically detected scattering method, rather than as a more conventional spectroscopy.

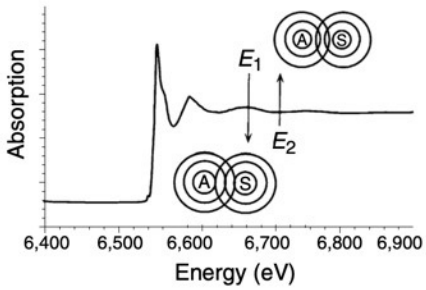

Figure 4.6: Modulation of EXAFS photo-excitation cross-section by the interference between the outgoing and the back-scattered photoelectron waves.

For a single absorber-scatterer pair (for example, in a diatomic gas), this alternating interference will give rise to sinusoidal oscillations in the absorption coefficient where the energy is given in units proportional to the inverse photoelectron wavelength. The photoelectron wavevector, k, is mathematically defined as:

$$k = \sqrt{\frac{2m_e\left(E - E_0\right)}{h^2}} \tag{4.7}$$

where the threshold energy, E_0, represents the binding energy of the photoelectron, also known as the absorption edge.

In most cases, the X-ray excited photoelectron actually undergo multiple scattering prior to returning to the absorbing atom. The EXAFS signal χ(k) can then be described more accurately by including the signal due to a number of scattering paths of the photo-electron, i.e.

$$\chi\left(k\right) = -k\sum_{i=1} S_0^2 N_i \frac{f_i^{eff}\left(k\right)}{R_i^2} e^{-\frac{R_i}{\lambda}} \sin\left(2kR_i + 2\phi\left(k\right)\right) e^{-\frac{\sigma^2 k^2}{2}} \tag{4.8}$$

where the sum over i represents a summation of unique scattering paths of the photoelectron, while the independent variable k is the photoelectron wavenumber described in Eq. 4.7. Multiple scattering is particularly important at low k values, where the photoelectron has very low energy and consequently travels a long mean-free path, allowing for extensive multiple scattering. Multiple scattering is especially pronounced when the two scattering atoms are nearly collinear, as the photoelectron experiences strong scattering in the forward direction. In such cases, the EXAFS

oscillations resulting from the multiple scattering pathway (absorber → scatterer 1 → scatterer 2 → scatterer 1 → absorber in Fig. 4.7) can be up to an order of magnitude stronger than those arising from the single scattering pathway (absorber → scatterer 2 → absorber) [**?** **?** **?**]. Multiple scattering has the potential to introduce significant errors in both the amplitude and phase of the EXAFS signal. If left unaccounted for, these errors can impact the determination of coordination number and bond length.

Figure 4.7: Illustration of single scattering (dashed line) and multiple scattering (solid lines) pathways where the absorbing atom A is surrounded by two scattering atoms, S_1 and S_2 [**?**].

The parameters of the EXAFS equation above (Eq. 4.8) are as follows. First, R_i represents the half path length, which is equal to the bond length in the case of single scattering. Next, N_i denotes the path degeneracy and is related to the coordination number in single scattering scenarios. The scattering amplitude $|f_i^{eff}|$ and phase ϕ_i account for various effects, including the finite extent of scattering potentials and their dependence on scattering angle. The inelastic mean free path λ and the many-body amplitude reduction factor S_0^2 account for the effects of inelastic losses. Finally, the Debye-Waller factor $e^{-\frac{\sigma_i^2 k^2}{2}}$ incorporates the effects of vibrational or static distortion.

The amplitude of the EXAFS oscillations is proportional to the number of scattering atoms, while the frequency of the oscillations is inversely proportional to the distance between the absorber and scatterer. The shape of the oscillations is determined by the energy dependence of the photoelectron scattering, which in turn depends on the identity of the scattering atom. However, to extract chemically relevant information, several other parameters need to be determined or defined. Among these parameters, $\mathrm{f}_i^{eff}(\mathrm{k})$ and $\phi(\mathrm{k})$ play a crucial role. They represent the energy dependence of the photoelectron scattering and the phase shift experienced by the photoelectron wave as it passes through the potential of the absorbing and scattering atoms, respectively. These amplitude and phase parameters

contain the necessary information to identify the scattering atom.

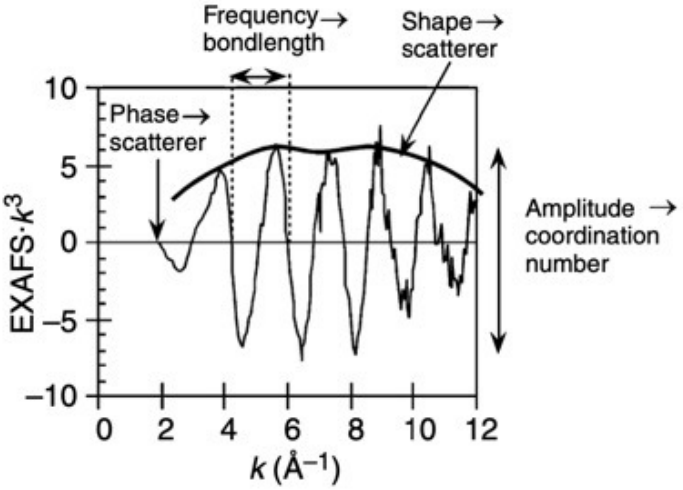

Figure 4.8: EXAFS spectrum as calculated in Eq. 4.8 showing a characteristic "beat" in amplitude at k= $7\mathring{A}^{-1}$ due to the presence of both FeS and FeFe scattering. The structural information of a di-μ-sulfido bridged Fe dimer is encoded in the amplitude, the shape, the phase, and the frequency of the oscillations. Data have been multiplied by k^3 to enhance the oscillations at high k. Noise, which is pronounced at high k for dilute samples, often limits the data to k$\leq 12\mathring{A}^{-1}$ [**?**].

Generally, multiple scattering codes like FEFF (which stands for effective scattering amplitude, f_{eff}) are utilized to calculate the effective scattering phases and amplitudes. Various parameters are employed as fitting variables in this process. Of particular importance are the half path lengths (R) and path degeneracy (N) when dealing with single scattering paths, as these parameters directly correspond to structural properties such as bond length and coordination number. Some of the parameters in the EXAFS equation can also be calculated *ab initio*, while others are obtained by fitting the model to experimental data.

4.2 Optical spectroscopies and other techniques

Optical spectroscopy is a versatile, non-invasive technique widely used to study a range of different materials. It uses light in the UV, visible or infrared (IR) wavelength to determine physical, chemical, or structural

properties of the materials. Ultraviolet-visible (UV-Vis) spectroscopy is categorized such technique. UV-Vis determines and quantifies the chemical properties of a sample using absorbed monochromatic light in the ultraviolet and visible regions.

Generally, when light interacts with an object, it can be absorbed by the object if the wavelength of the incident light corresponds to an electronic excitation within the object. The remaining light is transmitted, meaning it passes through the object. In a spectrophotometer, the transmittance is measured by dividing the intensity spectrum of the transmitted light through a sample (I) by the intensity spectrum of the incident light (I_0).

$$T = \frac{I}{I_0} \tag{4.9}$$

The absorbance (A_0) of the sample is related to I and I_0 according to the following equation:

$$A = \log_{10} \frac{I_0}{I} \tag{4.10}$$

The detector then converts the incoming light into a current which is proportional to the intensity. The absorbance against wavelength (nm) in the UV and visible section of the electromagnetic spectrum are usually plotted for analysis. UV-Vis spectroscopy can also give quantitative information of a given compound or molecule. The mathematical relationships between absorbance, Beer-Lambert's law, the light intensities measured in the instrument, and transmittance is given by:

$$A = \epsilon L c = \log_{10} \frac{I_0}{I} = \log_{10} \frac{1}{T} = -\log_{10} T \tag{4.11}$$

Fourier transform infrared spectroscopy (FTIR) and Raman spectroscopy are categorized under optical spectroscopy technique. These two techniques are complementary to each other and provide fundamental characteristic vibrations that can be used to determine the molecular structure and identify materials [**?**]. They are commonly known as "vibrational" spectroscopy. Raman spectroscopy yields precise results for materials with a crystalline structure, while FTIR is more proficient with amorphous and organic materials. FTIR identifies and quantifies samples based on their vibrational

spectra by utilizing the absorption and emission of light in the infrared region. On the other hand, Raman spectroscopy probes materials using monochromatic laser light, relying on the inelastically scattered light instead of transmitted light as in FTIR. Raman spectroscopy provides information about the chemical structure, including the identity, concentration, phase, morphology, and other properties of the sample. However, Raman spectroscopy is suitable for organic compounds only and cannot be used for fluorescent materials, most metals, and elemental substances.

X-ray diffraction (XRD) is a widely used, non-destructive technique for characterizing minerals with long-range structural order. It has various applications, including determining crystal structure and size, phase identification, crystallographic orientation, lattice parameters, dislocation density, residual stress/strain, phase transformation, and thermal expansion coefficient. However, XRD does not provide significant information about materials that lack long-range structural order, such as glassy or amorphous materials. XRD also has a detection limit of approximately 1% by volume, i.e., if a compound is present in a sample below this level, no peaks above the noise will be detected in the diffraction pattern. The exact detection limit depends on the density, atomic number (Z), and crystal structure of the compounds in the sample. By utilizing tunable and high-intensity X-rays from synchrotrons, smaller and more dilute phases can be analyzed, allowing for the determination of very fine structures, crystal defects, and plastic deformation in minerals [**? ? ?**].

XRD has an electron diffraction counterpart, which offers a spatial resolution of $1\mathring{A}$ with the most advanced electron microscopes. However, for a detectable signal, the region of interest must be no more than a few atomic layers thick. Neutron diffraction is another valuable complementary technique to XRD. Neutron diffraction is suitable for characterizing compounds involving light elements. However, the diffraction of neutrons by crystals is generally weak, requiring very large samples (greater than 1 mm^3) compared to XRD, which can analyze single crystals as small as 2×10^{-4} mm^3.

Nuclear magnetic resonance (NMR) spectroscopy can also be used to describe the structure and dynamics of various molecular and macromolecular systems. NMR is a physicochemical analysis technique that is based on the

interaction between externally applied radio frequency radiation and atomic nuclei. This interaction results in an exchange of energy, causing a change in a property of atomic nuclei known as nuclear spin. NMR is capable of directly measuring the three-dimensional structure of macromolecules in their natural state, even achieving a resolution as low as sub-nanometer in solution. Moreover, NMR provides unique information about dynamics and intermolecular interactions. However, interpreting the NMR spectrum can be complex and challenging. Additionally, this technique requires a substantial amount of pure samples in order to achieve a reasonable signal-to-noise ratio [**?**].

X-ray photoelectron spectroscopy (XPS) is a surface sensitive and non-destructive technique used to analyze the outermost ∼10 nm (∼30 atomic layers) of natural and engineered materials. XPS is commonly used to characterize the surfaces of a wide range of materials, including inorganic compounds (minerals), semiconductors, organic compounds, and thin films and coatings on natural and engineered materials. XPS has a counterpart called energy dispersive spectroscopy (EDX/EDS), which measures X-rays emitted from a sample while XPS measures photoelectrons. In EDX/EDS, the excitation volumes can extend as much as 3 microns into the material. However, similar to electron diffraction techniques, the surface composition and chemistry determined by these methods, may differ from the "bulk" composition of the material.

4.3 *Ab initio* methods

4.3.1 DFT calculation

Density-functional theory (DFT) reframes the problem of calculating electronic properties in terms of the ground state electron density instead of the traditional electronic wavefunctions. Traditional electronic structure methods attempt to find approximate solutions to the Schrödinger equation of N interacting electrons moving in an external electrostatic potential (typically the Coulomb potential generated by the atomic nuclei). However, there are serious limitations to this approach: (1) the problem is highly nontrivial, even for very small numbers N, and the resulting wave

functions are complicated objects, and (2) the computational effort grows very rapidly with increasing N, making the description of larger systems prohibitive. A different approach is taken in density functional theory where, instead of the many-body wave function, the one-body density is used as the fundamental variable. Since the density $n(r)$ is a function of only three spatial coordinates (rather than the 3N coordinates of the wave function), density-functional theory is computationally feasible even for large systems.

The most computationally challenging energy contributions in DFT are the kinetic energy and the exchange-correlation energy [**?**]. The kinetic energy is calculated using the Kohn-Sham orbitals [**?**]. These orbitals, although orthonormal, do not represent the actual electron orbitals. Instead, they map the system of interacting electrons onto a system of non-interacting electrons moving in an effective potential. Conversely, the exchange-correlation energy accounts for two important interactions: the exchange interaction caused by the repulsion between electrons with parallel spins, and the correlation interaction, which describes the correlated motion between electrons of antiparallel spins due to their mutual Coulombic repulsion.

In its simplest implementation, exchange-correlation effects are treated via the Perdew, Burke, and Ernzerhof (PBE) implementation of the generalized gradient approximation (GGA)[**?** **?**]. GGA builds upon the local density approximation (LDA) by considering both the local electron density and its gradient, as the electron density can vary rapidly within a small region of space. However, GGAs have known limitations. They often underestimate band gaps in most semiconductors and insulators [**?** **?**]. Additionally, they can produce incorrect predictions of metallic or very small band-gap semiconducting states in Mott insulators. For example, in the case of undoped cuprates like La_2CuO_4 and $CaCuO_2$, GGA would yield an incorrect nonmagnetic ground state instead of the actual antiferromagnetic insulating state. Despite these issues, GGAs are still widely used because it yields extremely useful total energies and structural properties for a wide range of materials.

Kohn Sham (KS) Formulation

In 1965, Kohn and Sham introduced an artificial system of non-interacting electrons with the same ground state electron density as the many-body Schrödinger equation [25]. Instead of using the fully interacting multi-electron wavefunctions, the KS formulation resorts to single-particle wavefunctions for solving the many-body problem. The Kohn-Sham Hamiltonian is just an extension of Hartree-Fock Hamiltonian but it implicitly assumes that $\hat{\mathcal{T}}$ is the kinetic energy operator of non-interacting electrons which neglects the correlation of the interacting system. The kinetic energy of the real interacting system can be rewritten as

$$\hat{\mathcal{T}} = \hat{\mathcal{T}}_{KS} + \hat{\mathcal{V}}_c \tag{4.12}$$

where $\hat{\mathcal{T}}_{KS}$ is kinetic energy of the non-interacting electron, and $\hat{\mathcal{V}}_c$ is the correlation energy that measures how much movement of one electron is influenced by the presence of other electrons. The total KS Hamiltonian has the form

$$\hat{\mathcal{H}}_{KS} = \left(\hat{\mathcal{T}}_{KS} + \hat{\mathcal{V}}_c\right) + \hat{\mathcal{V}}_{ext} + \hat{\mathcal{V}}_H + \hat{\mathcal{V}}_x \tag{4.13}$$

$$= \hat{\mathcal{T}}_{KS} + \hat{\mathcal{V}}_{ext} + \hat{\mathcal{V}}_H + \hat{\mathcal{V}}_{xc} \tag{4.14}$$

where $\hat{\mathcal{V}}_{xc} = \hat{\mathcal{V}}_x + \hat{\mathcal{V}}_c$ is the combined exchange-correlation energy. The difference between Hartree Hamiltonian from Hartree-Fock Hamiltonian gives the exchange term while the difference between Hartree-Fock Hamiltonian and Kohn-Sham Hamiltonian gives the correlation term [72].

The exact ground state density $\rho(\vec{p})$ of an N-electron system is formulated as

$$\rho\left(r\right) = \left[\sum_{i=1}^{\infty} \phi_i\left(\vec{r}\right) * \phi_i\left(\vec{r}\right)\right] \tag{4.15}$$

where the single-particle KS orbitals $\phi_i\left(\vec{r}\right)$ are the N lowest energy solutions of the Kohn-Sham equation

$$\hat{\mathcal{H}}_{KS}\phi_i\left(\vec{r}\right) = \epsilon_i\phi_i\left(\vec{r}\right) \tag{4.16}$$

Self Consistent Field (SCF) Calculation

In order to solve the KS equation (3.34), the Hamiltonian $\hat{\mathcal{H}}_{KS}$ must be known first. However, the Hamiltonian can only be solved from single-particle KS orbital $\phi_i(\vec{r})$ given in Eq. 4.15. The orbital $\phi_i(\vec{r})$ in turn is calculated from the KS equation leading to an infinite loop as shown in Fig. 4.9.

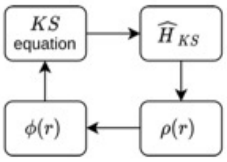

Figure 4.9: Solving Kohn-Sham equation leads to a circular argument.

To circumvent this infinite looping, a trial electron density is introduced, and the KS equation is solved iteratively until convergence is achieved. This iterative process is known as a Self Consistent Field (SCF) calculation [**?**]. Specific steps are illustrated in Fig. 4.10.

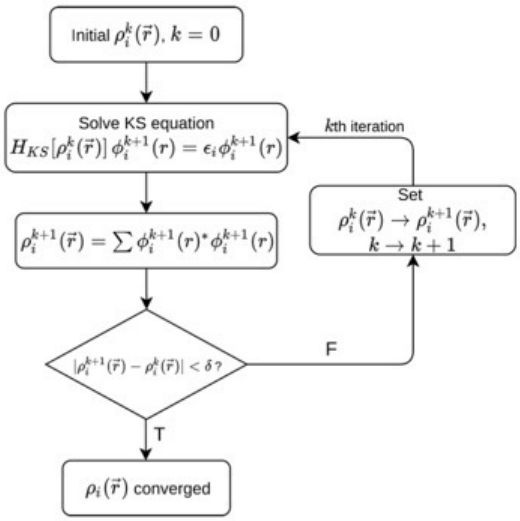

Figure 4.10: Convergence of electron density and other observable quantities using Self Consistent Field calculation.

Local Density Approximation (LDA)

The simplest and commonly used exchange-correlation functional is called Local Density Approximation (LDA). LDA assumes that the electronic

contribution to the exchange-correlation energy from each point in space is the same as to what it would be for a homogeneous electron gas with the uniform density throughout the whole system. The exchange-correlation energy functional is given by

$$E_{xc}^{LDA}\left[\rho\left(r\right)\right] = \int \rho\left(\vec{r}\right)\epsilon_{xc}\left[\rho\left(\vec{r}\right)\right]\, d^3x \tag{4.17}$$

where $\epsilon_{xc}\left[\rho\left(\vec{r}\right)\right]$ is the exchange-correlation energy per particle of a uniform electron gas of density $\rho\left(\vec{r}\right)$. The quantity $\epsilon_{xc}\left[\rho\left(\vec{r}\right)\right]$ can be further split into exchange and correlation contributions

$$\epsilon_{xc}\left[\rho\left(\vec{r}\right)\right] = \epsilon_x\left[\rho\left(\vec{r}\right)\right] + \epsilon_c\left[\rho\left(\vec{r}\right)\right] \tag{4.18}$$

where

$$\epsilon_{xc}\left[\rho\left(\vec{r}\right)\right] = -\frac{3}{4}\left(\frac{3}{\pi}\right)^{\frac{1}{3}}\rho\left(\vec{r}\right) \tag{4.19}$$

LDA is expected to perform best for solids with slowly varying densities [**?**], such as nearly-free-electron metals, and worst for inhomogeneous systems like atoms, where the density must continuously approach zero just outside the atom. The partial success of LDA in inhomogeneous systems can be attributed to systematic error cancellation, where the correlation is underestimated but the exchange is overestimated, resulting in a reasonable value for $E_{exchange-correlation}^{LDA}$ [**? ?**]. However, LDA tends to overestimate the cohesive exchange-correlation energy and binding energies for metals and insulators [**? ? ?**], while significantly exaggerating errors for weakly bonded systems such as van der Waals and H-bond systems ([**? ? ?**]. Nevertheless, LDA remains fairly accurate in predicting elastic properties like bulk modulus [**? ?**].

Generalized Gradient Approximation (GGA)

In order to improve the shortcomings of LDA, the Generalized Gradient Approximations (GGA) systematically calculate gradient corrections of the form $|\nabla\rho(\vec{r})|$, $|\nabla\rho(\vec{r})|^2$, $|\nabla^2\rho(\vec{r})|$, etc. to the LDA. Such functionals can be generalized as

$$E_{xc}^{GGA}[\rho] = \int F^{GGA}[\rho(\vec{r}), \nabla\rho(\vec{r})]\ d^3x \tag{4.20}$$

where f^{GGA} is some arbitrary function of electron density and its gradient. GGA functionals are often termed as semi-local because of their $|\nabla\rho(\vec{r})|$ dependence. A more specific form of the GGA functional can be written as [84]

$$E_{xc}^{GGA}[\rho] = \int \rho(\vec{r})\, \epsilon_{xc}[\rho(\vec{r})]\, F_{xc}[s]\ d^3x \tag{4.21}$$

where $epsilon_{xc}[\rho(\vec{r})]$ is the exchange-correlation energy per particle of an electron gas in a uniform electron density $\rho(\vec{r})$ (i.e. similar to LDA). F_{xc} is the enhancement factor that tells how much exchange-correlation energy is enhanced over its LDA value for a given $\rho(\vec{r})$. GGA differs from the LDA functional only by an enhancement factor. Here s is a dimensionless reduced gradient.

$$s = \frac{|\nabla\rho(\vec{r})|}{2(3\pi^2)^{\frac{1}{3}}\,\rho(\vec{r})^{\frac{4}{3}}} \tag{4.22}$$

This factor gives GGA much greater accuracy than LDA [**?**] in terms of total energies, atomization energies, and energy barriers[**? ? ?**]. Some of the popular GGA functionals used in the literature are Perdew-Burke-Ernzerhof (PBE), Becke88 (B), and Perdew-Wang (PW91) [**? ? ?**]. PBE is the simplest among the functionals and has the following exchange enhancement factor

$$F_x^{PBE}[s] = 1 + \kappa - \frac{\kappa}{1 + \frac{\mu s^2}{k}} \tag{4.23}$$

where κ and μ are parameters obtained from physical constraints. When the density gradient approaches to zero ($|\nabla\rho(\vec{r})| \to 0, s \to 0$), PBE(s) will become unity and Eq. 4.21 reduces to LDA formulation.

DFT calculations do not provide exact solutions to the full Schrödinger equation. Although pure DFT can approximate the true ground state energy of a system quite well, it cannot accurately compute excited state energies. Additionally, there are situations where DFT computations yield unphysical results, such as the underestimation of band gaps in semiconductors and

insulators, and the inaccurate modeling of weak Van der Waals attractions. These limitations stem from the density functional formalism, which focuses on electron density rather than wave functions, prompting the exploration of alternative approaches that aim to converge to exact solutions of the Schrödinger equation.

One commonly used computer program for DFT calculations is VASP (the Vienna Ab initio Simulation Package). In VASP, key quantities like one-electron orbitals, electronic charge density, and local potential are expressed using plane wave basis sets. The interactions between ions and electrons are described using norm-conserving or ultra-soft Vanderbilt pseudopotentials (US-PP), or by employing the projector-augmented wave (PAW) method. US-PP and the PAW method allow for a significant reduction in the number of plane waves per atom, particularly for transition metals and first-row elements. VASP enables the calculation of forces and the full stress tensor, which can be used to relax atoms into their ground state configuration. The software employs efficient iterative matrix diagonalization techniques, such as the residual minimization method with direct inversion of the iterative subspace (RMM-DIIS) or blocked Davidson algorithms. These techniques are coupled with highly efficient Broyden and Pulay density mixing schemes to accelerate the self-consistency cycle. Further details on the methodology employed in VASP can be found in Ref. [**?**].

4.3.2 FDMNES simulation

FDMNES (Finite Difference Method Near Edge Structure) is a user-friendly cluster-based code which allows *ab initio* simulation of X-ray spectroscopies involving absorption or scattering processes at energies near the characteristic absorption edges. The code is particularly efficient in the vicinity of the edge, allowing for the calculation of spectra involving one-photon processes like X-ray absorption near-edge structure (XANES) and X-ray emission spectroscopy (XES), as well as polarization dependent processes such as X-ray magnetic circular dichroism (XMCD), X-ray magnetic linear dichroism (XMLD), X-ray natural linear dichroism (XNLD) and X-ray natural circular dichroism (XNCD) [**?**]. It can also calculate spectra involving two-photon processes such as resonant elastic X-ray scattering (REXS; also

called RXD or DANES) as well as non-resonant inelastic X-ray scattering (NRIXS or Raman X-ray scattering).

The code is most suitable for application to the calculation of K and L_1 edges, as well as the $L_{2,3}$ edges of heavy elements. It uses density functional theory (DFT) methods which is basically a ground-state theory. Therefore, for other edges that is sensitive to multi-electronic phenomena during the transition process, other theoretical approaches are more appropriate. Nevertheless, the code architecture is versatile and it is not rare to obtain satisfactory agreement with data even at these edges. Concerning the simulated system, no assumption on the potential is made and the code is fully relativistic. Consequently, virtually all systems can be calculated, including bulk crystals, liquids, small molecules and large metalloproteins [**?**]. From the point of view of chemical species, all elements ranging from hydrogen to the heavier actinides are allowed in the calculation.

FDMNES offers two operational modes for solving the electronic structure namely the full-potential finite difference method (FDM) and the full multiple scattering theory (FMS). FDM can predict precisely extra near-edge structures as it avoids muffin-tin approximation (applies for free shape potentials) while latter, FMS, gives less precise but faster calculations. The theoretical framework for FDMNES can be found from the works of Bunău, et al. in Ref. [**?**].

Chapter 5

Experimental setup

5.1 Sample preparation

Moderately-doped CaF_2 crystal with a nominal doping concentration of 0.01mol% was prepared by Bridgman method [**?**]. The crystal was cut parallel to the $\langle 111 \rangle$ direction and then polished into a circular disc with a diameter of 10 mm, a thickness of 1.0 mm, and an optical finish, as illustrated in Fig. 5.1.

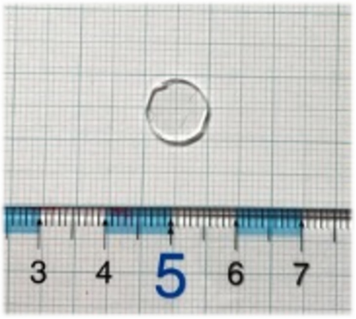

Figure 5.1: Photo of the 0.01mol% Ce-doped CaF_2 crystal.

On the other hand, moderately-doped $LiCaAlF_6$ and $LiSrAlF_6$ single crystals with a nominal doping concentration of 1.0 mol% were prepared by the Czochralski (CZ) method [**?**]. Ce^{3+}-doped $LiCaAlF_6$ crystal is described as having a cuboid shape with an optical finish, while the Ce^{3+}-doped $LiSrAlF_6$ crystal is shaped into a semicircular disc with an optical finish. The c-axis is perpendicular to one of the long planar sides of the Ce^{3+}-doped $LiCaAlF_6$ crystal, while for the Ce^{3+}-doped $LiSrAlF_6$ crystal,

it is perpendicular to the base of the crystal.

The subsequent stage involves characterizing the optical and local structural properties of the crystals. For the Ce-doped CaF_2 crystal, the optical properties will be examined through absorption, VUV fluorescence, excitation, fluorescence lifetime, and quantum yield measurements. The structural properties will be analyzed using XAS *K*-edge XANES and EXAFS techniques. Similarly, the Ce-doped $LiCaAlF_6$ and $LiSrAlF_6$ crystals will be examined for absorption and VUV fluorescence, with particular attention given to polarization dependence. To obtain a comprehensive understanding of the local structural properties of these crystallographically-related materials, a multi-spectroscopic approach will be employed. This approach will involve XAS *K*-edge XANES and EXAFS analyses, as well as XAS *L3*-edge XANES analyses. Furthermore, complementary simulations using DFT and FDMNES will be conducted. Collectively, these techniques are expected to provide the following specific information about the crystals' properties:

1. Oxidation state by XANES
2. Local structure by EXAFS with complementary DFT (optimized volume) and FDMNES simulation
3. Coordination number by EXAFS with complementary DFT (optimized volume) and FDMNES simulation
4. Optical transitions by optical spectroscopy (absorption, photoluminescence, etc.) with complementary DFT (total and partial DOS)

5.2 Optical spectroscopies

5.2.1 Transmission/Absorption spectroscopy

The absorption of the 0.01mol% Ce-doped CaF_2 crystal was measured in the vacuum UV (VUV) range of 120 to 300 nm. This measurement was carried out at room temperature in a vacuum chamber using a Bunkoukeiki KV-202 bench-top VUV spectrometer. The spectrometer utilizes a deuterium lamp as a light source and a nitrogen purge type monochromator,

allowing for a dynamic range of wavelengths from 120 nm (VUV) to 300 nm (UV). Irradiation is via the semi-double beam method and the transmitted light was detected using a photomultiplier tube with a salicylic acid soda window. Additional information on the Bunkoukeiki KV-202 bench-top VUV spectrometer can be found in Ref. [**?**].

On the other hand, the absorption of Ce-doped $LiCaAlF_6$ and $LiSrAlF_6$ crystals were measured using a polarized absorption setup. The same spectrometer was used but polarization of the incident beam can be adjusted parallel (π) or perpendicular (σ) to the crystal's c-axis by means of a polarizer.

5.2.2 Time-integrated photoluminescence spectroscopy

To investigate the 0.01mol% Ce-doped CaF_2 crystal, time-integrated photoluminescence (PL) spectroscopy was conducted at room temperature. The excitation source used was the 290-nm or 4.8-eV (frequency tripled, 3ω) output of a Spectra Physics Ti:sapphire femtosecond laser system. The incident laser beam, focused to a submillimeter size, was directed onto the crystal's surface. The PL spectrum was recorded using a StellarNet BLUE-Wave UVNb-50 miniature spectrometer. The experimental setup was configured such that the incident and emitted beams were at a 45° angle from the sample's surface, as illustrated in Fig. 5.2.

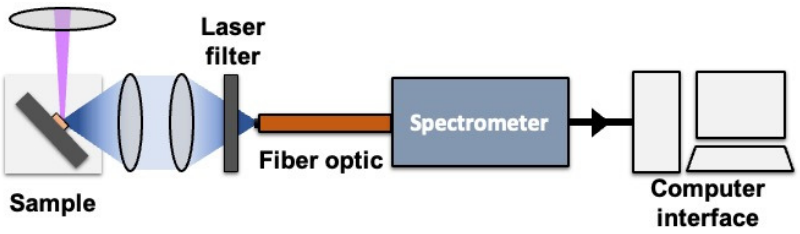

Figure 5.2: Schematic diagram of the experimental setup used for photoluminescence (PL) measurement of the 0.01mol% Ce-doped CaF_2 crystal.

The emission of Ce-doped $LiCaAlF_6$ and $LiSrAlF_6$ crystals were measured using a polarized setup. This time, the excitation source used was the fourth harmonic (266-nm wavelength) of a solid-state Nd:YAG pulsed laser system. A half-wavelength plate and a polarizer were utilized to set the

incident and emitted beam parallel (π) or perpendicular (σ) to the crystal's c-axis.

5.2.3 Time-resolved and time-integrated photoluminescence spectroscopy

Time-integrated photoluminescence (PL) and time-resolved photoluminescence (TRPL) spectroscopies were conducted at room temperature on a 0.01mol% Ce-doped CaF_2 crystal. The excitation source used for these experiments was the 290-nm or 4.8-eV (frequency tripled, 3ω) output of a Spectra Physics Ti:sapphire femtosecond laser system. The incident excitation was pulsed to allow observations of decay time between incoming pulses. The pulse duration used was 100 fs, much shorter than the expected decay times of Ce-doped CaF_2 crystals, and the repetition rate was 1 kHz. The setup for PL and TRPL measurements is shown in Figures 5.2 and 5.3, respectively. For the PL spectrum, a StellarNet BLUE-Wave UVNb-50 miniature spectrometer was employed. On the other hand, TRPL measurements were carried out using a Chromex 250is imaging spectrograph coupled with a Hamamatsu C1587 universal streak camera and a Hamamatsu C4742-95-10 NR high-resolution charge-coupled device (CCD) camera. In both cases, the setup was arranged so that the incident and emitted beams were at a 45° angle from the surface of the Ce-doped CaF_2 crystal.

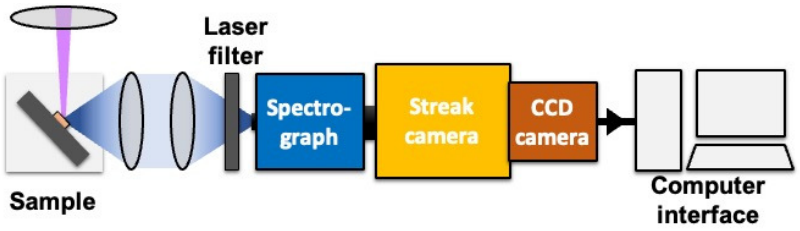

Figure 5.3: Schematic diagram for the time-resolved photoluminescence (TRPL) measurements of 0.01mol% Ce-doped CaF_2 crystal.

5.2.4 Quantum yield spectroscopy

PL excitation and quantum yield spectroscopies were performed on the Ce-doped CaF_2 crystal using a Quantaurus-QY Plus C13534-11 UV-NIR

absolute PL quantum yield spectrometer. This spectrometer has a detection range from 300 nm to 950 nm and a resolution of less than 2 nm. It is specifically designed to measure the instantaneous absolute value of emission quantum yield using the PL method. Further information about the spectrometer can be found in Ref. [**?**].

5.3 X-ray absorption spectroscopy

5.3.1 X-ray Absorption Spectroscopy at the Ce *K*-edge

Ce *K*-edge XAS measurements were performed at the NW10A beamline of the Photon Factory Advanced Ring (PF-AR) at the High Energy Accelerator Research Organization (KEK). A water-cooled Si(311) double crystal was utilized as the monochromator. Cerium (III) fluoride (CeF_3) and cerium (IV) oxide (CeO_2) were used as reference samples for the Ce^{3+} and Ce^{4+} oxidation states, respectively. These reference samples were prepared by diluting the respective powders with boron nitride (BN) and then pressing them into pellets with a diameter of 10 mm and a thickness of approximately 1.0 mm. The CeF_3 and CeO_2 spectra were obtained at room temperature in transmission mode using ionization chambers. The schematic diagram of the Ce *K*-edge XAS setup for the measurement of the 0.01mol% Ce-doped CaF_2 crystal is presented in Figure 5.4. In this setup, the crystal was positioned at a 45° angle from the source and the detector. The fluorescence spectrum was recorded at room temperature using a Ge pixel array detector (Canberra), while the CeO_2 reference spectrum was simultaneously measured in transmission mode for X-ray beam calibration. For all the samples, the spectra were merged from at least three repetitions and were analyzed using the Larch program [**?**].

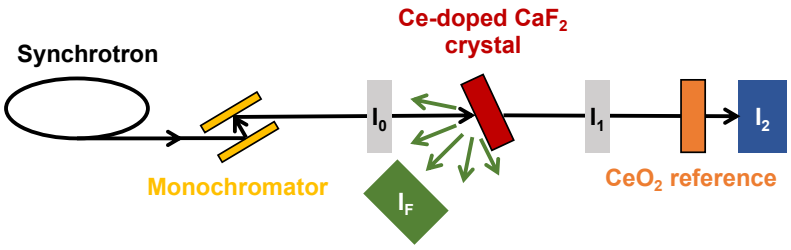

Figure 5.4: Schematic diagram of the XAS setup for the 0.01mol% Ce-doped CaF_2 crystal.

For the 1.0 mol% Ce-doped $LiCaAlF_6$ and 1.0 mol% Ce-doped $LiSrAlF_6$ crystals, the aforementioned setup was configured for polarization experiments. The crystal was mounted such that its c-axis was parallel or perpendicular to the incident X-ray's polarization. In addition, polarization experiments were also performed at the Ce L_3-edge at the BL9A beamline of the Photon Factory (PF) in KEK.

DFT methods were then employed to complement the results of the XAS experiments. Particularly, the optimized volume, charge density difference, and the total and partial density of states (DOS) of $2 \times 2 \times 2$ $LiCaAlF_6$ and $LiSrAlF_6$ supercells, containing one Ce atom, were calculated using the Vienna ab initio simulation package (VASP) software. Projector augmented wave (PAW) pseudopotentials and the generalized gradient approximation within the Perdew-Burke-Ernzerhof (GGA-PBE) exchange-correlation functional were used for the calculations.

Finally, the Ce L_3-edge spectra were simulated using the finite difference method near edge structure (FDMNES) program. The optimized volume from the DFT calculations were used as input CIF files. The atomic configurations of the Ce ion were set manually to emulate the $4\,f^1 5\,d^*$ Ce^{3+} and $4\,f^0 5\,d^*$ Ce^{4+} excited states, as well as the ligand charge transfer, $L4\,f^1 5\,d^*$ Ce^{3+} excited state. Here, "textitL" indicates that an electron from the ligand is transferred to the Ce 4f orbital and "d*" denotes an excited electron in the d orbital. The cluster radius was increased from 3 to 4 Å. Only dipole interactions were considered, and each spectrum was convoluted with a Gaussian function with a width of 1.0. The energy and the intensity of each simulated spectrum were adjusted as well.

Chapter 6

Results

6.1 Optical properties of 0.01mol% Ce-doped CaF_2 single crystal

The VUV absorption spectrum of a 0.01mol% Ce-doped CaF_2 single crystal at room temperature is shown in Figure 6.1. The spectrum displays five distinct absorption bands, centered around 185, 195, 204, 244, and 304 nm, along with the CaF_2 host edge at 123 nm. The shallow absorption depths of bands are typical for oxygen-free, low concentration Ce-doped CaF_2 crystals at room temperature. The bands at 185, 195, 204, and 304 nm are attributed to the 4f→5d transitions of a single-ion C_{4v} F_i' (100) Ce^{3+} center, while the remaining band at 244 nm is associated with the 4f→5d transitions of a cluster-ion C_{3v} F_i' (111) Ce^{3+} center [**? ? ? ? ?**]. Hence, the bands in Fig. 6.1 are labeled accordingly.

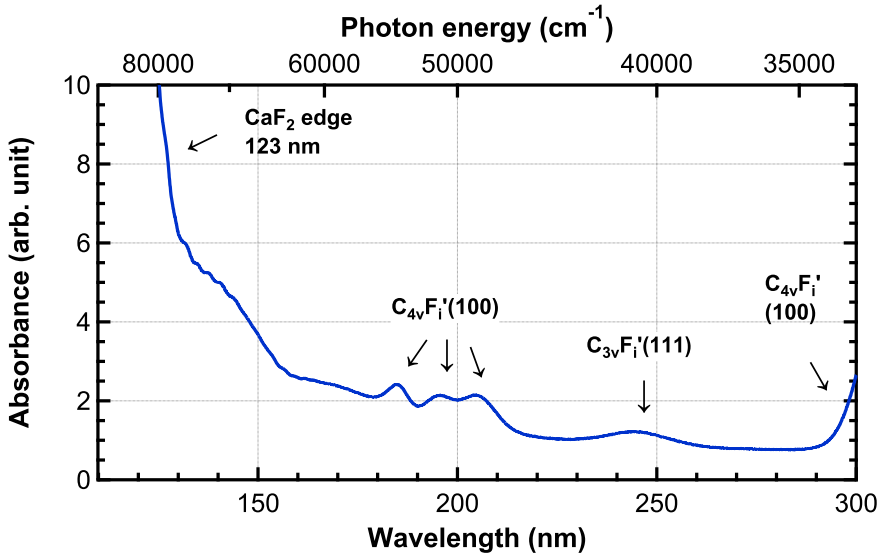

Figure 6.1: VUV absorption spectrum of 0.01mol% Ce-doped CaF_2 single crystal at room temperature.

The UV PL emission spectrum of the 0.01mol% Ce-doped CaF_2 single crystal at room temperature is displayed in Fig. 6.2. Once again, the 290-nm wavelength of the Ti:sapphire laser was used as the excitation source. The crystal exhibits a double-peak emission band with a separation distance of approximately 0.2 eV (1800 cm^{-1}). These emission bands are attributed to the interconfigurational 5d→4f ($^2F_{5/2}$) and 5d→4f ($^2F_{7/2}$) transitions of the single-ion Ce^{3+} center, C_{4v} F_i' (100) [**? ? ?**]. It should be noted that to excite the C_{3v} F_i' (111) center, the excitation wavelength needs to fall within the shorter-wavelength range of 250 to 270 nm, as will be demonstrated in the subsequent PL excitation spectra. Therefore, in this particular spectrum, the emission associated with the cluster-ion Ce^{3+} center, C_{3v} F_i' (111), is not discussed because the 290-nm excitation wavelength is not enough to excite any C_{3v} F_i' (111) center.

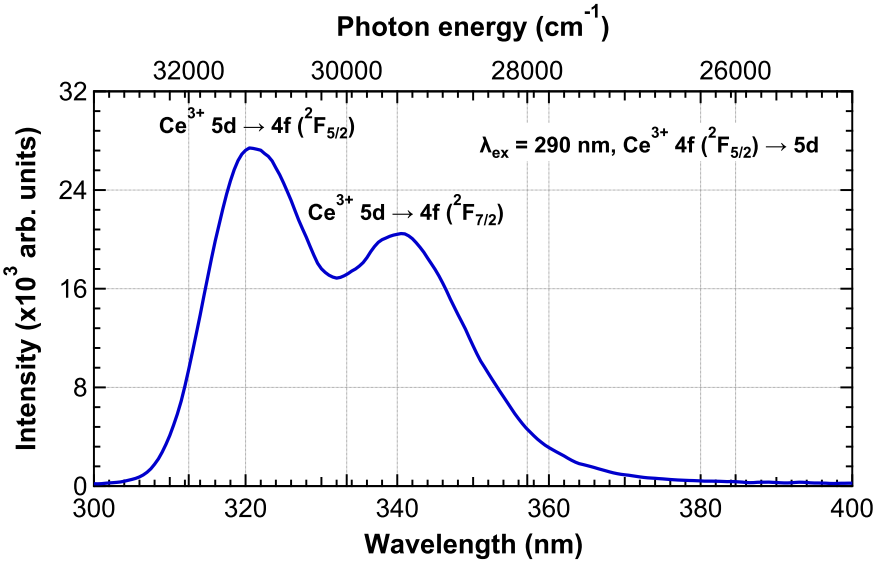

Figure 6.2: UV PL spectrum of 0.01mol% Ce-doped CaF_2 single crystal under 290-nm Ti:sapphire laser excitation at room temperature.

The UV PL emission decay of the 0.01mol% Ce-doped CaF_2 single crystal at room temperature under 290-nm Ti:sapphire laser excitation is shown in Fig. 6.3. In this time-resolved streak image, the double emission bands of the Ce-doped CaF_2 crystal, centered at 320 and 340 nm, are clearly distinguishable and can be analyzed separately. The individual decay profiles of the 320 and 340-nm emission bands of the Ce-doped CaF_2 crystal are shown in Fig. 6.4. The temporal resolution for this setup, using the fast scanning mode, is 3 ns. The 320-nm emission displays a single exponential decay with a decay constant of 40.3 ± 0.5 ns (Fig. 6.4a). Similarly, the 340-nm emission also exhibits a single exponential decay, but with a slightly lower decay constant of 38.4 ± 0.4 ns (Fig. 6.4b). These decay times are comparable to those reported for 1.0 to 10mol% Ce-doped CaF_2 single crystals (44.1 to 51.6 ns) [**?** **?**]. However, it is important to note that our results were obtained using a different setup and the previously mentioned values were derived from averages of two decay profiles.

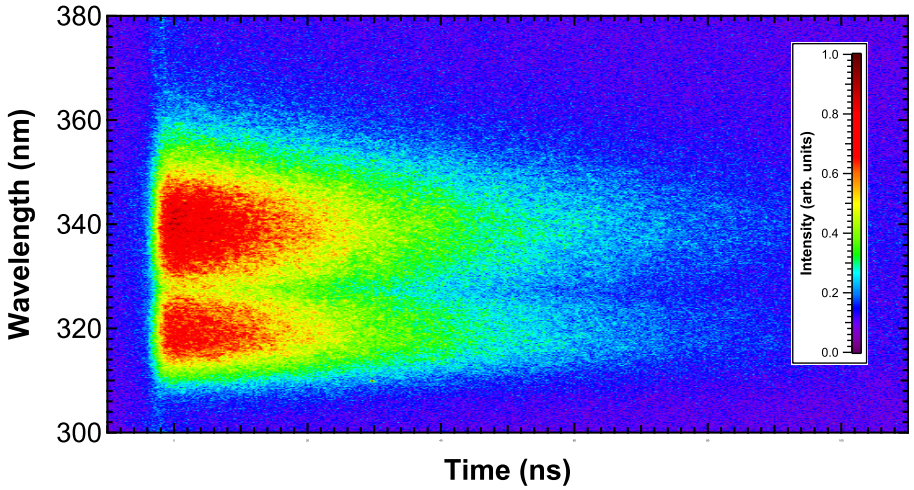

Figure 6.3: UV PL emission decay of 0.01mol% Ce-doped CaF_2 single crystal under 290-nm Ti:sapphire laser excitation at room temperature.

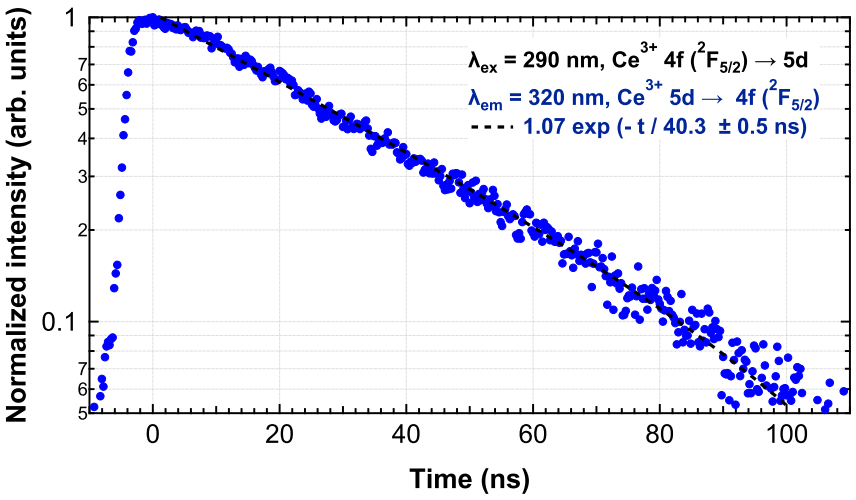

(a)

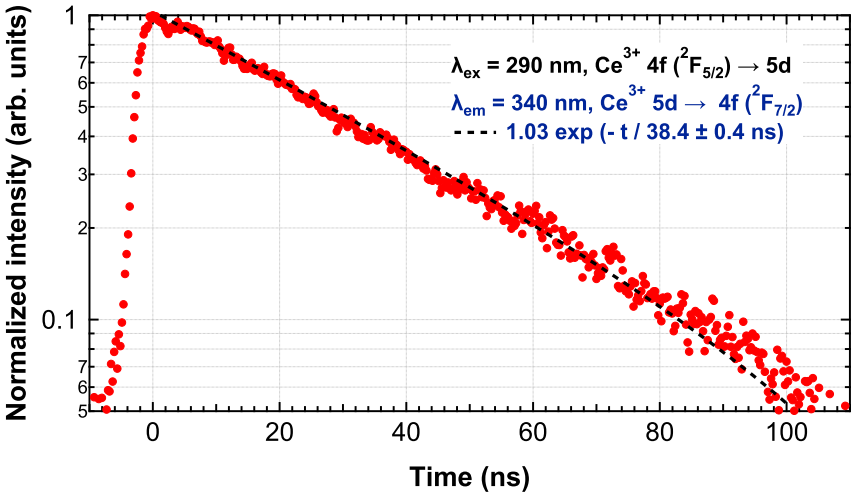

(b)

Figure 6.4: Decay profile of the (a) 320 and (b) 340-nm emissions of 0.01mol% Ce-doped CaF_2 single crystal under 290-nm Ti:sapphire laser excitation at room temperature. The fitted single exponential functions are represented as dotted lines.

The PL excitation spectra of the 0.01mol% Ce-doped CaF_2 single crystal are presented in Fig. 6.5. It can be observed that both excitation curves, monitored around 320 and 340 nm, exhibit similar trends within the wavelength range of 250 to 300 nm. These trends indicate that in order to generate the 320 and 340 nm emission bands, excitation should be performed within the range of 250 to 270 nm and 285 to 300 nm, respectively. The former corresponds to the absorption band associated with the

cluster-ion Ce^{3+} center, C_{3v} F_i' (111), while the latter is for the single-ion Ce^{3+} center, C_{4v} F_i' (100). The quantum yield of the 0.01mol% Ce-doped CaF_2 single crystal, monitored within the emission range of 300 to 400 nm, is also depicted as a function of excitation wavelength in Fig. 6.6. The quantum yield follows a similar trend as observed in the PL excitation spectra in Fig. 6.5. Specifically, the quantum yield decreases from 33.3% to zero as the excitation wavelength varies from 250 to 270 nm, remains at zero at 285 nm, and then exponentially increases to a maximum of 66.9% at 300 nm. This result indicates that both excitation regions contribute to the radiative transitions (fluorescence) in the 320 and 340 nm emission regions. However, the presence of a quantum yield gap of approximately 37% between the excitation regions of 250 to 270 nm and 285 to 300 nm suggests that non-radiative transitions occur between the C_{3v} F_i' (111) and C_{4v} F_i' (100) centers [**? ?**]. Consequently, exciting the Ce^{3+} center, C_{4v} F_i' (100) centers is more efficient in generating UV emission from the Ce-doped CaF_2 crystal.

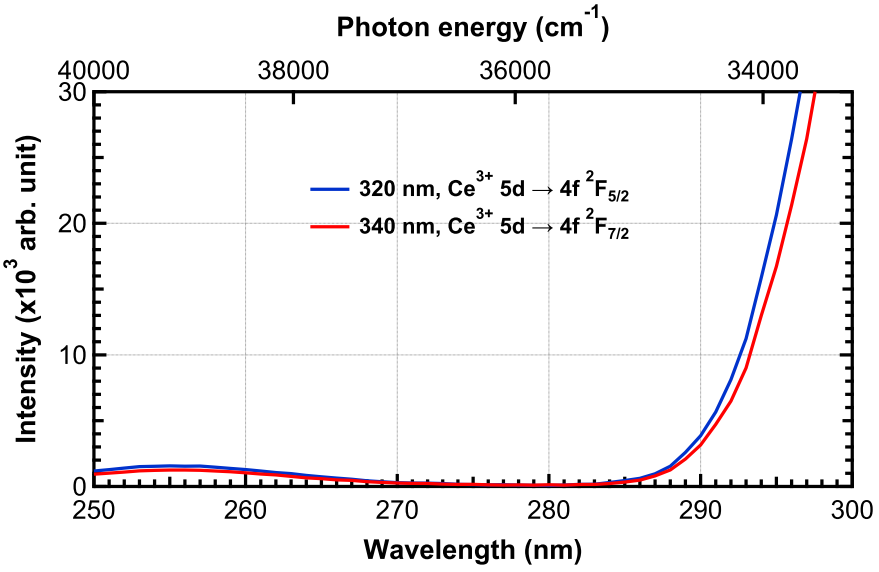

Figure 6.5: PL excitation spectra of 0.01mol% Ce-doped CaF_2 single crystal monitored around 320 and 340 nm at room temperature.

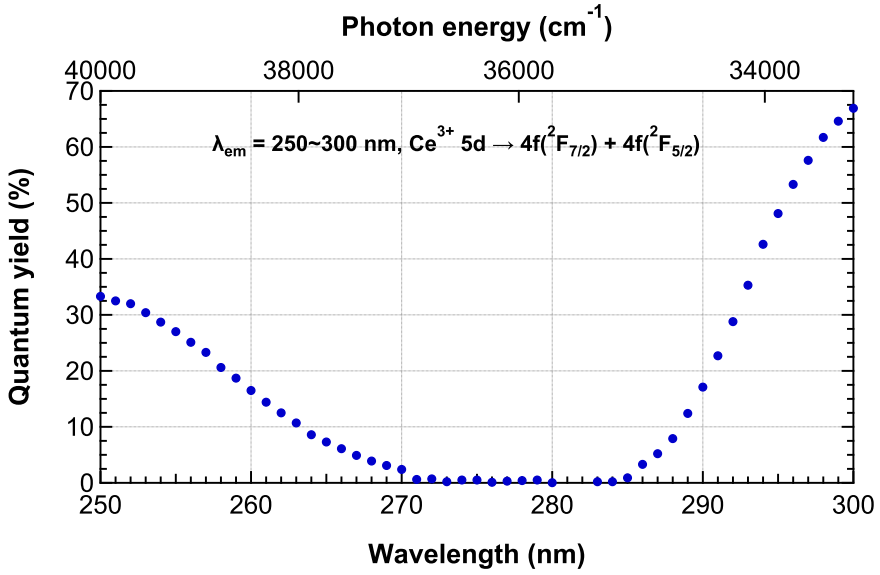

Figure 6.6: Quantum yield of 0.01mol% Ce-doped CaF_2 single crystal, monitored within the 308 to 386-nm emission range at room temperature under different excitation wavelengths.

6.2 Optical Properties of 1.0mol% Ce-doped $LiCaAlF_6$ and 1.0mol% Ce-doped $LiSrAlF_6$ crystals

The absorption spectra of Ce-doped $LiCaAlF_6$ and $LiSrAlF_6$ crystals show weak polarization dependence, with peaks at 266 and 270 nm for LiCaAlF6 and at 264 and 269 nm for $LiSrAlF_6$. The emission spectra exhibit double-peak bands, with peaks at 290 and 310 nm for $LiCaAlF_6$ and at 292 and 313 nm for $LiSrAlF_6$. A significant blue shift in the 292-nm emission band and a doubling of intensity are observed for $LiSrAlF_6$ when the emitted beam is polarized parallel to the crystal's c-axis, while $LiCaAlF_6$ experiences a smaller blue shift and less pronounced increase in intensity.

6.3 Ce ion's local environment in 0.01mol% Ce-doped CaF_2 single crystal

The Ce K-edge XANES spectrum of the 0.01 mol% Ce-doped CaF_2 single crystal at room temperature is presented in Fig. 6.7. Also included are the CeF_3 (red line) and CeO_2 (blue line) reference spectra for the Ce^{3+} and Ce^{4+} oxidation states, respectively. The absorption edge of the Ce-doped CaF_2 single crystal coincides well with that of the CeF_3 reference, confirming that the Ce ion dopant retains its original oxidation state of 3+. The XANES spectra of the Ce-doped CaF_2 crystal and the reference samples exhibit a few damped oscillations without distinct features that differentiate the samples, unlike those seen in other transition metals with low-energy absorption edges. In this regard, the XANES features of the Ce-doped CaF_2 crystal appear similar to those of the CeF_3 reference. However, the following K-edge EXAFS analysis will demonstrate that the coordination environments are different.

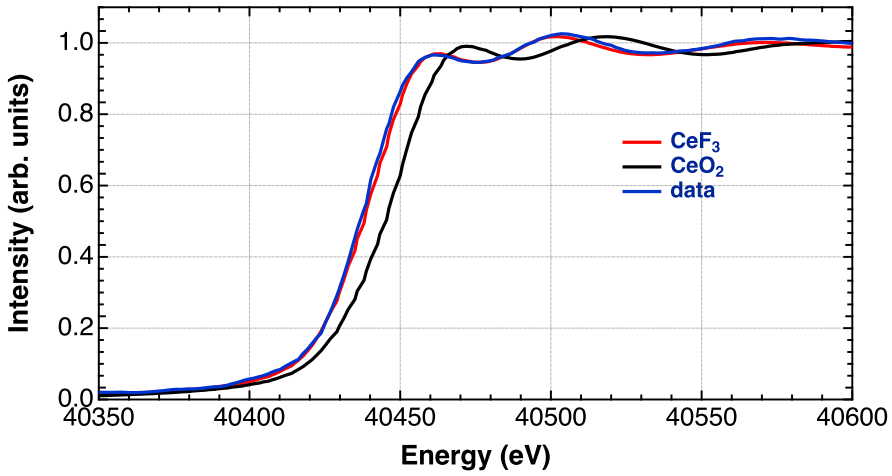

Figure 6.7: Ce K-edge XANES spectrum of 0.01mol% Ce-doped CaF_2 single crystal (black line) at room temperature. The CeF_3 (red line) and CeO_2 (blue line) reference spectra for the Ce^{3+} and Ce^{4+} oxidation states, respectively, are also shown.

To validate previous interpretations regarding the presence of multiple Ce^{3+} centers with reduced site symmetries and to confirm whether the crystal shares the same local structure as the CeF_3 reference, we conducted

EXAFS analysis on the 0.01 mol% Ce^{3+}-doped CaF_2 crystal. Figs. 6.8 and 6.9 exhibit the k-space and R-space EXAFS spectra of the 0.01mol% Ce^{3+}-doped CaF_2 single crystal, respectively. The k range is set from 3.0 to 12.0 $\mathring{A}^{-1}$, while the R range extends from 1.00 to 2.36 Å. The first shell fitting, indicated by the red dashed line, yields an r-factor of 0.0138. This corresponds to a coordination number (CN) of 7.0 ± 0.7 and a Ce-F bond length of 2.396 ± 0.008 Å. These values align with the CN (8) and Ca-F bond length (2.389) of the undoped CaF_2 crystal, respectively. However, these values fall short of the CN (9) and average Ce-F bond length (2.486) of CeF_3. Consequently, this result directly confirms that the Ce^{3+} ion substitutes the Ca^{2+} ion site in CaF_2. Due to the low signal-to-noise ratio, we cannot extend the analysis to the higher k region. Therefore, it is not possible to determine the location of the interstitial F^- ions. Nevertheless, our findings establish that the local structure remains unchanged when the trivalent Ce^{3+} ion replaces the divalent Ca^{2+} ion. Furthermore, there is no significant distortion induced in the local environment surrounding the Ce^{3+} ion in CaF_2, suggesting the presence of a distant charge compensator. This is plausible because the F^- ions are not tightly bound to the empty cube of F^- ions closest to the Ce^{3+} ion [**?**]. Our analysis cannot discriminate traces of other potential Ce^{3+} centers, i.e., with different symmetry, in both the XANES and EXAFS spectra. However, on average, the Ce^{3+} ion in the moderately doped (0.01mol%) CaF_2 experiences an undisturbed 8-coordinated cubic (O_h) crystal field.

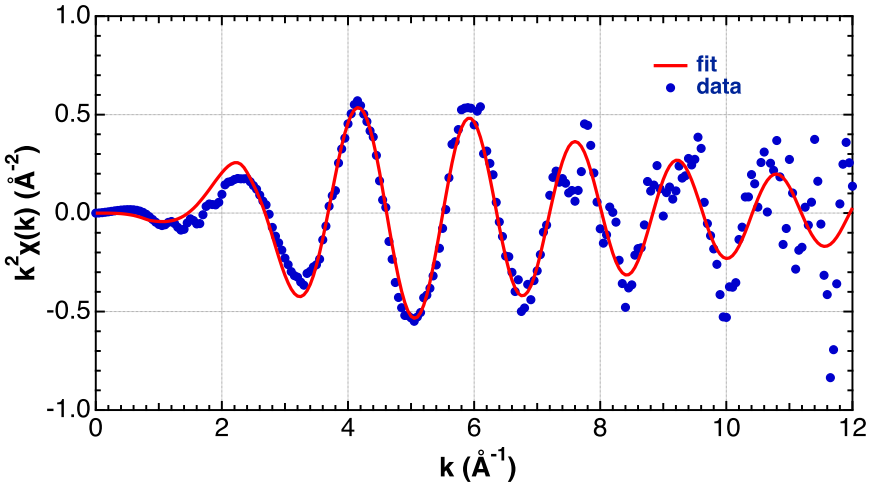

Figure 6.8: Ce K-edge EXAFS spectra in k-space of 0.01mol% Ce^{3+}-doped CaF_2 single crystal at room temperature. The measured data for the Ce^{3+}-doped CaF_2 crystal is represented by solid black dots, while the first shell fitting curve of its Fourier transform, using the CeF_3 FEFF input file, is denoted by a red solid line.

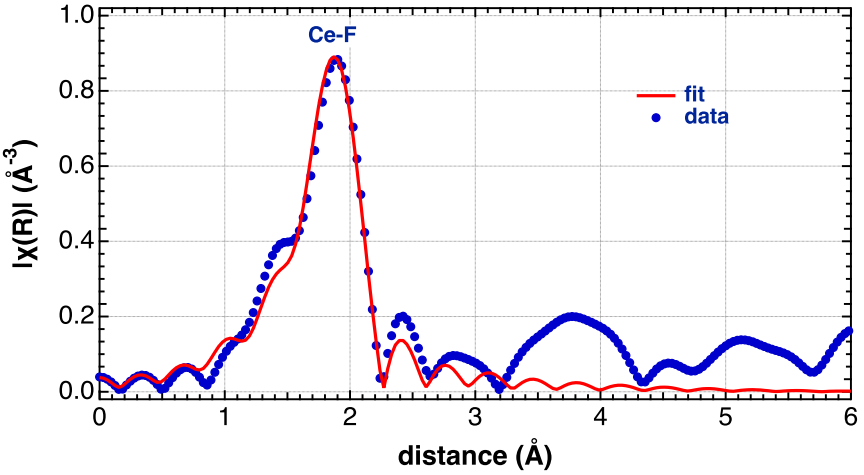

Figure 6.9: Ce K-edge EXAFS spectra in R-space of 0.01mol% Ce^{3+}-doped CaF_2 single crystal at room temperature. The measured Ce^{3+}-doped CaF_2 data is also represented as solid black dots, while the 1st shell fitting curve of its Fourier transform using CeF_3 FEFF input file is denoted by a red solid line.

6.4 Ce ion's local environment in 1.0mol% Ce-doped $LiCaAlF_6$ and 1.0mol% Ce-doped $LiSrAlF_6$ single crystals

The oxidation states and local environments of Ce in $LiCaAlF_6$ and $LiSrAlF_6$ crystals were investigated using XANES and EXAFS analysis. The Ce L_3-edge XANES spectra showed no pronounced polarization dependence, and displayed prominent peaks coincident with the CeF_3 reference, indicating that both crystals are dominated by trivalent Ce ions. However, both crystals also exhibited distinct peaks C and D, which are characteristic peaks of CeO_2 (Ce^{4+}) reference. These peaks were more pronounced in the Ce-doped $LiSrAlF_6$ crystal. Contrary, the Ce K-edge XANES spectra indicated the presence of solely trivalent Ce ions in Ce-doped $LiCaAlF_6$, while the analysis for Ce-doped $LiSrAlF_6$ was inconclusive due to low signal-to-noise ratio. EXAFS analysis on Ce-doped $LiCaAlF_6$ revealed that the Ce^{3+} ions substitute at the Ca ion site and maintain a 6-coordinated octahedral environment. The crystal's optimized volumes from DFT calculations supported this result and indicated a slight distortion in the CeF_6 octahedron. The charge density difference, and the total and partial density of states (DOS) revealed hybridization of the Ce ion's 4f and 5d states with its neighbor Al^{3+} ion's 3s and 3p states and F^- ion's 2p states due to their covalent interactions. Charge transfers between these ions are therefore possible. The main feature, peaks B, in the Ce L_3-edge XANES spectra was successfully simulated using the FDMNES program and optimized volumes from DFT as input files. Peak D was reproduced by taking into account the contribution of the Al^{3+} ion, while peak C was simulated by inducing a charge transfer from the ligand F^- ion to the 4f orbital of the Ce ion.

Chapter 7

Local structures and optical properties of Ce-doped fluoride crystals

7.1 Ce^{3+} ion in CaF_2 crystal

The Ce ion in a moderately-doped (0.01mol%) CaF_2 crystal is expected to replace the Ca^{2+} ion due to their similar ionic sizes. Through XAS K-edge XANES and EXAFS analyses, we confirmed that the Ce ion remains in the 3+ oxidation state and indeed substitutes at the Ca^{2+} site. The presence of multiple VUV absorption bands from 180 to 300 nm and two UV emission peaks around 320 and 340 nm indicate the presence of a dominant single-ion Ce^{3+} center with a cubic (O_h) symmetry rather than a tetragonal (C_{4v}) symmetry. This suggests that charge compensation is remote to the Ce^{3+} ion. However, our analysis could not differentiate between different symmetries of the Ce^{3+} ion due to the limitations of our EXAFS analysis at the K-edge, which provides only an average result. Therefore, we cannot confirm the existence of a cluster-ion Ce^{3+} center, despite the presence of its signature 240-nm absorption band in the optical spectroscopic data.

The presence of a cubic (O_h) Ce^{3+} center has been reported in annealed CaF_2 and SrF_2 crystals, as well as in moderately-doped (<0.01mol%) CaF_2 crystals co-doped with Na [**?** **?** **?**]. In annealed and moderately-doped CaF_2 and SrF_2 crystals, fast cooling prevents F^- interstitial ions from

diffusing towards the Ce^{3+} ion. In (Ce, Na) co-doped CaF_2 crystals, the Na^+ ion maintains the cubic symmetry of the Ce^{3+} center by keeping a large separation distance from the Ce^{3+} ion. The 5d splitting scheme of the cubic and tetragonal crystal fields is defined by a low-lying e_g and a high-lying t_{2g} levels [**?** **?** **?**]. In the cubic crystal field, the t_{2g} level is further split into three bands by spin-orbit coupling with an equal spacing of approximately 0.3 eV. The absorption spectrum of the moderately-doped (0.01mol%) CaF_2 crystal agrees more with the features of the cubic crystal field than with the tetragonal crystal field, as observed in Fig. 6.1. The corresponding crystal field splitting of the Ce^{3+} ion in cubic (O_h) symmetry, with an average Ce-F bond length of 2.3956 Å, is illustrated in Fig. 7.1.

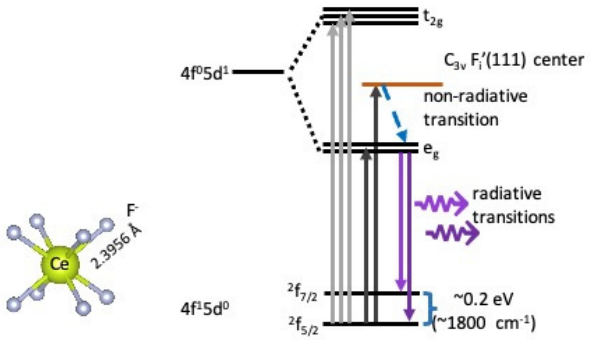

(a) (b)

Figure 7.1: Local structure of Ce^{3+} ion in 0.01mol% Ce-doped CaF_2 and the corresponding crystal field splitting of its 4f and 5d levels.

If the F^- interstitial ion moves closer to the Ce^{3+} ion, as in a tetragonal crystal field, the band-to-band distance between e_g and t_{2g} is expected to increase. The splitting of both e_g and t2g levels into $(x^2 - y^2)$ and $(2z^2 - x^2 - y^2)$, as well as into t_{2g} to (xy) and (yz and zx), respectively, will become more pronounced. However, the emission decay time will remain the same [**?** **?**]. Due to the significant spatial separation between the orbitals of the interstitial F^- ion and the lowest excited orbital ($d_{x^2-y^2}$) of the Ce center, the wavefunctions of the lowest excited states in both cubic and tetragonal centers are the same [**?**]. Therefore, their probabilities of transitioning to the ground state are the same. This explains why the decay time (Fig. 6.3) observed in the moderately-doped (0.01mol%) CaF_2 crystal with an undisturbed 8-coordinated cubic (O_h) Ce^{3+} center is comparable to

those reported for Ce-doped CaF_2 single crystals with concentrations ranging from 1.0 to 10mol%. Lastly, our PL excitation (Fig. 6.5) and quantum yield (Fig. 6.6) spectra demonstrate that the emission pathways leading to the 320 and 340 nm emission bands differ for cubic and trigonal Ce^{3+} centers. The trigonal Ce^{3+} center undergoes an additional non-radiative transition before the radiative transition to the 4f levels, indicating that excitation via the Ce^{3+} cubic center is more efficient.

7.2 Ce^{3+} ion in $LiCaAlF_6$ and $LiSrAlF_6$ crystals

Our XAS K-edge XANES and EXAFS analyses confirmed that Ce^{3+} ions maintain their oxidation state and substitute for Ca^{2+} ions in $LiCaAlF_6$ crystals. The substitution preserves the 6-coordinated octahedral environment of Ca^{2+}, albeit with slight stretching observed in the Ce-F bond lengths. Unfortunately, the poor signal-to-noise ratio prevents a similar analysis for the Ce-doped $LiSrAlF_6$ crystal. However, the XAS L_3-edge XANES spectra of both crystals show coinciding whiteline peaks, indicating dominant Ce^{3+} centers and potentially similar local environments. DFT calculations and FDMNES simulations support the presence of a singular Ce3+ center with a comparable trigonal environment in both crystals.

Based on DFT calculations, the positions of the 4f and 5d levels of the Ce^{3+} ion in Ce-doped $LiCaAlF_6$ and $LiSrAlF_6$ crystals were found to be in close proximity to the conduction band, with a slight shift towards the valence band in $LiSrAlF_6$. These levels overlap with those of F^- and Al^{3+} ions in the crystal host, facilitating the transfer of electrons between them. Peaks C and D in the spectra provide evidence of these charge transfers. This can also explain the anisotropy in the absorption and emission bands, as well as the excited state absorption (ESA). The stronger covalent interaction in Ce-doped $LiSrAlF_6$ compared to Ce-doped $LiCaAlF_6$ results in more pronounced optical anisotropy and ESA. In Ce-doped $LiCaAlF_6$ and $LiSrAlF_6$ crystals, the extent of the overlap between the electronic states of Ce ion (4f and 5d) and its neighboring F^- and Al^{3+} ions is attributed to charge transfer effects (covalent interaction) rather

than distortions in the F-M-F^{i} and F-M-F^{ii} angles.

7.3 How to designing a scintillator and UV laser crystal

The principle of the laser was first known in 1917 when Einstein described the theory of stimulated emission. In 1958, Schalow and Townes established the conditions for laser action at optical frequencies. They, along with Prokhorov and other engineers, worked towards creating MASER (Microwave Amplification by the Stimulated Emission of Radiation) [**?**], which amplified microwaves for use in communication systems. Then, in 1960, Maiman demonstrated laser action using ruby as the lasing medium [**?**]. Other significant advancements followed, such as the operation of trivalent uranium and divalent samarium in CaF_2 [**?**], and the demonstration of laser action in Nd^{3+}-doped glass in 1961 [**?**]. The first continuously operating crystal laser was reported in the same year by Johnson and Nassau using Nd^{3+}:$CaWO_4$ [**?**]. Since then, laser action has been achieved with various materials, including trivalent lanthanides, divalent lanthanides, transition metals, and the actinide ion U^{3+}, embedded in different host materials. Optically pumped laser action has been demonstrated in numerous ion-host crystal combinations, covering a spectral range from ultraviolet to mid-infrared. The Nd^{3+}:YAG combination, explored by Geusic *et al* [**?**], has become a reference for solid-state laser materials due to its low thresholds for continuous wave (CW) operation at room temperature.

The general scheme of a solid-state laser is depicted in Fig. 7.2. It consists of an active medium with selectively populated energy levels, a pump to excite the active medium and create population inversion, and a resonant electromagnetic cavity that contains the active medium and provides feedback to amplify and maintain the coherence of the emitted light.

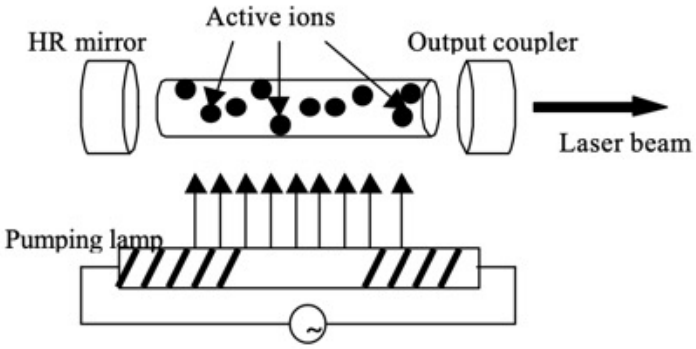

Figure 7.2: General scheme of a solid-state laser.

The energy-level structure of laser materials plays a crucial role in achieving the population inversion required for laser action. The main features can be understood through two commonly used idealizations: the three-level and four-level systems, as illustrated in Fig. 7.3. In optically pumped three-level lasers like ruby, the process begins with all ions in the lowest level (level 1). Excitation and absorption mechanisms then populate level 3, which is typically composed of multiple bands to enable broad-spectrum optical pumping. The majority of excited ions undergo fast radiationless transitions to the intermediate level 2, while some energy is lost and transferred to the lattice. The electron eventually returns to the ground level by emitting a photon. When the pumping intensity is below the laser threshold, atoms in level 2 primarily return to the ground state through spontaneous emission. After the pump radiation ceases, level 2 is depopulated through fluorescence, which varies in rate depending on the material. Ordinary fluorescence acts as a drain on the population of level 2. However, when the pump intensity exceeds the laser threshold, the decay from the fluorescent level includes both stimulated and spontaneous radiation, with the stimulated radiation producing the laser output beam.

Normally, it is necessary for the rate of radiationless transfer from the highest level to the level where laser action begins to be fast compared to other spontaneous transition rates in a three-level laser. Therefore, the lifetime of level 2 should be significantly longer than the relaxation time of the 3→2 transition. Additionally, a three-level laser requires an extremely high-intensity source to achieve a highly populated level 2. To overcome this limitation, the four-level system is utilized in lasers such as Nd:YAG,

Ce:$LiCaAlF_6$, and Ce:$LiSrAlF_6$. In this system, the pump transition extends from the ground state (level 0) to the absorption level 3, similar to the three-level system. However, in the four-level system, the excited ions quickly proceed to level 2. The laser transition then occurs to a fourth, terminal level 1 located above the ground state. From here, the atom undergoes a rapid non-radiative transition back to the ground level. In a true four-level system, the material must have a relaxation time between the terminal laser level and the ground level that is fast compared to the fluorescent lifetime. Additionally, the terminal laser level should be significantly higher than the ground state to minimize its thermal population. If the energy gap between the lower laser level and the ground state is small, the material can be cooled to function as a four-level laser. In a four-level system, an inversion of the 2→1 transition can even occur at low pump power, eliminating the need for high pump rates required to maintain equilibrium population in the three-level system mentioned earlier. In the most favorable scenario, the relaxation times of the 3→2 and 1→0 transitions in the four-level system are short compared to the spontaneous emission lifetime of the laser transition.

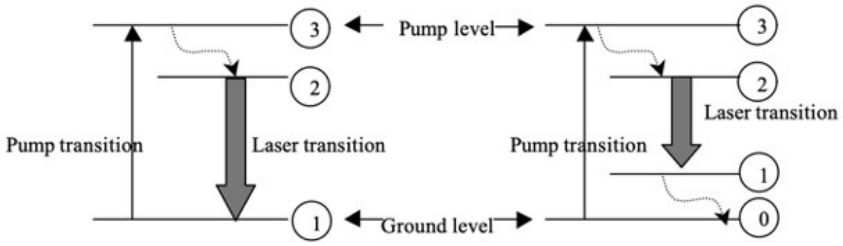

Figure 7.3: Simplified energy level diagram of a three-level (left) and a four-level (right) laser.

Generally, the decay or lifetime of photoluminescence (PL), fluorescence, and phosphorescence is determined by the total relaxation rate constant (W_{tot}) of the excited state following excitation. W_{tot} can be calculated as the sum of the spontaneous emission rate constant (A) and the non-radiative rate constant (W_{NR}), which is also equivalent to the inverse of the observed photoluminescence lifetime (τ).

$$W_{tot} = A + W_{NR} = \frac{1}{\tau} \tag{7.1}$$

Assuming that non-radiative rate constant is small enough compared

with the spontaneous emission rate constant, the luminescence lifetime is determined only by the radiative rate of the specific excited state for the individual luminescence ions. The luminescence decay can thus be expressed as

$$I(t) = I_0 \exp -At = I_0 \exp -\frac{t}{\tau} \tag{7.2}$$

where I_0 is the initial PL intensity at t=0, τ is the luminescence lifetime. If the luminescence ions and the type of transition are known, then the luminescence lifetime can be roughly determined.

Laser and scintillator materials can therefore be designed based on the electronic structure of the laser crystal. In Chapter 1, there are four models, namely the redshift model, centroid shift model, charge transfer model, and *charge transfer model*, which are extrapolated from reported spectroscopic data. These models can be used to estimate how deep the 4f and 5d levels of the Ce ion or other lanthanide ions can be in a given host crystal. For instance, Ueda *et al* have utilized the chemical shift model, along with the correction of the nephelauxetic effect, to construct the vacuum referred binding energy (VRBE) diagram for various Ln^{2+} and Ln^{3+} ions in garnet YAG host crystal [**?** **?** **?**]. They have also employed experimental charge transfer absorption energy and *ab-initio* calculations, in conjunction with the VRBE of Ln ions, to predict the VRBE diagram for transition metal (TM) ions [**?**]. By doing so, they were able to identify luminescent centers compatible with the YAG host crystal. Their results confirmed that Ce^{3+} ion is a suitable candidate since its lowest $5d_1$ level is located below the bottom of CB with an appropriate energy gap (Fig. 1.6) and the 4f-$5d_1$ absorption is located in the blue region due to strong crystal field (Fig. 1.6) which is a result of a strong crystal field (Fig. 1.6). Hence, thermal-stimulated photoionization through blue light excitation via the 4f-$5d_1$ absorption is feasible for Ce^{3+}-doped YAG. Conversely, they were able to rule out Eu^{2+} and Yb^{2+} ions since their $5d_1$ levels, located within the conduction band, would lead to significant auto-ionization quenching.

In the YAG host crystal, both Ce^{3+} and Pr^{3+} ions act as hole-trapping centers. In order to be used as a blue light chargeable persistent phosphor, these ions must keep a hole before the recombination phase. To achieve this,

electron traps can be intentionally introduced in Ce and Pr-doped YAG through co-doping, while also satisfying the condition $E_{h\_trap} > E_{e\_trap}$. In this regard, Ueda *et al* have also identified suitable co-dopant candidates for the Ce^{3+} ion in YAG, including Sm^{3+}, Eu^{2+},Yb^{3+}, Sc^{3+}, Ti^{3+}, V^{3+}, and Cr^{3+} ions. These co-dopants have their respective divalent ions located below the bottom of the conduction band. Fig. 7.4 shows the thermoluminescence (TL) glow curves, which provide information about the depth trap of Ce^{3+}-doped YAG with different co-dopant ions [**?**]. By changing the co-dopant ions, the TL glow peak temperature clearly varies, demonstrating the formation of different electron traps by these co-dopants. Although there is a slight energy difference between the trap depth estimated by the VRBE diagram and the TL glow curves, it is sufficient for screening candidates for electron traps.

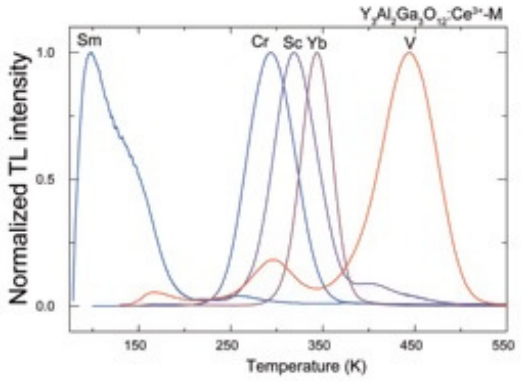

Figure 7.4: Thermoluminescence glow curves of $Y_3Al_2Ga_3O_{12}$:Ce^{3+} with different electron traps [**?**].

Laser and scintillator materials can also be designed based on the local crystalline structure of the material. In previous works, doping was carried out through trial and error. The doping concentration was maintained at low levels, and the size and valence of the additive ion were matched to those of the host ion it replaces so as not to disturb the crystal lattice. However, these studies were essentially blind and lacked direct evidence on the changes in the oxidation state of the dopant ion and the extent of local restructuring within the crystal. In this regard, structural techniques such as X-ray absorption spectroscopy (XAS) can be utilized as alternative approach to the electronic structure described earlier and/or complementary technique

to optical spectroscopic investigations. In our study on moderately-doped (0.01%mol) CaF_2 crystal, XAS was able to determine that the predominant local structure corresponds to a Ce^{3+} ion coordinated by eight fluorine ions in an undisturbed cubic (O_h) field, rather than a distorted tetragonal (C_{4v}) center. However, it should be noted that the analysis only provides for the average local structure. To address this limitation, some studies have employed more sophisticated techniques such as electron paramagnetic resonance (EPR) and nuclear magnetic resonance (NMR). From optical spectroscopies, we were also able to establish that the presence of the distorted Ce^{3+} trigonal (C_{3v}) center in the CaF_2 crystal yields same emission peaks. However, the corresponding quantum yield is lower, rendering it impractical for excitation.

X-ray absorption spectroscopy (XAS) at the Ce L_3-edge can also provide additional information about the localization or non-localization of Ce^{3+} ion's 4f electrons. Limited studies on CeF_3 (localized), and CeO_2 (non-localized) and few other compounds have demonstrated this behaviour. Our results suggest that the Ce^{3+} ions in both $LiCaAlF_6$ and $LiSrAlF_6$ crystals have non-localized 4f electrons. The non-localization of electrons in the 4f offered new insights into the luminescence and lasing properties of these crystals. Specifically, it identified the origin of anisotropy in the optical properties of both crystals and of ESA as resulting from covalent interactions between the Ce^{3+} and its neighbouring F^- and Al^{3+} ions. Our study has, for the first time, elucidated the origin of ESA which is one of the main reasons why most Ce-doped fluoride and oxide crystals don't lase in the UV region. From our results, it is equally important to ensure that the 5d levels are positioned well above the conduction band and to examine not only the influence of the first coordination shell but also the interaction of the Ce ion with other metal ligands. Covalent interaction between Ce^{3+} ion and its neighbours, F^- and Al^{3+} ions was shown to influence the luminescence and lasing performance of Ce^{3+}-doped $LiCaAlF_6$ and $LiSrAlF_6$ crystals, particularly along the c-axis direction where the Al^{3+} ions are stacked. The covalent interaction in Ce^{3+}-doped $LiSrAlF_6$ is stronger than in Ce^{3+}-doped $LiCaAlF_6$, resulting in more pronounced optical anisotropy and greater ESA. In terms of electronic structure, a stronger covalent interaction corresponds to a greater shift of the 4f and 5d levels towards the valence band of the

host. This is consistent with the tilting of the zig-zag curves of Ln^{2+} and Ln^{3+} in the VRBE plot towards lower energy due to the nephelauxetic effect with an increasing number of 4f electrons [**?** **?**]. New insights from structural studies, such as the ones exemplified in our study, are necessary for the future development of high-performance UV lasers and excellent scintillators.

In addition to the energy-level structure of a laser material, the design of a laser is influenced by many other interdependent factors. These factors include the characteristics of the output beam (such as wavelength, spectral purity, tunability, divergence, polarization, power, and power stability), the operating environment (including temperature, humidity, vibration, acceleration, and externally applied forces), as well as practical considerations (such as size, cost, available power, and pump-source characteristics) [**?**]. In today's laser technology, a wide range of gain media, cavity designs, and pump configurations have been employed. Numerous studies have been published on the subject of laser design. However, it is important to note that there is no one-size-fits-all design solution for all applications. Each laser must be carefully optimized to operate at one point in the multidimensional parameter space mentioned above.

Chapter 8

Conclusion

8.1 Conclusion

We have successfully evaluated the local crystalline environment of Ce ions in a 0.01mol% Ce-doped CaF2 crystal, as well as in 1.0mol% Ce-doped $LiCaAlF_6$ and $LiSrAlF_6$ crystals. By employing XAS techniques, we were able to demonstrate the extent of restructuring in both a cubic (CaF_2) and trigonal (LiCaAlF6 and LiSrAlF6) host lattice at relatively low doping concentrations.

In the case of the Ce-doped CaF_2 crystal, the presence of multiple VUV absorption bands ranging from 180 to 300 nm and two UV emission peaks around 320 and 340 nm were confirmed to be due to the existence of a dominant single-ion Ce^{3+} center. However, the symmetry was assigned to cubic (O_h) rather than tetragonal (C_{4v}). Unfortunately, our XAS K-edge XANES and EXAFS analysis were unable to discriminate between different symmetries of the Ce^{3+} ion, and thus could not confirm the presence of a cluster-ion Ce^{3+} center, despite the presence of its signature 240-nm absorption band in the optical spectroscopic data.

The absorption and emission bands in Ce-doped $LiCaAlF_6$ and Ce-doped $LiSrAlF_6$ crystals exhibited anisotropy. XAS results confirmed that the Ce^{3+} ions are in a 6-coordinated octahedral environment with stretched Ce-F bond lengths and extended F-Ce-F^{ii} (and contracted F-Ce-F^{i}) bond angles. DFT and FDMNES simulations reveal that the 5d→4f (4f→5d) transitions in these crystals are influenced by the first-coordinate trigonal

octahedron and the second nearest neighbor, Al^{3+} ions, layered along the c-axis. Particularly, the anisotropy in the optical properties and ESA, which are more pronounced in Ce-doped $LiSrAlF_6$, can be attributed to the covalent interaction between the Ce^{3+} ion and its neighboring F^- and Al^{3+} ions. The presence of peaks C and D in the L_3-edge spectra are also due to the charge transfer between the Ce^{3+} ion and its ligand ions, resulting from the hybridization of their electronic states.

Our study has also successfully demonstrated the sensitivity of the Ce L_3-edge approach to the multi-electron processes involving the 4f and 5d levels of Ce^{3+}-doped colquiriite-type fluoride crystals. Thus, it can be further exploited to understand the luminescence of other host crystals doped not only with Ce^{3+} ions but also with other inner transition metals. Employing structural techniques to complement the electronic-structure approach will not only enhance our understanding of fundamental physical phenomena and underlying mechanisms in wide bandgap fluoride crystals but also contribute to the development of new high-performance lasers, scintillators, and other optoelectronic devices.